

1926 1 NACA 1 N 2953

TECH LIBRARY KAFB, NM



0000180

# NATIONAL ADVISORY COMMITTEE FOR AERONAUTICS

TECHNICAL NOTE 2953

AN INVESTIGATION OF THE EXPERIMENTAL AERODYNAMIC LOADING  
ON A MODEL HELICOPTER ROTOR BLADE

By John R. Meyer, Jr., and Gaetano Falabella, Jr.

Massachusetts Institute of Technology



Washington  
May 1953

TECHNICAL NOTE 2953  
AFL 2811



0066180

NATIONAL ADVISORY COMMITTEE FOR AERONAUTICS

## TECHNICAL NOTE 2953

AN INVESTIGATION OF THE EXPERIMENTAL AERODYNAMIC LOADING  
ON A MODEL HELICOPTER ROTOR BLADE

By John R. Meyer, Jr., and Gaetano Falabella, Jr.

## SUMMARY

Pressure distributions were measured on a model helicopter rotor blade under hovering and simulated forward-flight conditions. Pressures were recorded at advance ratios  $\mu$  of 0.10, 0.22, 0.30, 0.40, and 0.50 for a zero-offset flapping-hinge rotor and at 0.10, 0.22, 0.30, 0.45, 0.60, 0.80, and 1.0 for a lifting rotor having a flapping-hinge offset of 13 percent.

Analyses of the data for the zero-offset condition at  $\mu = 0.22$  and 0.50 and the 13-percent-offset condition at  $\mu = 0.22$  and 1.0 are presented in the form of chordwise pressure distributions, spanwise loadings, and contour plots. The contour plots, showing the loading distribution on the disk, indicated a marked difference between the aerodynamic characteristics of the two rotors operating under identical conditions. The introduction of an appreciable amount of flapping-hinge offset resulted in a large first-harmonic aerodynamic loading in simulated forward flight. The recorded data not analyzed are included in a separate grouping.

Blade flapping measurements revealed appreciably lower values of first-harmonic flapping coefficients for the offset rotor as compared with the conventional configuration. An analysis of the angle of attack at the tip of the retreating blade, based on experimental flapping measurements, indicated that an appreciable offset flapping hinge in combination with a low blade mass constant offers a means of postponing stall on the retreating blade.

## INTRODUCTION

The complex flow pattern existing in the wake of a helicopter rotor in forward flight does not conveniently lend itself to exact mathematical treatment. Consequently, at present the mathematical investigations (refs. 1, 2, and 3) dealing with the inflow and aerodynamic-loading problems contain a number of assumptions and

approximations which leave some doubt as to the validity of results obtained. Some means by which the importance of these simplifications can be established appears desirable.

From the structural point of view the actual rotor blade loading corresponding to various flight conditions is a subject which warrants clarification, as pointed out in reference 4, since the bending-moment distribution is at present for a large part dependent upon the aerodynamic loads determined by a theoretical analysis.

The previous considerations indicate a demand for detailed information regarding the actual aerodynamic loading on a rotor blade under various operating conditions. It was the purpose of this work to investigate the possibility of determining, by means of a small-scale wind-tunnel model, the aerodynamic loading on a helicopter rotor blade.

At the outset, a number of methods were considered for carrying out this study. They are briefly as follows:

(1) Determination of the bending-moment distribution and deflection curve of a stiff blade. As a result of the tests performed in reference 4 it has been established that the bending-moment distribution on a model rotor blade may be experimentally determined to a good degree of accuracy. Distributions obtained in this manner could be differentiated twice to obtain the total loading on the blade. The measured blade deflection curve yields the inertia loading and hence the aerodynamic loading would result from the algebraic sum of the total and inertia loadings. The disadvantages of this method are the rather large error that may be introduced as a result of the differentiation process and the high degree of accuracy needed in the determination of the deflection curve.

(2) Determination of the blade deflection curve alone for a very flexible blade. The magnitude of the bending-moment distribution on a very flexible blade is small and consequently the magnitude of the net-loading curve (difference between aerodynamic and inertia loads) for the very flexible blade is also small compared with either the inertia- or aerodynamic-loading curves. Hence an approximation to the aerodynamic loading may be obtained by merely considering the inertia loading on a highly flexible blade as determined by its observed deflection during operation. The technique here involves the use of a stroboscopic light which would "stop" the blade at a given azimuth while a cathetometer measures vertical deflection above an arbitrary reference plane. The difficulty arising here is the application of this approach to the forward-flight condition in the wind tunnel since, for satisfactory loading results, the spanwise deflection curves must be determined quite accurately at a sufficient number of azimuths throughout the rotor disk.

(3) Measurement of air forces on a rotating blade by the use of a pressure pickup unit. A pressure pickup unit has been developed at the Massachusetts Institute of Technology which is directly applicable to this problem and provides a convenient approach. The rotor system which incorporates the pickup would be provided with blades having a series of tubes with appropriately spaced orifices. These tubes would run spanwise and be located at various chordwise positions on both the upper and lower surfaces. A remotely controlled pressure switch located on the hub would select the orifices in a chordwise direction and expose the pressure pickup momentarily to the pressure difference existing at a given pair of orifices on the blade. A recording oscillograph then would yield a continuous record of the pressure-difference variation at a point as it travels in the azimuth direction. From these data aerodynamic loadings on the entire disk may be obtained with considerable accuracy, thoroughness, and convenience.

Limited success was obtained in the attempt to apply the first two methods; however, the experimental difficulties encountered as mentioned above did not warrant the time, expense, and effort necessary to overcome them. In preference to the further development of the first two methods, the third because of its comparative simplicity and applicability was selected and developed for use in this aerodynamic-loading investigation.

This investigation was conducted at M.I.T. under the sponsorship and with the financial assistance of the National Advisory Committee for Aeronautics.

#### SYMBOLS

A	total disk area, sq ft
$a_0$	constant term in Fourier series that expresses $\beta$ (eq. (2))
$a_1, b_1$	coefficients of $\cos \psi$ and $\sin \psi$ , respectively, in expression for $\beta$ (eq. (2))
$C_Q$	torque coefficient, $Q/\rho A \Omega^2 R^3$
$C_T$	thrust coefficient, $T/\rho A \Omega^2 R^2$
c	blade-section chord, ft unless otherwise stated
e	flapping-hinge offset, ft unless otherwise stated
$I_1$	blade mass moment of inertia about flapping hinge, slug- $ft^2$

L	rotor lift, lb
m	mass of blade per foot of radius, slugs/ft
$m_b$	total mass of blade, slugs
Q	rotor torque, ft-lb
R	blade radius, ft unless otherwise stated
r	radial distance to blade element, ft unless otherwise stated
T	rotor thrust, lb
$U_P$	component at blade element of resultant velocity perpendicular both to blade-span axis and $U_T$ , ft/sec
$U_T$	component at blade element of resultant velocity perpendicular to blade-span axis and to axis of no feathering, ft/sec
V	true airspeed of helicopter along flight path, ft/sec
v	induced inflow velocity at rotor, ft/sec
x	chordwise distance, ft; also, in appendix A, ratio of blade-element radius to rotor-blade radius, $r/R$
$\alpha$	rotor angle of attack, positive when shaft axis is pointing rearward, radians unless otherwise stated
$\alpha_r$	blade-element angle of attack, radians unless otherwise stated; maximum value indicated by sub-subscript max
$\beta$	blade flapping angle at particular azimuth position, radians unless otherwise stated
$\gamma$	mass constant of rotor blade
$\theta$	blade-section pitch angle, radians unless otherwise stated
$\lambda$	inflow ratio, $(V \sin \alpha - v)/\Omega R$
$\mu$	advance ratio, $(V \cos \alpha)/\Omega R$
$\xi$	flapping-hinge offset ratio, $e/R$
$\rho$	mass density of air, slugs/cu ft

$\sigma$  rotor solidity

$\psi$  blade azimuth angle measured from downwind position in direction of rotation, radians unless otherwise stated

$\Omega$  rotor angular velocity, radians/sec

#### DESCRIPTION OF APPARATUS

Rotor blades.- The model rotor blade design was dictated by the testing facilities available and the desire to obtain data that would be directly applicable to models previously used in bending-moment investigations (ref. 4). Therefore, in agreement with this reference, the rotor diameter was 5 feet, the profile was NACA 0015, and the chord was 3 inches. A two-bladed configuration was chosen in order to simplify the hub and pitch-control design. Figure 1 shows the arrangement of the tubes in the blade and the orifice locations. Also shown are the cross section of the blade spar (steel) and the leading-edge weight, inserted for the purpose of obtaining chordwise balance. A high-stiffness blade was desired since it was imperative that the tubes imbedded in the surface of the blade remain essentially unflexed if leaks were to be avoided. The stiffness  $EI$  which resulted from the steel spar with balsa-wood profile was 43,000 lb-in.<sup>2</sup> and the uniform blade mass distribution  $m$  was 0.0178 slug/ft. These blades were used on the two rotor configurations described below.

Rotor with 13-percent-offset flapping hinge.- During the design stage of the rotor it was desired to incorporate internal pitch controls in order to produce a clean configuration. As a result, the flapping- and lag-hinge axes were located at radial positions of  $3\frac{13}{16}$  and  $4\frac{1}{4}$  inches, respectively. Figure 2 shows the blade and the two adapters which allowed the same blades to be used either in the hinged- or fixed-at-root condition.

Figure 3 is a schematic drawing of the rotor hub showing the swash plate and pitch control arms. The blade spar extensions rotated in ball bearings and were held against centrifugal loads by a nut provided with a tapered pin. The gearbox detail is shown in figure 4. Here the main rotor power was transmitted through an offset idler shaft so that the collective- and cyclic-pitch control rods could be actuated through the hollow upper rotor drive shaft. The collective-pitch yoke, located at the end of the control rod, fitted into the rotor hub annulus. The cyclic-pitch control rod was located within the collective-pitch rod and was connected to the ball-bearing swash plate through a linkage. These control rods were operated by individual small electric

motors through gearboxes which were mounted in such a manner that the operation of one control did not affect the position of the other control. This was accomplished by attaching the cyclic-pitch gearbox and motor to the collective-pitch control rod by means of a slide. Collective- and cyclic-pitch control motions were transferred to the control panel by means of small autosyn motors and indicators. The autosyn motors, located in the rotor control gearbox, can be seen in figure 4. The indicators were located in a single instrument on the control panel (fig. 5) so that blade pitch could be controlled and read at all times during testing.

Rotor with zero-offset flapping hinge. - In order to permit comparison of the aerodynamic loadings on a rotor with appreciable hinge offset and one with zero hinge offset, a rotor hub having a flapping hinge located on the axis of rotation was designed and built. Figure 6 shows a close-up of the hub arrangement. It can be seen that the blades were individually hinged; and, unlike the 13-percent-offset rotor, this design did not provide cyclic-pitch change and the collective pitch had to be adjusted before operation. The pressure switch and pickup were mounted on top of the rotor shaft extension in such a manner that they were independent of the blade motion. A view of the zero-offset rotor with the spinner in place and installed in the wind tunnel is shown in figure 7.

Rotor mounts. - In the hovering condition a conical mount was employed. This configuration is shown in figure 8 where the rotor disk was approximately 10 feet above the floor. The rotor drive motor, located inside the cone, was supported with its shaft in the vertical direction and the rotor shaft was connected by means of a universal coupling. The gearbox with remote pitch controls was not incorporated since it was not thought necessary to have pitch controls for this condition. The streamlined mount for wind-tunnel tests is shown in figure 9 where the gearbox and rotor can be seen installed. The entire mount was pivoted so that various shaft-axis inclinations  $\alpha$  could be obtained.

Lift and torque measuring equipment. - It was considered advisable to measure total lift in order to check the aerodynamic loadings obtained from pressure-distribution measurements. A strain-gage lift balance was therefore designed and incorporated into the equipment. The device consisted primarily of two cantilever beams with a total of four strain gages (type CD-7) placed in two arms of a Wheatstone bridge circuit and connected to a Baldwin-Southwark strain indicator. Accuracy of the lift balance was within 0.2 pound. The rotor hub assembly was allowed to move in a direction parallel to the shaft axis by means of a sliding fit between the mount and rotor assembly. A fork and arm were provided for calibrating the balance and preloading the beams. This assembly can be seen in figure 9.

In regard to torque measurements, the motor was calibrated to obtain horsepower output as a function of armature current over the operating speed range. The calibration allowed the rotor input power to be measured within 0.01 horsepower.

Pressure measuring equipment.— The pressure pickup employed in this equipment was one developed at M.I.T. which utilizes the RCA Mechano Electronic Transducer (RCA vacuum tube 5734). The pickup consists of two chambers separated by a thin metallic diaphragm which is connected to the sensitive element of the transducer. The output of the pickup and its associated equipment was connected to a Consolidated oscillograph equipped with a type 7-112 galvanometer having a sensitivity of 30 in./ma. The over-all sensitivity of the entire pressure measuring system was the order of 0.20 lb/sq in./in. of galvanometer deflection which allowed pressure measurements within 0.01 lb/sq in. A picture of the pressure pickup is shown in figure 10.

The pressure pickup was connected to the 0.065-inch outside-diameter (inside diameter, 0.045 inch) stainless-steel tubes imbedded in the upper and lower surfaces of the blade (fig. 1) by means of flexible tubing and a pressure switch. Figures 11 and 12 show the switch assembled and the arrangement of the holes and slots in the mating surfaces. The switch was designed in such a manner that a pair of orifices on opposite surfaces of the blade were connected to the two chambers of the pickup simultaneously. The measurement obtained therefore was the pressure difference across a given point on the blade. This scheme resulted in a cancellation of the centrifugal-force effects on the air column in the blade tubes. A feature which allowed data to be taken conveniently and quickly was the zeroing device incorporated into the pressure switch. This consisted of the enlarged slots which connected the two crescent-shaped channels at two different switch positions and thereby short-circuited or exposed the two chambers in the pickup to the same pressure twice per revolution of the pressure switch. The result was a zero-pressure-difference signal at these two switch positions. The switch was rotated through a gear train by a small electric motor which was mounted on the rotor hub and remotely controlled while the rotor was in operation. Figure 13 shows the pressure switch and pickup assembly. Electrical connections were made to this assembly by a series of slip rings and brushes. In addition to the six silver rings there was a Bakelite ring having two small metal contacts for the purpose of determining the azimuth position of the rotor blades as a function of time. This was accomplished by including these contacts in a circuit whose response was recorded on the oscillograph simultaneously with the pressure-pickup trace.

Since the pressure variations occurring on the blade in the simulated forward-flight condition were transmitted through tubes to the pickup, it was necessary to carry out a dynamic calibration of the pressure measuring system. Calibration was accomplished by attaching a small

chamber to the blade, as shown in figure 14, and applying a very closely approximated sinusoidal pressure variation. At one end of the chamber a flush-type pressure pickup was located while the opposite end was exposed to a given point on the blade through a rubber seal. The diaphragm of the flush-type pressure pickup was considered sufficiently close to the blade orifice so that no phase-lag or amplitude correction was necessary for this response. In this manner a calibration was made which to a first approximation duplicated operating conditions. A pressure variation over a frequency range of from 0 to 35 cps was applied to the chamber and the response of the two pressure pickups was compared to obtain amplitude ratio and lag information. Results of such a procedure are given in figures 15(a) and 15(b). This lag information was used only in the first analyses. Subsequent and final analyses utilized another method of correction described in a section under "Discussion of Results."

Blade flapping measurements.-- It was desirable to record the blade flapping motion for the two rotors described herein. An autosyn was used for this purpose. A 400-cycle input resulted in an envelope whose double amplitude depended upon the position of the armature which in turn was coupled to the flapping-hinge pin. The arrangement can be seen in figures 6 and 7. The input and output leads were brought through the same slip-ring assembly that was used for the pressure tests. The output was recorded on an oscillograph simultaneously with the signal from the azimuth indicator. Calibrations of the output double amplitude against blade flapping angle resulted in curves which were linear within 10 percent. Sensitivity of flapping-motion recording equipment was of the order of  $10^{\circ}$ /in. of galvanometer deflection.

#### PROCEDURE

Cellophane tape was used to cover the orifices on the rotor blades. The tape on the span station where data were desired was removed and the rotor was set at an operating condition. The pressure-switch motor was then energized and its speed was regulated to give a satisfactory record. This procedure scanned the chordwise pressure distribution and resulted in a record similar to the sample shown in figure 16. Here a dashed line has been drawn which connects the two zero-pressure-difference levels and measurements are made from this line to the pressure-pickup response trace. The trace is slightly distorted by 60-cycle hash, but this does not interfere with the analysis appreciably. On shutting down the rotor, the test span station was retaped and another span station was exposed. This procedure was repeated until a pressure distribution for the entire blade was obtained. Total-lift and torque data were taken at the operating rotational speed with blade pitch  $\theta$  of  $0^{\circ}$  and then at the pitch setting corresponding to the condition being investigated.

It should be pointed out that a number of undesirable effects upon the pressure pickup were eliminated by the zeroing feature built into the pressure switch. Most important of these were centrifugal force (although the sensitive diaphragm was close to the center of rotation), temperature changes, and drift in the electrical equipment. Since the zero pressure difference was recorded at the time pressure records were taken these various effects were automatically accounted for on the records.

When taking data in the wind tunnel, the tape was removed from a given span station and data were obtained, as previously described, at a series of  $\mu$  conditions. The rotor and tunnel were then shut down, the span station retaped, and another span station exposed. The process was repeated until pressure data for the entire blade were obtained.

Preparation for blade flapping-motion measurements was made by disconnecting the pressure-pickup lead wires and attaching the autosyn leads. Blade flapping motion was then recorded on the oscillograph at conditions corresponding to the series selected for the pressure-data tests.

All tunnel tests on the zero-offset and 13-percent-offset rotors were run at a rotor angle of attack of  $-5^\circ$ . The pitch setting for all conditions was  $8^\circ$  except at the highest advance-ratio condition for the offset rotor when this angle was reduced to  $4^\circ$ . The rotors had no cyclic pitch applied in these tests.

In regard to lift measurements in the tunnel, it was found that the lift-drag interference was too great and therefore the data were not considered satisfactory for comparison with the data obtainable from the pressure traces. The torque measurements were satisfactorily recorded for the model, but their significance in view of the low Reynolds number is questioned.

## DISCUSSION OF RESULTS

### Hovering Condition

A sample oscillograph record for the rotor with offset flapping hinge in the hovering condition is shown in figure 16. Here are seen the different pressure levels corresponding to the various chordwise positions on the blade and the zero-pressure-difference condition at both ends of the trace. The resulting chordwise pressure distributions for the condition of  $\theta = 8^\circ$  and 800 rpm are shown in figure 17. These curves have been integrated and plotted to obtain the spanwise aero-dynamic loading shown in figure 18. Note that data have not been

obtained at every span station available since the distribution is satisfactorily determined by the points shown. An integration of the span loading resulted in a total lift on one blade of 3.9 pounds. Assuming that both blades produced the same amount of lift, the total lift on the two-bladed rotor was 7.8 pounds which checks the total lift balance reading of 7.9 pounds satisfactorily. This condition corresponds to  $C_T = 0.0038$ ,  $\lambda = -0.044$ , and  $C_Q = 0.00029$ .

Another hovering test was carried out with the blades fixed at the root under the same conditions (800 rpm and  $\theta = 8^\circ$ ). It was expected that the results would be identical to those obtained from the hinged-at-root condition. This was essentially realized since the total lift balance reading of 7.6 pounds was obtained against an integrated result of 7.4 pounds. The slight discrepancy between the measured total lift readings for the two root conditions can be attributed to slight errors in blade pitch, rotational speed, and the lift balance. The loading curve is not presented since it is essentially the same in character as that shown in figure 18.

#### Simulated Forward-Flight Condition

Amplitude-ratio and lag correction of pressure data. - The amplitude-ratio curves of figures 15(a) provide the necessary information for correcting the pressure data for amplitude distortion when desired. Inasmuch as the over-all loading investigation was considered basic and explorative, it was not considered essential at this time to correct the pressure data for amplitude distortion. Testing was limited to a maximum rotational speed of 800 rpm which corresponds to a first-harmonic frequency of 13.3 cps. Examination of figure 15(a) shows an average error of approximately 10 percent at this frequency. The amplitude error decreases at the second-harmonic frequency. However, response at frequencies higher than those corresponding to the second harmonic is seen to be highly damped and therefore much in error. It is felt that the data do not adequately represent the aerodynamic loading beyond the second harmonic if the third and higher harmonics actually existed in significant strength.

The problem of correcting the pressure signals for lag in the system was mentioned briefly in a previous section, but the method referred to there was eventually discarded in preference to a more direct approach. This present method takes advantage of the theory for an offset rotor developed in appendix A and the measurement of blade flapping motion. These measurements made it possible to determine the azimuth of maximum flapping for all conditions tested. In accordance with the results of the analysis in appendix A, the maximum positive inertia moment occurs when the flapping angle is a positive maximum. From equilibrium considerations, it is necessary that the aerodynamic moment about the hinge

be a positive maximum also when the flapping angle is a positive maximum. There are three possible ways the aerodynamic moment may change; namely, by a constant loading vector changing its position in the spanwise direction, by a varying vector acting at a given spanwise position, or by a combination of the two. It can be seen from the spanwise loadings at four azimuths (e.g., see fig. 23) that the resultant loads pass through approximately the same spanwise position. The conclusion can then be drawn that not only does the azimuth of maximum flapping indicate the position of maximum aerodynamic moment but also the azimuth of maximum aerodynamic loading. The result therefore gives rise to a boundary condition which enables a rather accurate and convenient lag correction to be made. Since the rotor with zero flapping-hinge offset makes use of the same pressure measuring system, the same lag corrections apply.

Blade flapping motion. - Harmonic analyses of all the blade flapping-motion data were made (see appendix A) and the results are shown in figure 19. The effect of introducing a flapping-hinge offset can be readily seen. The cosine component of flapping was reduced considerably, the sine component increased slightly, and the apparent  $\mu$  range over which operation could be sustained without excessive vibration almost doubled. Although data were obtained with the 13-percent-offset rotor at  $\mu = 1.0$  these data have not been included in figure 19 since the pitch setting was  $4^\circ$  for this condition rather than  $8^\circ$ . Only steady-state and first-harmonic components have been represented since the higher harmonics in general were less than 10 percent of the first-harmonic values. This is significant when approaching the problem from an analytical point of view inasmuch as it indicates that a neglect of higher harmonics does not greatly affect the results.

Rotor with offset flapping hinge. - The oscillograph records were analyzed by first drawing a reference line connecting the two zero-pressure-difference levels at each end of a given record. Using the azimuth indicator marks on the records and the appropriate lag corrections, the azimuth and pressure-difference scales were laid out on each of the six traces representing the response of the six chordwise locations at a given span station. The cycles were then cut from the records and assembled in proper sequence as shown for the examples in figure 20.

It will be noted that the pressure-difference traces conform with physical expectations in that a high pressure level is found near the leading edge and diminishes to a lower level in the neighborhood of the trailing edge; and, in addition, the pressure differences gradually build up spanwise from the inboard section of the blade out toward the tip and then proceed to fall off abruptly. However, on examining any one of the cycles for the condition where the flapping hinge is offset,

it will be clearly seen that there exists a large amount of first-harmonic variation with a concentration of loading at  $\psi = 150^\circ$ . It was felt that this first-harmonic aerodynamic loading would have to be substantiated and the phenomenon more fully understood if the data were to be accepted as free from any shortcomings in the pressure measuring equipment.

An experimental check was carried out therefore on the equipment in the following manner. The model with the offset flapping hinge ( $\xi = 0.13$ ) was set up outside the wind tunnel and operated with various amounts of cyclic pitch which resulted in certain magnitudes of blade flapping. It was found that a considerable amount of first-harmonic pressure variation with azimuth resulted which substantiated the wind-tunnel tests. The rotor was then temporarily modified to a teetering configuration ( $\xi = 0$ ), but it was necessary to remove the pressure-switch assembly since the annular hub was free to pivot and the test could not tolerate the relatively large mass concentrated above the teetering axis. The pickup alone, however, was mounted directly on the hub which made it possible to obtain the pressure-difference response of a pair of orifices during a given run. On operating the rotor with cyclic pitch as above, it was found that there was no appreciable variation in pressure difference with azimuth which is in accordance with theory and physical expectations. This preliminary test demonstrated that the aerodynamic characteristics of a rotor with relatively heavy blades are appreciably modified upon introducing a flapping-hinge offset of the order of 10 percent.

It is well-known that for a rotor with zero flapping-hinge offset the first-harmonic aerodynamic loading is very small since there is a cancellation of the first-harmonic inertia moments. However, the analysis given in appendix A points out that with the introduction of a flapping-hinge offset this is not the case. An appreciable amount of first-harmonic aerodynamic moment is necessary to satisfy the equilibrium condition at the flapping hinge. Furthermore, an analysis of the angle of attack of the blade or at the tip shows that the offset has the effect of decreasing the maximum angle of attack as compared with that of a rotor having zero offset under the same operating conditions. The comparison is shown in figure 21. Another interpretation of this result is that the introduction of offset enables a lifting rotor to operate aerodynamically at an appreciably higher value of advance ratio without adverse stall effects. Obviously the structural and vibration problems that would be introduced by an appreciable offset blade design need investigating before a conclusion as to the merit of such a design may be reached. It should be noted that the blade mass constant  $\gamma$  of the rotors tested was approximately 2, which is low compared with that of conventional rotors. The significance of the hinge offset is discussed in greater detail in appendix A.

Analyses of raw data were carried out for advance ratios of 0.22 and 1.0 for the offset rotor. The general procedure in carrying out an analysis was to pick off points from the oscillograph traces at four azimuths  $90^\circ$  apart, the azimuth corresponding to maximum pressure difference being one of these positions. It was then possible to plot chordwise pressure-difference distributions at each span station for the four azimuths as shown in figure 22. The chordwise distributions were then integrated to obtain spanwise loading diagrams, examples of which are given in figure 23. The analysis was extended by taking points from these curves and plotting aerodynamic loading against azimuth for a series of radial stations. Loadings were then read from the resulting curves at  $30^\circ$  intervals and tabulated for the purpose of constructing a contour plot showing the aerodynamic loading over the entire disk as exemplified by figure 24. The data and plots for the  $\mu = 1.0$  condition are shown in figures 25 to 27.

In constructing the chordwise plots mentioned, it should be noted that a certain amount of extrapolation was necessary in the vicinity of the leading edge because physical limitations did not permit data to be conveniently obtained in this neighborhood. The relatively high pressure differences recorded at chord station 6 for the analyzed condition of  $\mu = 0.22$  and  $\xi = 0.13$  (fig. 22) are not in agreement with usual chordwise pressure distributions. In fact all the traces (see appendix B) for the offset rotor under conditions of  $\mu = 0.10$  through  $\mu = 0.45$  show that chord station 6 experiences pressures of the same magnitude as station 5. However, this unusual aerodynamic effect was not recorded for the advance ratios of 0.60, 0.80, and 1.0. Interestingly, there is no evidence of this phenomenon on any of the zero-offset traces. To attribute the cause to faulty instrumentation on the evidence available does not seem any more reasonable than to expect that this unusual flow condition really does exist. In the absence of more definite indications, the curves of figure 22 were drawn in accordance with conventional theory, although it is pointed out that further investigation may show fairing the curves in this manner to be incorrect. It is felt that the above two approximations introduced little distortion in the over-all picture.

It should be noted that, since no cyclic pitch was applied to the offset rotor, rolling and pitching moments were experienced. The test equipment did not provide for the measurement of these moments; however, a discussion of the rolling and pitching moments on an offset rotor is presented in reference 5. Applying the expressions given there to the rotor under test, the pitching and rolling moments become 3.20 and 4.72 ft-lb, respectively, for  $\mu = 0.22$ , and 8.27 and 14.4 ft-lb for  $\mu = 0.60$ .

In regard to the fixed-at-root rotor blade configuration in simulated forward flight, an attempt was made to obtain pressure data at

high values of advance ratio but tests were curtailed by the failure of a root fitting during operation. Further testing of the fixed-at-root blade at this time was discontinued inasmuch as advance-ratio data up to and including 1.0 had been obtained from the 13-percent-offset hinged blade.

Rotor with zero-offset flapping hinge. - An analysis of the pressure data for advance ratios of 0.22 and 0.50 was carried out for the zero-offset rotor in the same manner as that described in the section on the 13-percent-offset rotor. The raw data and plots derived therefrom are given in figures 28 to 34. These particular advance ratios were chosen since 0.22 was the lowest  $\mu$  analyzed in the case of the offset rotor and 0.50 was the highest  $\mu$  at which data were obtained for the zero-offset rotor because excessive flapping limited operation to this condition. The rather high hash level in many of the records is of a 60-cps nature and was due to other equipment operating in the laboratory at the time these records were taken. Analyses were not seriously hampered by this effect, however, since a curve could readily be faired through the 60-cycle hash to represent the true pressure variation.

It will be noted from figure 28, showing the oscillograph traces of the pressure-difference variations at  $\mu = 0.22$ , that there exist only relatively small variations in lift with azimuth. This effect is shown in the contour plot of figure 31. The results of tests carried out as an extension of the work described in this report indicate pressure data which are very much the same as those described above except for a second-harmonic component of greater magnitude. The aerodynamic loadings, for the zero-offset condition contained herein, should therefore be applied with discretion in the determination of inflow and other cases where the second-harmonic component may be of importance.

The data for  $\mu = 0.50$  show certain low lift regions due to either stalled areas (low Reynolds number or high  $\alpha_r$ ) or areas of relatively low velocity, during the retreating portion of the cycle. The pressure-difference variations associated with these regions have almost a square-wave appearance, particularly noticeable in figures 32(a) to 32(d). Consequently, the contour plot for this condition, as shown in figure 34, indicates an aerodynamic-loading concentration in the region of  $\psi = 60^\circ$ . The two contour plots mentioned here illustrate the shift in aerodynamic-loading distribution which is associated with a change in advance ratio. The uniformity of loading appears to disappear at higher values of  $\mu$  because of the influence of large reverse flow regions and in the case of model testing possible scale or Reynolds number effects (appendix C).

## CONCLUSIONS

Pressure measuring equipment has been developed and applied to the problem of determining the aerodynamic loading on a model helicopter rotor blade in hovering and simulated forward flight. A zero-offset flapping-hinge rotor and a lifting rotor having a flapping-hinge offset of 13 percent were tested. From this investigation it was found that:

1. In the hovering condition total-lift measurements and integrated pressure distributions were in good agreement.
2. In the forward-flight condition the aerodynamic loading of the zero-offset rotor was in accordance with expectations, but the introduction of appreciable offset (13 percent) resulted in a large first-harmonic contribution. This phenomenon was substantiated by analysis.
3. Contour plots of comparable operating conditions revealed a highly concentrated loading on the disk of the 13-percent-offset rotor near an azimuth of  $150^{\circ}$  in contrast with the substantially uniform loading of the zero-offset rotor.
4. Blade flapping measurements revealed appreciably lower values of first-harmonic flapping coefficients for the 13-percent-offset rotor as compared with the conventional configuration. Higher harmonics were found to be negligible for all test conditions. Excessive flapping limited operation of the zero-offset rotor to an advance ratio  $\mu$  of 0.50 with a blade-section pitch angle of  $8^{\circ}$  and a rotor angle of attack of  $-5^{\circ}$ , whereas the 13-percent-offset rotor was operated through  $\mu = 0.80$  for the same values of pitch angle and angle of attack. A condition of  $\mu = 1.0$  was obtained with the latter rotor at a reduced pitch setting of  $4^{\circ}$ .
5. Angle-of-attack analyses indicated that an appreciable offset flapping hinge in combination with a low value of blade mass constant offers a means for postponing stall on the retreating blade and thereby permits lifting rotor operation at higher values of advance ratio.

Massachusetts Institute of Technology,  
Cambridge, Mass., May 1, 1952.

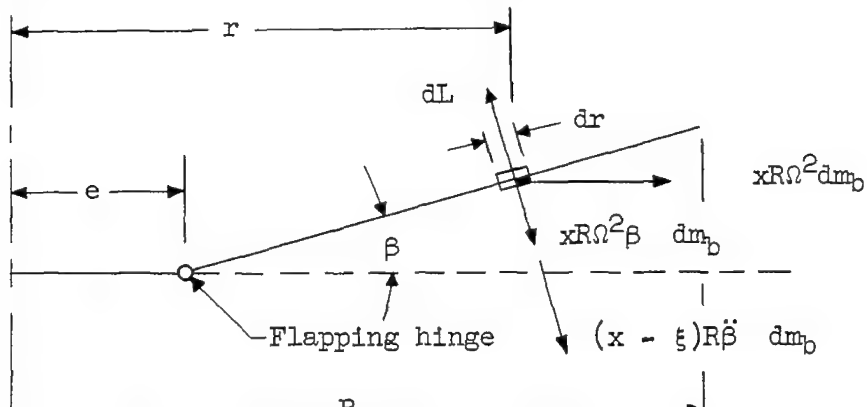
## APPENDIX A

## ANALYSIS OF A ROTOR BLADE WITH OFFSET FLAPPING HINGE

This development demonstrates the necessity for the existence of a first-harmonic aerodynamic moment on a flapping rotor blade having an appreciable amount of flapping-hinge offset. The blade angle-of-attack expression is derived which includes the effect of offset. Experimental blade flapping coefficients are presented and used in the calculation of the maximum blade angle at the tip for the two rotor offset conditions tested.

## Blade Equilibrium Consideration

Consider the blade shown in the following diagram:



$$\xi = e/R \quad x = r/R \quad dm_b = m dr$$

and the equilibrium of aerodynamic and inertia moments about the flapping hinge:

$$\int_{\xi}^1 (x - \xi)R dL = \int_{\xi}^1 \left[ x\Omega^2 R^2 (x - \xi)\beta + (x - \xi)^2 R^2 \ddot{\beta} \right] dm_b \quad (1)$$

Let the flapping angle  $\beta$  be represented by a harmonic series through the first harmonic only. Then:

$$\beta = a_0 - a_1 \cos \psi - b_1 \sin \psi \quad (2)$$

Differentiating twice:

$$\ddot{\beta} = a_1 \Omega^2 \cos \psi + b_1 \Omega^2 \sin \psi \quad (3)$$

Note that

$$x(x - \xi) = (x - \xi)^2 + \xi(x - \xi) \quad (4)$$

Substituting equations (2), (3), and (4) into the right-hand side of equation (1), the inertia moment becomes:

$$\Omega^2 R^2 \int_{\xi}^1 \left[ (x - \xi)^2 (a_0 - a_1 \cos \psi - b_1 \sin \psi) + \xi(x - \xi)(a_0 - a_1 \cos \psi - b_1 \sin \psi) + (x - \xi)^2 (a_1 \cos \psi + b_1 \sin \psi) \right] dm_b \quad (5)$$

Let:

$$I_1 = R^2 \int_{\xi}^1 (x - \xi)^2 dm_b \quad (6)$$

$$\xi = \frac{\xi R^2}{I_1} \int_{\xi}^1 (x - \xi) dm_b \quad (7)$$

where  $I_1$  is the moment of inertia of the blade about the flapping hinge. Let the inertia moment, given by expression (5), be  $M_1$ . With relations (6) and (7), expression (5) becomes:

$$\frac{M_1}{I_1} = a_0 \Omega^2 (1 + \xi) - a_1 \Omega^2 \xi \cos \psi - b_1 \Omega^2 \xi \sin \psi \quad (8)$$

which can be written as:

$$\frac{M_1}{I_1} = a_0 \Omega^2 + \zeta \beta \Omega^2 \quad (9)$$

From equations (1) and (9) it can be concluded that there must exist a first-harmonic aerodynamic moment proportional to the flapping motion. However, when higher harmonic terms are introduced in the flapping expression, equation (2), the harmonic inertia and consequently the harmonic aerodynamic moments are not proportional to  $\beta$  alone. Therefore, the aerodynamic moment and  $\beta$  are simultaneously a maximum only when harmonics higher than the first are negligible in the flapping motion.

#### Blade Angle-of-Attack Consideration

The blade angle of attack  $\alpha_r$  can be developed as follows:

$$\alpha_r = \theta + \frac{U_p}{U_T} \quad (10)$$

$$\alpha_r = \theta + \frac{\lambda \Omega R - (x - \xi) R \dot{\beta} - \mu \Omega R \beta \cos \psi}{\Omega R (x + \mu \sin \psi)} \quad (11)$$

From equation (2):

$$\dot{\beta} = a_1 \Omega \sin \psi - b_1 \Omega \cos \psi \quad (12)$$

Substituting equations (2) and (12) into equation (11) the expression for  $\alpha_r$  becomes:

$$\alpha_r = \theta + \frac{\lambda - (x - \xi)(a_1 \sin \psi - b_1 \cos \psi) - \mu(a_0 - a_1 \cos \psi - b_1 \sin \psi) \cos \psi}{x + \mu \sin \psi} \quad (13)$$

The records of blade flapping motion have been analyzed harmonically and the results for the two hinged conditions  $\xi = 0$  and  $\xi = 0.13$  are presented in figure 19. The zero-offset condition was tested up to and including a  $\mu$  of 0.50; the offset condition was tested through  $\mu = 1.0$ . However, the flapping data recorded at  $\mu = 1.0$  are not included in figure 19 because the pitch setting for this test was changed to  $4^\circ$ . An estimate of the flapping at  $\mu = 1.0$  for comparison with the other advance ratios can be obtained by extrapolating the flapping-coefficient curves from  $\mu = 0.80$ . The steady-state values of flapping  $a_0$  are represented by dashed curves for both the flapping-hinge offset conditions. These values are small and are about the size of the experimental error  $1/4^\circ$ ; consequently, they cannot be considered reliable data. The  $a_0$  coefficients have been included though as a matter of experimental completeness and for possible future comparison or reference.

The experimental flapping data have been substituted into equation (13) for  $\alpha_r$  to find the maximum angle of attack at the tip of the rotor blade for the various advance ratios tested. A small constant positive value of  $a_0$  was assumed in the case of  $\xi = 0.13$ . An arbitrary variation in  $a_0$  of  $1/2^\circ$  resulted in less than a 3-percent change in the values of angle of attack. In view of this, the assumption of  $1/2^\circ$  for  $\xi = 0.13$  was considered justifiable, negative coning angles being unlikely. A similar approximation of  $a_0$  was not needed in the calculation of  $\alpha_r$  for the zero-offset condition because the azimuth of maximum angle of attack occurred very close to  $\psi = 270^\circ$ .

The plots of  $\alpha(1.0)_{\max}$  resulting from the substitution of the experimental data into the expression for angle of attack appear in figure 21. Note that the offset rotor experiences much lower values of  $\alpha_{r_{\max}}$  at the tip than the zero-offset rotor. The azimuth at which  $\alpha(1.0)_{\max}$  occurs for the offset rotor varies from  $\psi = 225^\circ$  at  $\mu = 0.30$  to  $\psi = 200^\circ$  at  $\mu = 0.80$ . Operating conditions except for the hinge location were identical, and the blade mass constants ( $\gamma = 1.8$ ) were approximately the same.

#### Significance of Offset Flapping Hinge

It has been demonstrated that the effect of introducing a flapping-hinge offset on a lifting rotor having a low value of  $\gamma$ , operating with its shaft axis forward without cyclic feathering in a wind tunnel, is to produce an appreciable amount of first-harmonic aerodynamic loading on the disk. The resulting distribution of aerodynamic loading in forward flight is of such a nature that the blade loading is reduced in the low velocity region and increased in the high velocity region. The flapping characteristics are also modified, as pointed out in a preceding section and investigated in reference 5, in that the flapping motion can be considerably reduced for the offset condition noted above. It

should be emphasized that the blade mass constant  $\gamma$  is of importance in producing the above effects. Low values of  $\gamma$  are required in combination with offset to minimize the flapping motion.

The rotor blade angle-of-attack variations are naturally influenced by the loading distribution and the flapping motion that are required for equilibrium. The experimental results given in this report indicate that a pronounced decrease in the maximum angle of attack is experienced by the blade tip at all advance ratios upon introducing an offset of 13 percent and a blade mass constant of 2. Reference 5 explores this phenomenon from a theoretical approach and verifies the experimental results to a close approximation. The decrease in maximum blade angle of attack can be understood when the aerodynamic-loading distribution required for equilibrium is considered. Aerodynamic loading and flapping motion for an offset rotor are such that a shift in the azimuth of maximum angle of attack takes place. The shift is from a low velocity region ( $\psi = 270^\circ$ ) to one of relatively high velocity ( $\psi \approx 220^\circ$ ). This coupled with the reduction of lift in the region of  $\psi \approx 220^\circ$  allows the blade to operate at a lower value of maximum angle of attack under a given set of conditions.

As an example taken from reference 5, the combination of  $\gamma = 4$  and an offset of 0.20 results in the following characteristics at  $\mu = 0.60$ : A concentration of aerodynamic loading at approximately the azimuth of  $140^\circ$ , first-harmonic flapping coefficients of  $a_1 = 5.7^\circ$  and  $b_1 = -5.0^\circ$ , a maximum blade angle of attack of  $14^\circ$ , tip path plane approximately horizontal with the shaft axis inclined forward  $5.5^\circ$ , and no sacrifice in lift.

It should be noted that, if an offset rotor is operated with the proper amounts of cyclic pitch to result in zero moments at the hub, the aerodynamic-loading distribution would revert to that produced by a zero-offset rotor with similar blade angle-of-attack implications.

The question of an offset rotor, operating without cyclic feathering, being capable of producing a propulsive force is one which requires clarification and it is anticipated that some information in this regard will be forthcoming through investigations now in progress.

## APPENDIX B

## UNANALYZED DATA

The raw data in the form of oscillograph records are included as figures 35 to 42 for the purpose of general information and completeness. The lag corrections have been introduced but no attempt at analysis has been made. Records at advance ratios of 0.10, 0.30, and 0.40 for the zero-offset rotor and 0.10, 0.30, 0.45, 0.60, and 0.80 for the 13-percent-offset rotor are presented.

## APPENDIX C

## SCALE EFFECT

Increased usage of wind-tunnel model data has caused growing concern about the effects of scale or Reynolds number.

An investigation has been conducted to determine the scale effect on model rotor pressure-distribution measurements for the experimental equipment used herein. The general conclusion has been reached that for the simulated flight conditions of  $\mu = 0.22$  no appreciable error was introduced because of scale effect. For the condition of  $\mu = 0.30$ , the region around the  $\alpha_r$  contour of  $11^\circ$  appears to be somewhat affected by Reynolds number (figs. 43 and 44). This conclusion is in reasonable agreement with the results published in reference 6. For Reynolds numbers less than those representative of full scale, the major effect is seen to be (fig. 4 of ref. 6) a reduction in the maximum lift coefficient  $C_{L_{max}}$ ; therefore, if model pressure measurements are limited to angles of attack less than those of  $C_{L_{max}}$  for the Reynolds numbers involved, no appreciable scale effect will be introduced.

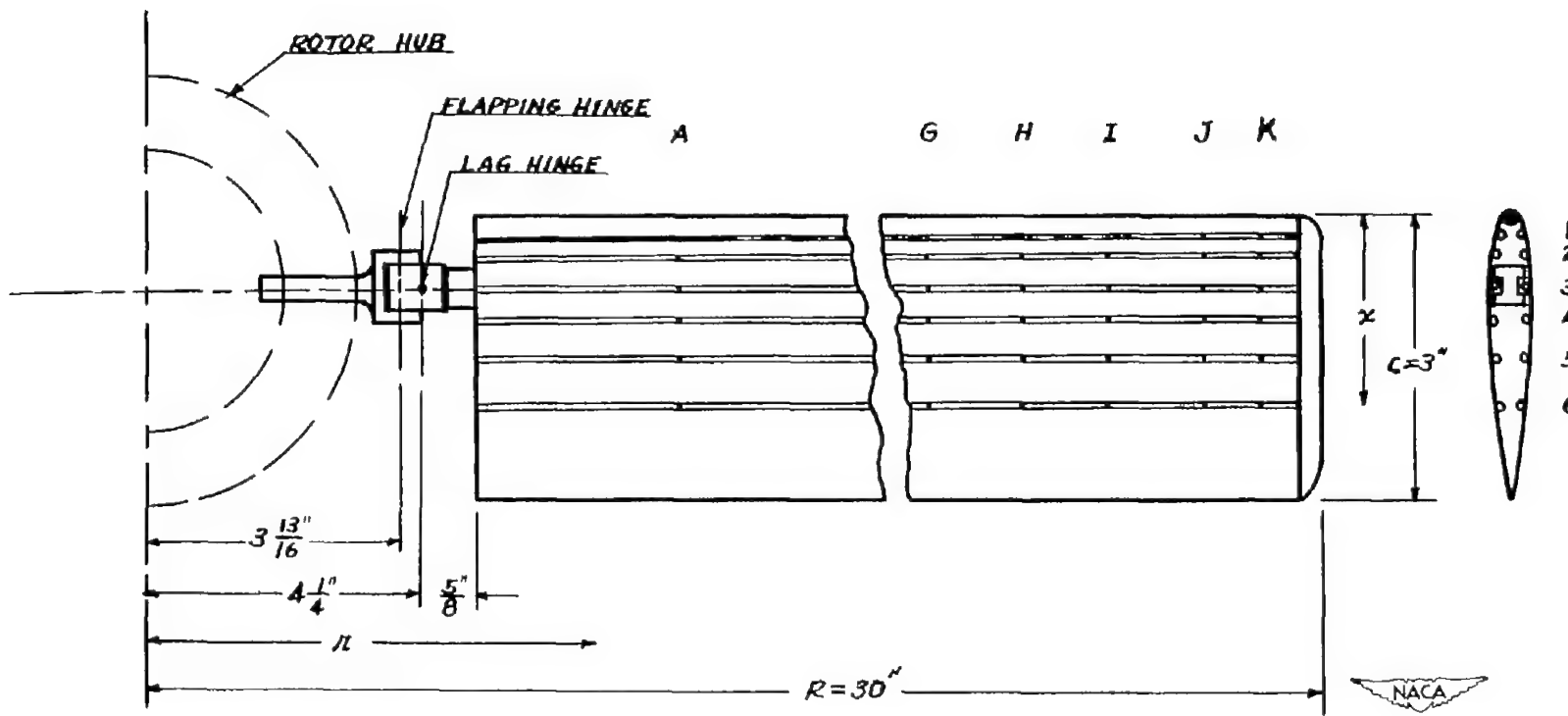
The curves of figure 43 show the sectional lift characteristics of the model rotor blade tested as a wing of aspect ratio 8 at representative values of Reynolds number which the outer portion of the blade experienced during one cycle at  $\mu = 0.30$ . The inner portion of the model blade experienced much larger angles of attack as represented in figure 45 which is also characteristic of full scale. For the condition of  $\mu = 0.30$  the inner portion of the blade contributed no positive lift in the region of  $\psi = 270^\circ$ . Pressure measurement on this portion of the blade for both full scale and model would of necessity include, in part, completely stalled and low negative velocity regions. Therefore the pressure variations due to low Reynolds number effect on the inner portion of the model blade in the critical region of the retreating half of the cycle are of course no more avoidable than in the case of full scale.

For the simulated flight conditions of  $\mu = 0.22$ , with  $\theta = 8^\circ$  and  $\alpha = -5^\circ$  as analyzed, no scale correction was necessary. Although the conditions of  $\mu = 0.50$ ,  $\xi = 0$ , and  $\theta = 8^\circ$  and  $\mu = 1.0$ ,  $\xi = 0.13$ , and  $\theta = 4^\circ$  were not investigated in detail for scale effect, brief considerations of the problem indicated that only a comparatively small percent of the total rotor disk was affected. In order to determine accurately the extent of scale effect, each rotor condition needs to be analyzed for angle-of-attack distribution in the critical region of

the disk. No attempt has been made to consider the problem to this extent; however, it can be reasonably assumed that the data included in this report are indicative of the actual full-scale pressure distributions for the rotor conditions simulated.

## REFERENCES

1. Coleman, Robert P., Feingold, Arnold M., and Stempin, Carl W.: Evaluation of the Induced-Velocity Field of an Idealized Helicopter Rotor. NACA WR L-126, 1945. (Formerly NACA ARR L5E10.)
2. Mangler, K. W.: Calculation of the Induced Velocity Field of a Rotor. Rep. No. Aero. 2247, British R.A.E., Feb. 1948.
3. Drees, Meijer, Jr.: A Theory of Airflow Through Rotors and Its Application to Some Helicopter Problems. The Jour. Helicopter Assoc. (Great Britian), vol. 3, no. 2, July-Aug.-Sept. 1949, pp. 79-104.
4. Meyer, John R., Jr.: An Investigation of Bending-Moment Distribution on a Model Helicopter Rotor Blade and a Comparison With Theory. NACA TN 2626, 1952.
5. Meyer, John R., Jr., and Falabella, Gaetano, Jr.: The Effect of Blade Mass Constant and Flapping Hinge Offset on Maximum Blade Angles of Attack at High Advance Ratios. Proc. Eighth Annual Forum, Am. Helicopter Soc., Inc., May 15-17, 1952.
6. Jacobs, Eastman N., and Sherman, Albert: Airfoil Section Characteristics as Affected by Variations of the Reynolds Number. NACA Rep. 586, 1937.



CHORD STATION	$x/c$	$x, \text{ in.}$
1	0.083	$\frac{1}{4}$
2	.156	$\frac{15}{32}$
3	.271	$\frac{13}{16}$
4	.375	$1\frac{1}{8}$
5	.500	$1\frac{1}{2}$
6	.674	$2\frac{13}{32}$

SPAN STATION	$r/R$	$r, \text{ in.}$	SPAN STATION	$r/R$	$r, \text{ in.}$
A	0.325	9.75	G	0.525	24.75
B	.460	13.80	H	.860	25.80
C	.590	17.70	I	.890	26.70
D	.660	19.80	J	.925	27.75
E	.725	21.75	K	.960	28.80
F	.790	23.70	L	.977	29.30

Figure 1.- Location of pressure orifices.

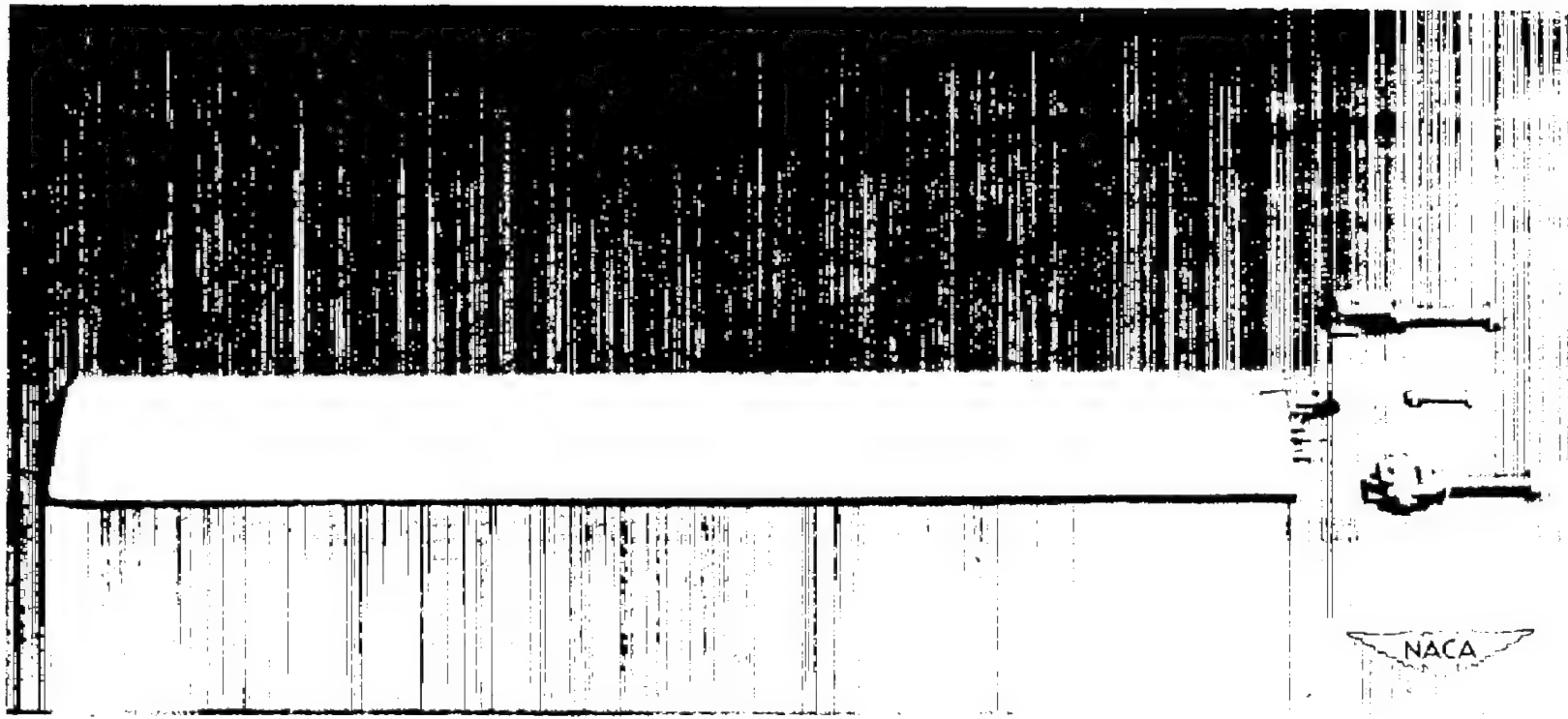


Figure 2.- Rotor blade with root adapters.

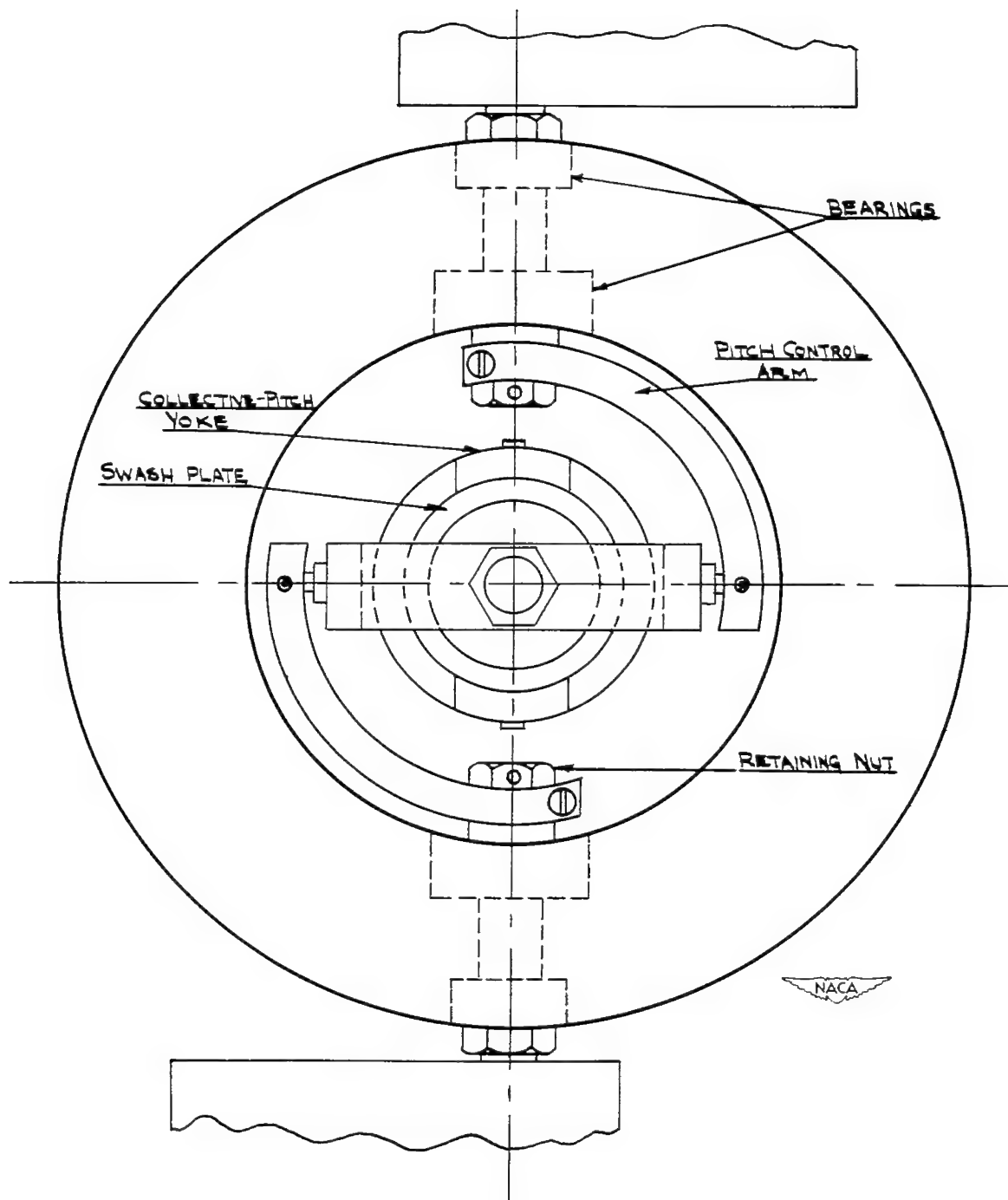


Figure 3.- Rotor hub plan view.

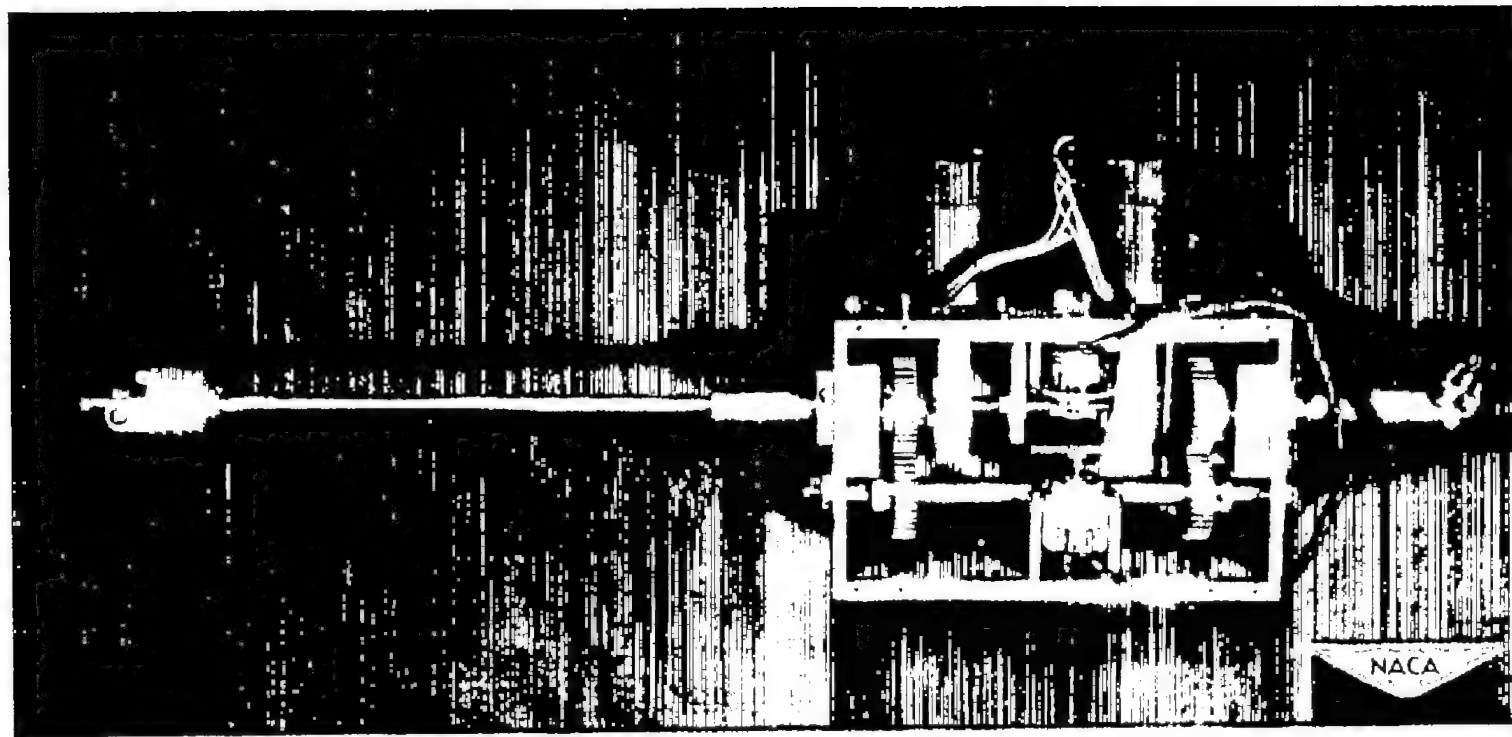


Figure 4.- Gearbox and control-rod detail.

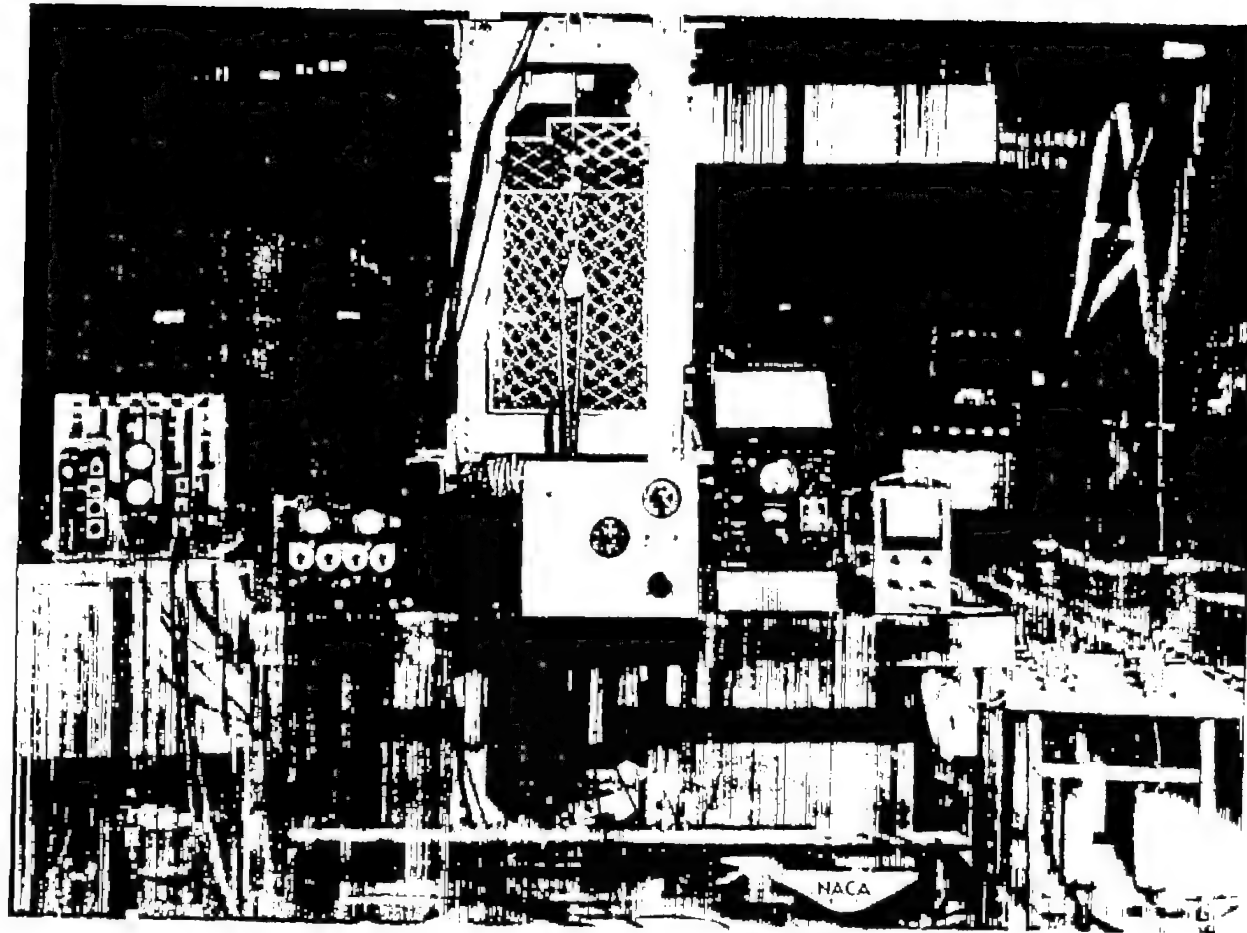


Figure 5.- Control and recording equipment.

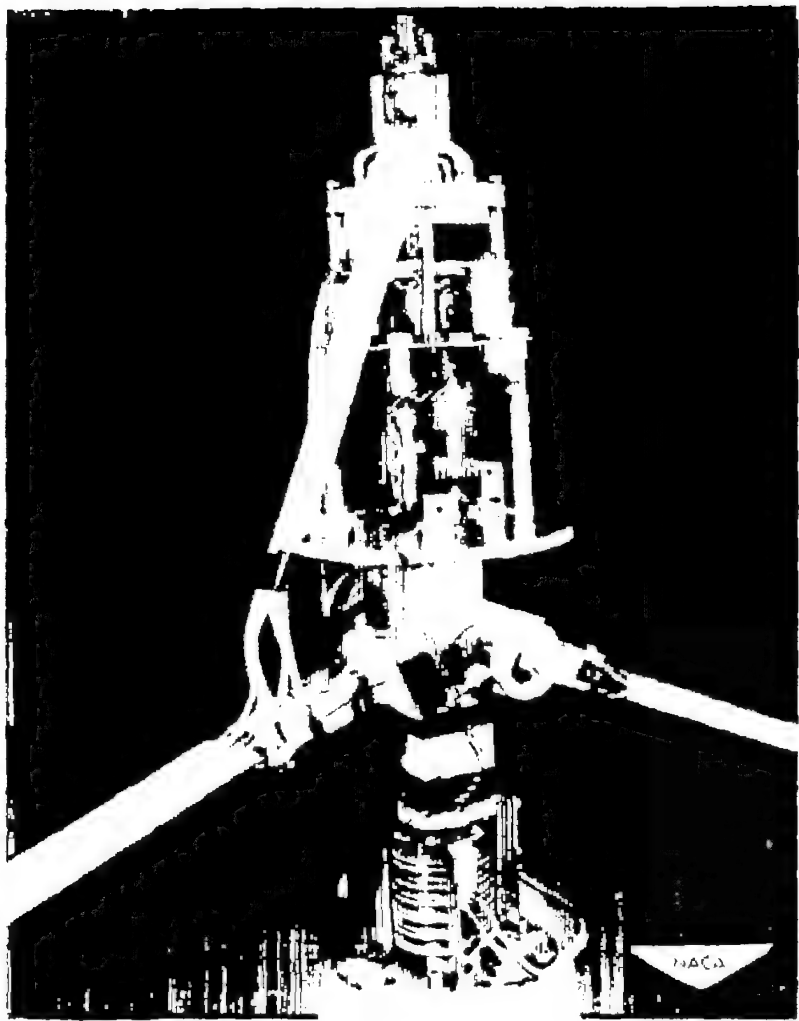


Figure 6.- Hub assembly of zero-offset rotor.

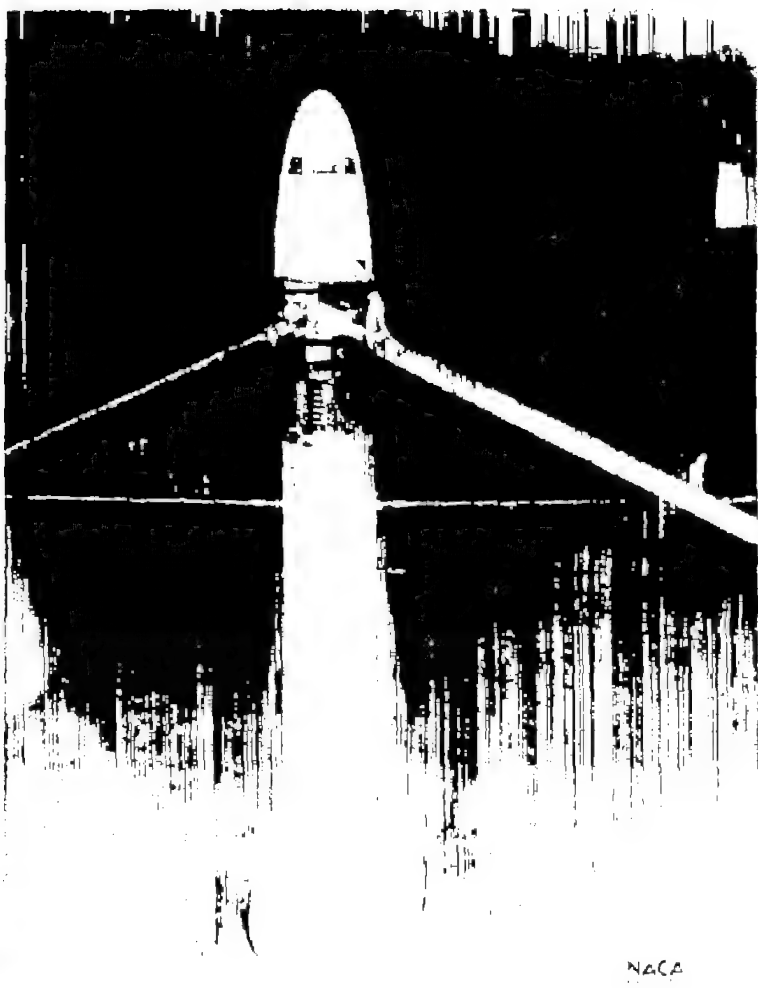


Figure 7.- Downstream view of zero-offset rotor in wind tunnel.

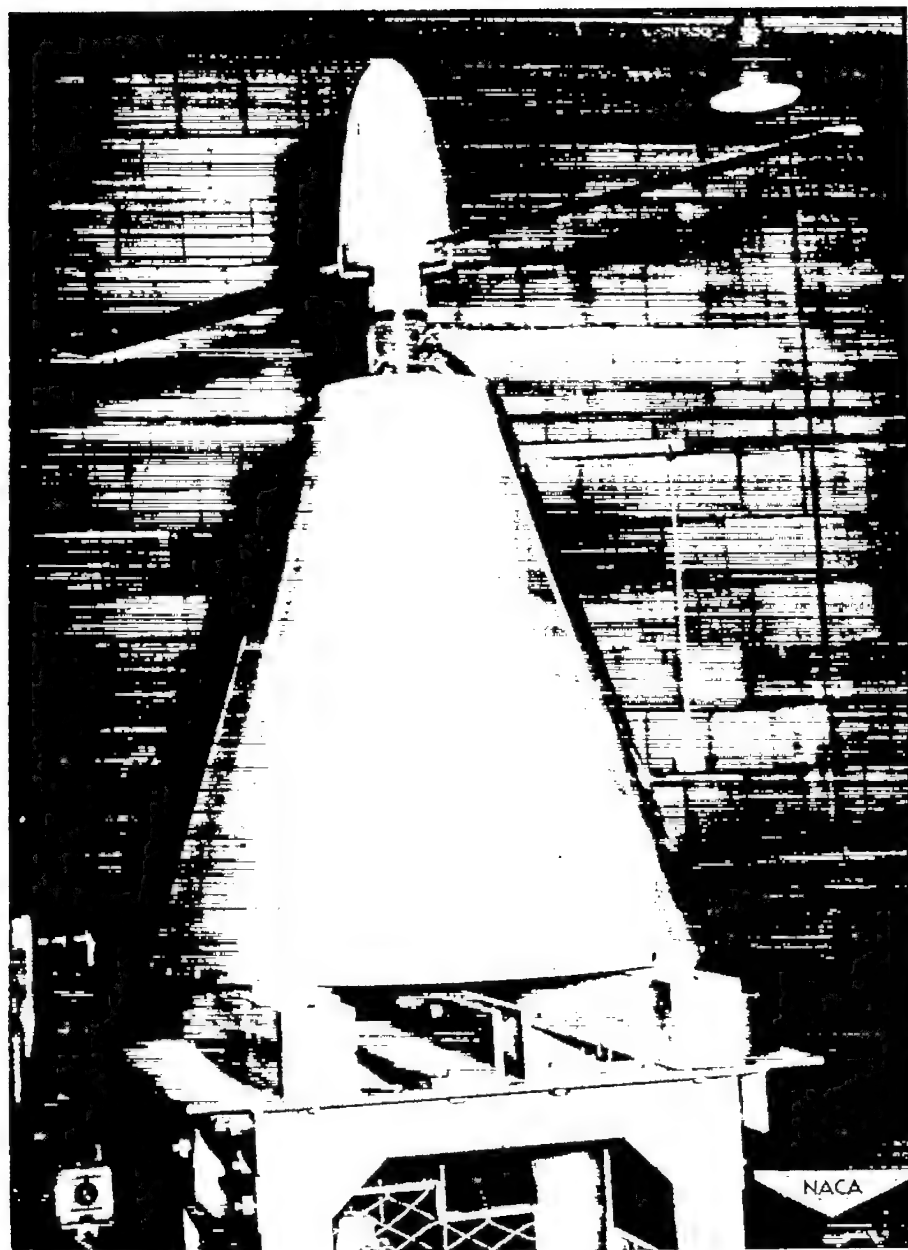


Figure 8.- Rotor on hovering mount.

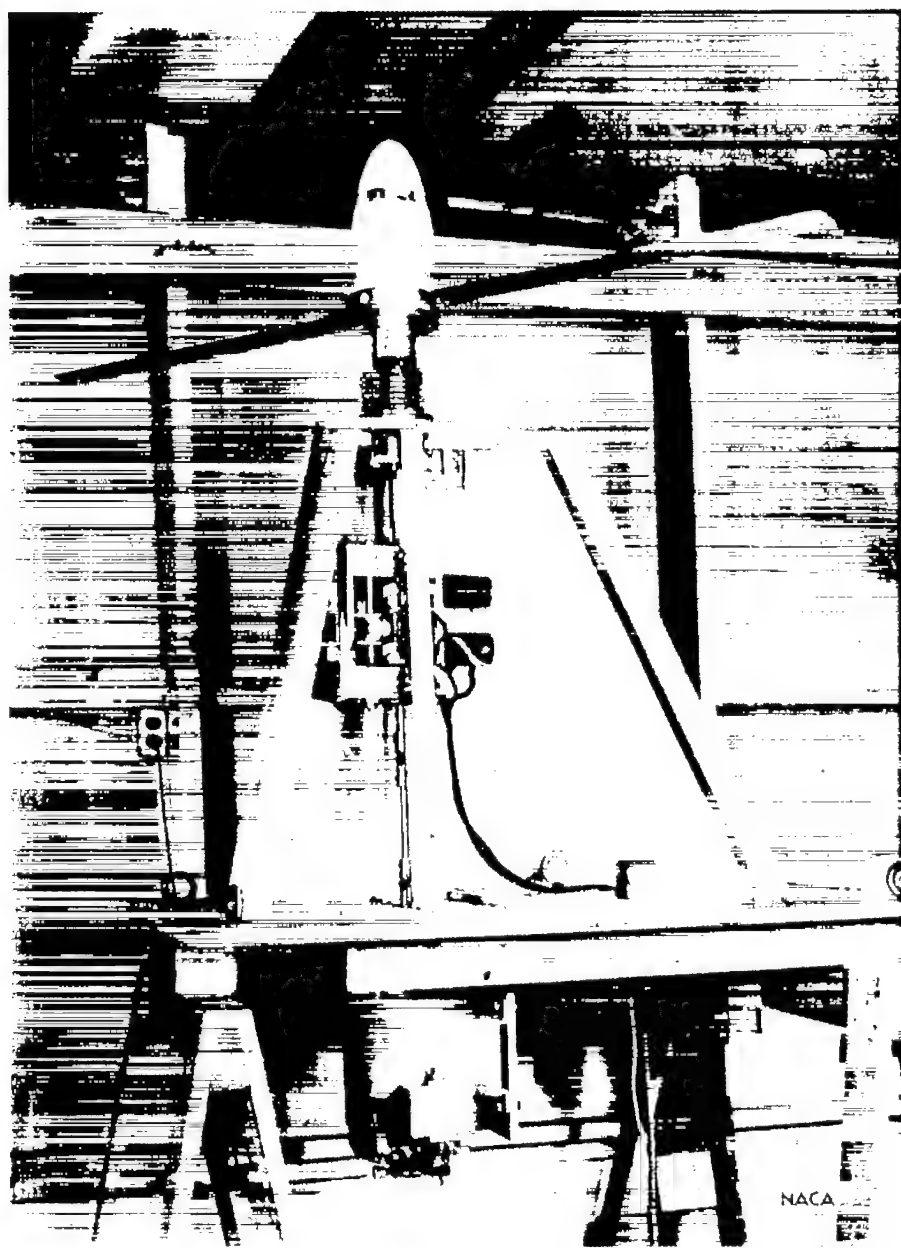


Figure 9.- Wind-tunnel mount.

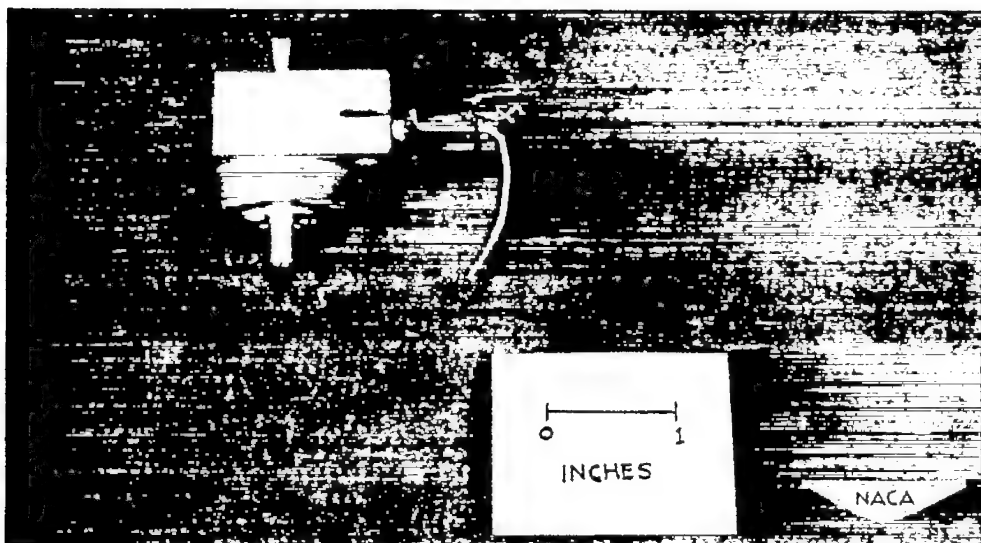


Figure 10.- Pressure pickup.

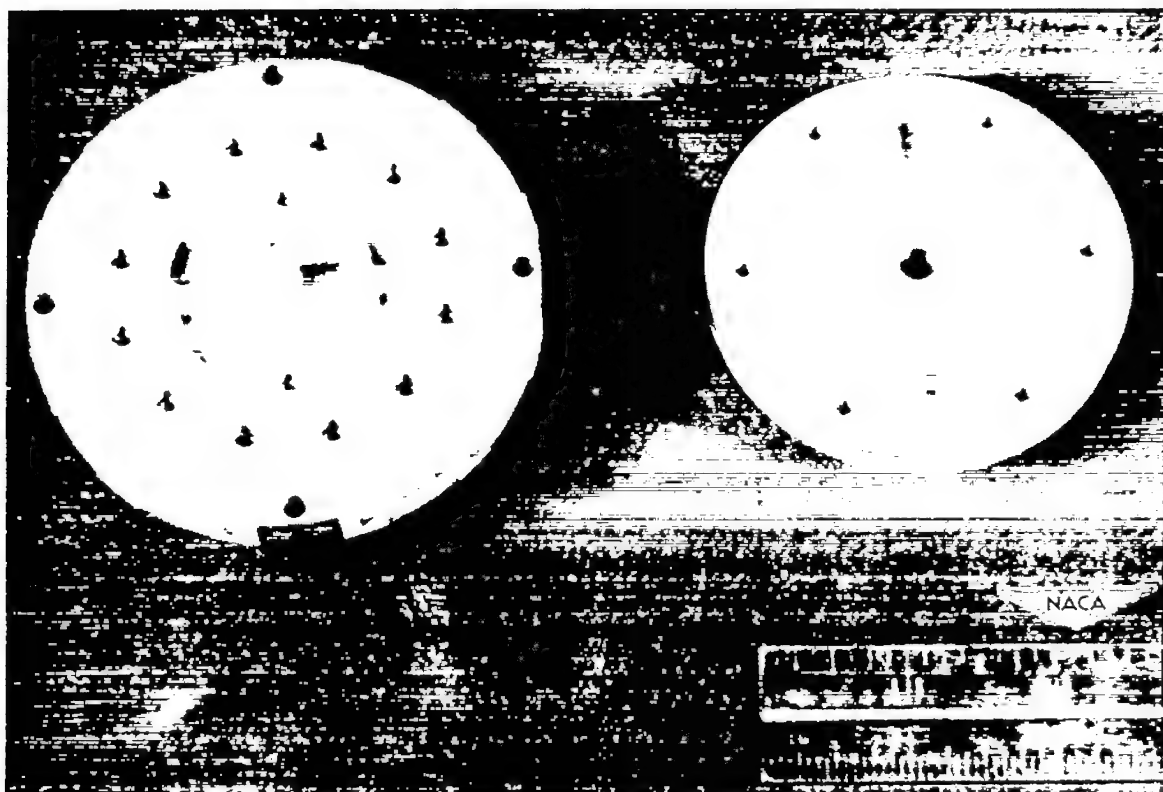


Figure 11.- Mating surfaces of pressure switch.

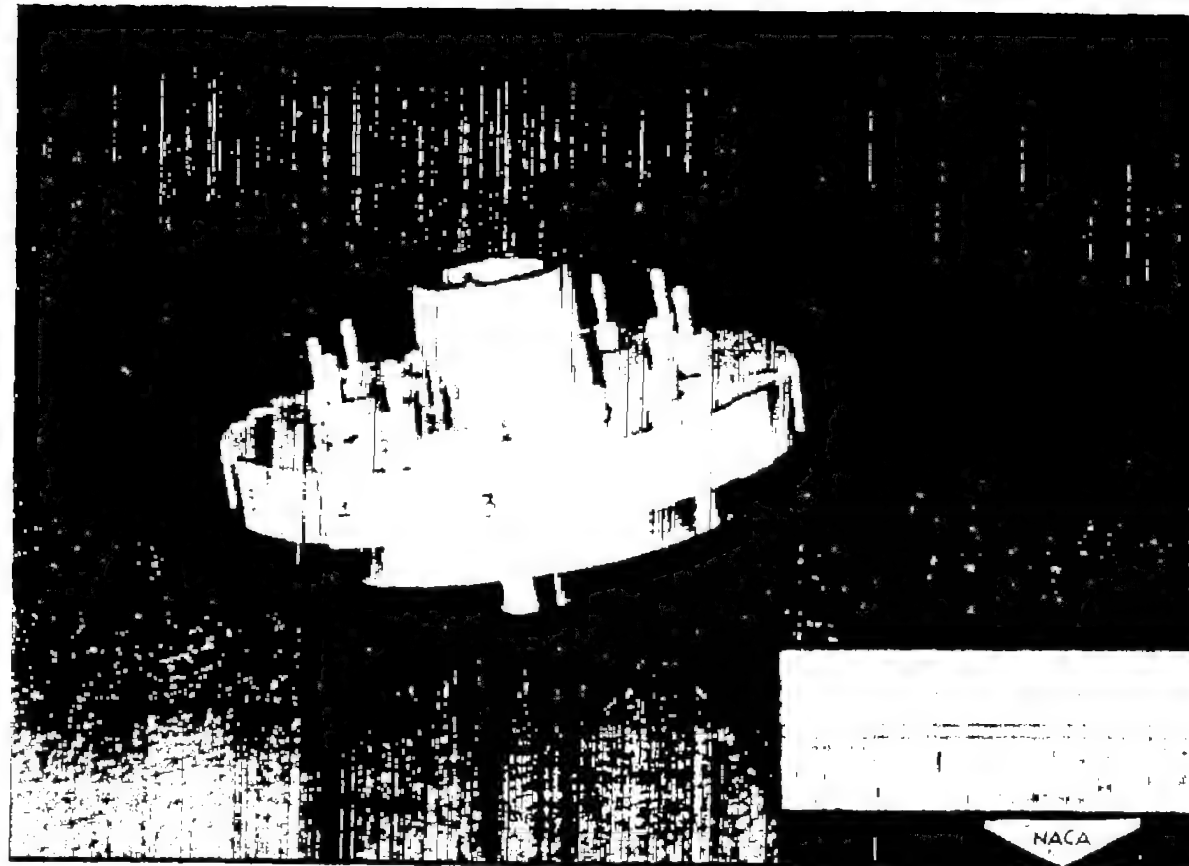


Figure 12.- Pressure switch assembled.

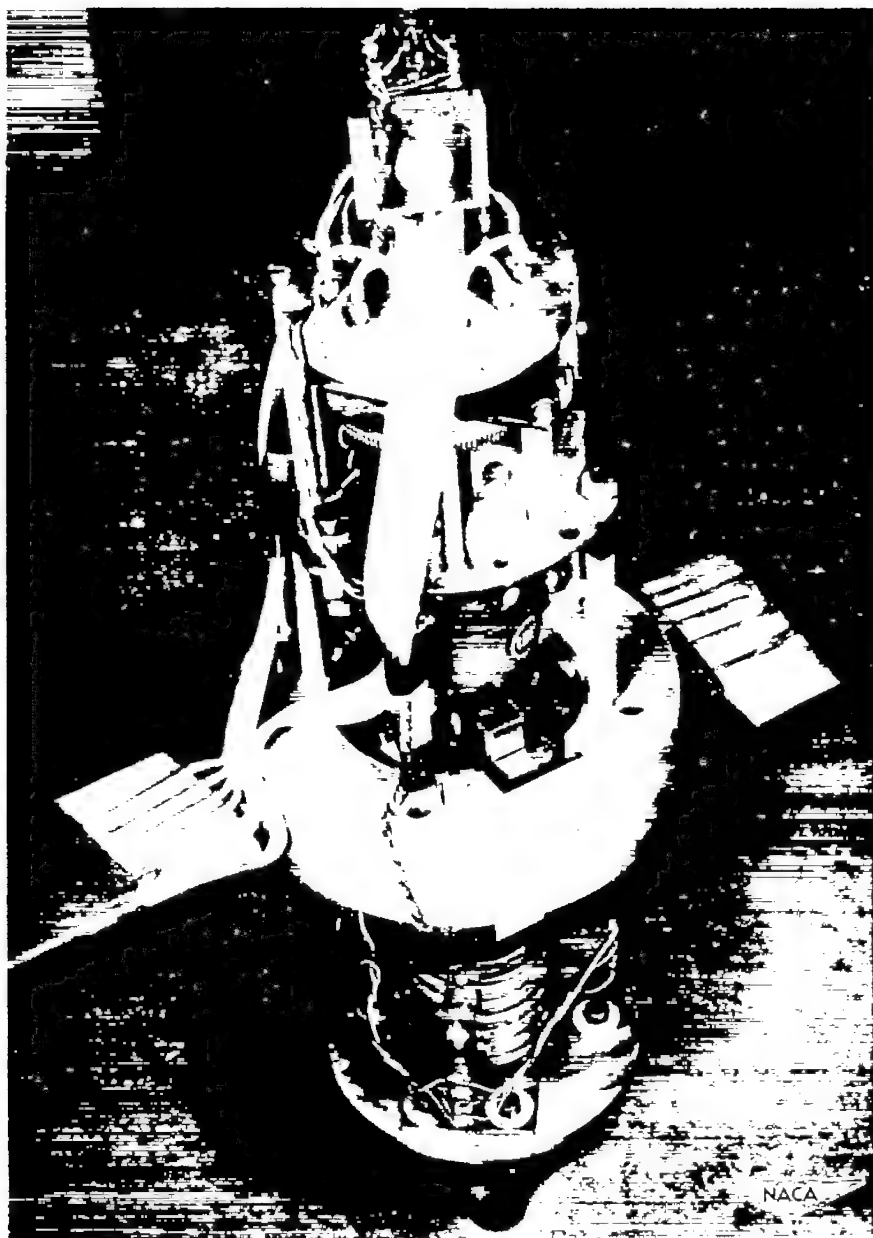
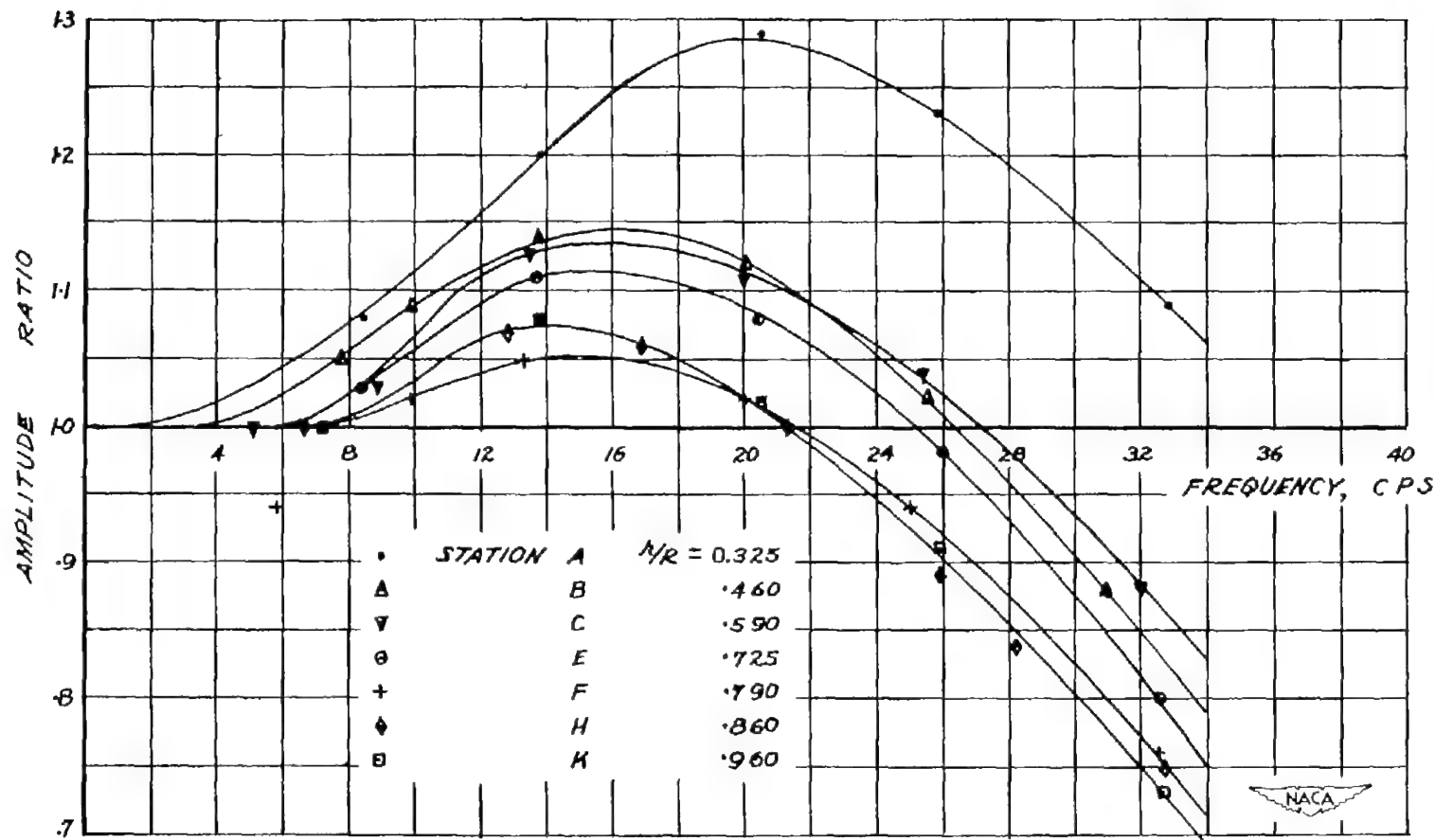


Figure 13.- Rotor hub detail.

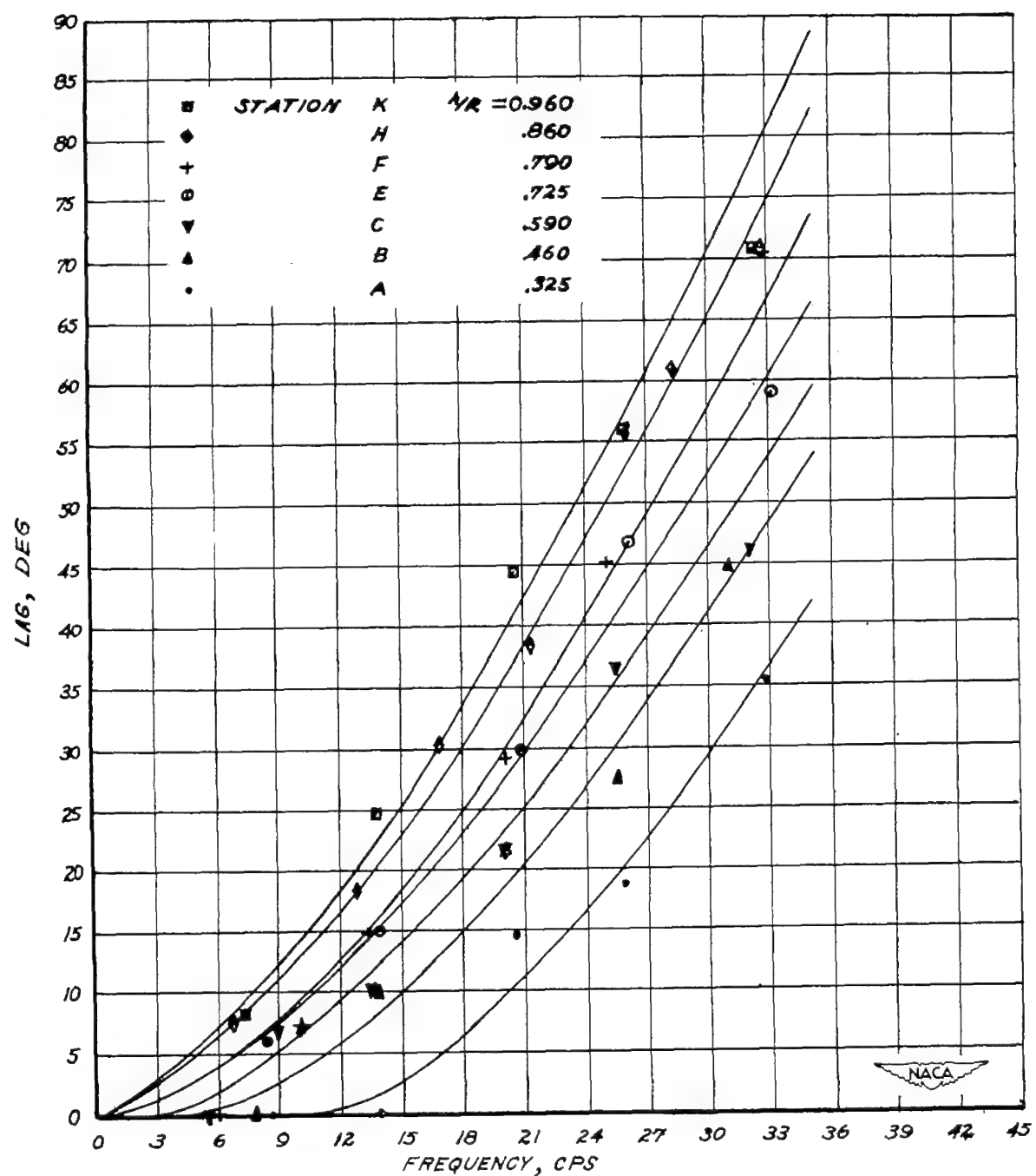


Figure 14.- Dynamic calibration of pressure measuring system.



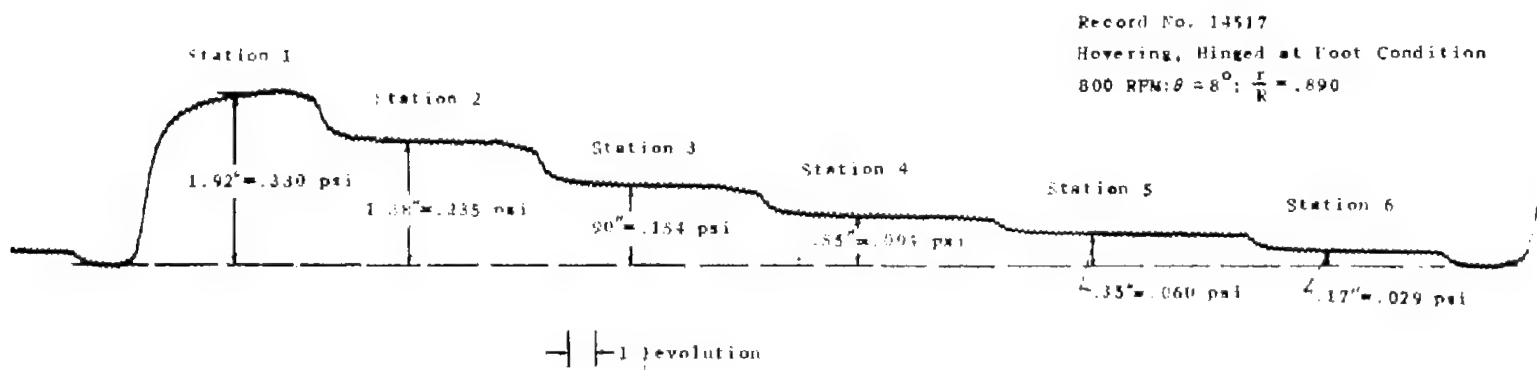
(a) Amplitude ratio against frequency.

Figure 15.- Dynamic response of pressure measuring system.



(b) Lag against frequency.

Figure 15.- Concluded.



NACA

Figure 16.- Sample oscillograph record of chordwise pressure distribution on 13-percent-offset rotor in hovering condition.

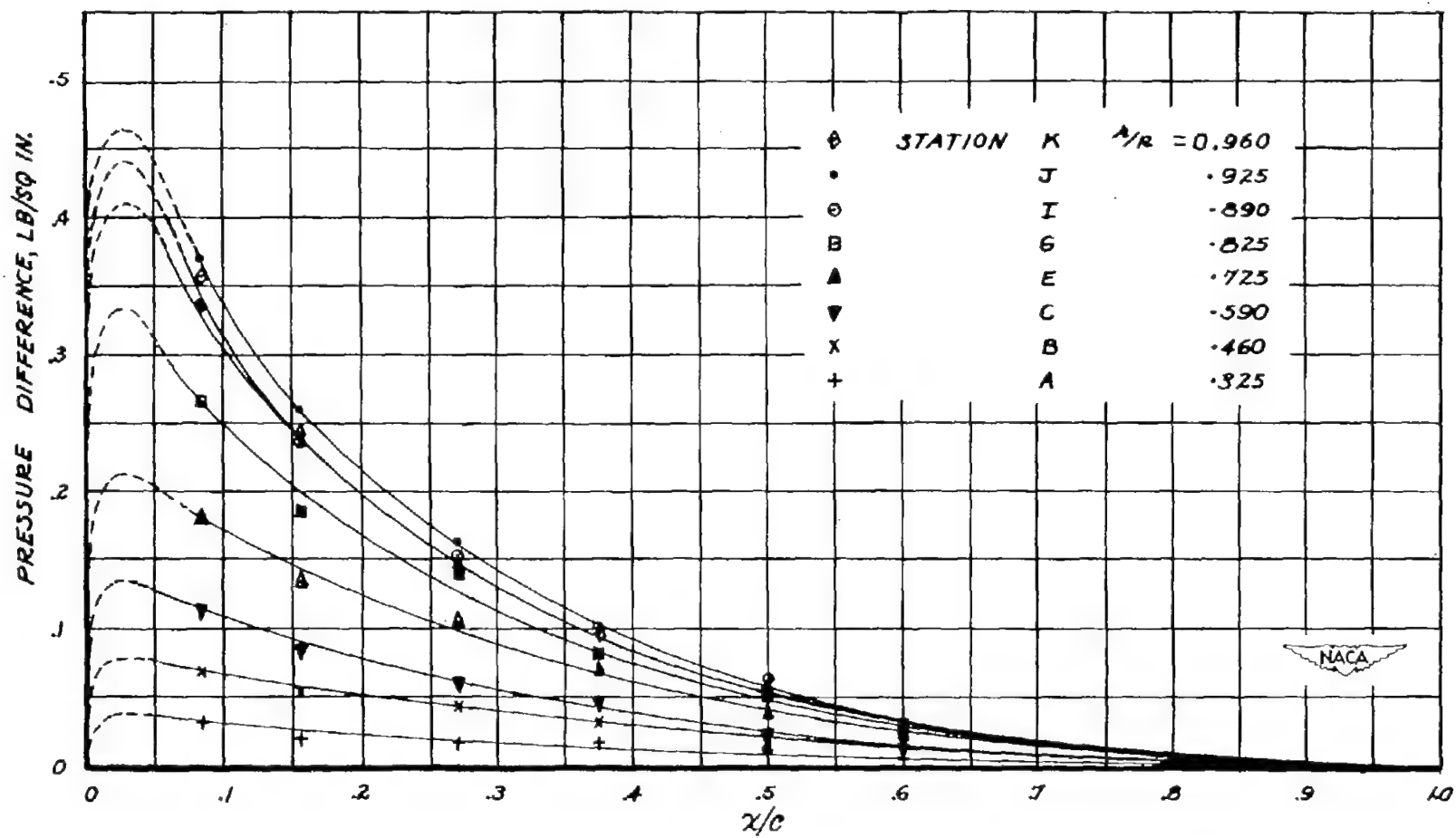


Figure 17.- Chordwise pressure distribution on hinged-at-root rotor blade.  
Profile, NACA 0015; condition, hovering; speed, 800 rpm;  $\theta = 8^\circ$ .

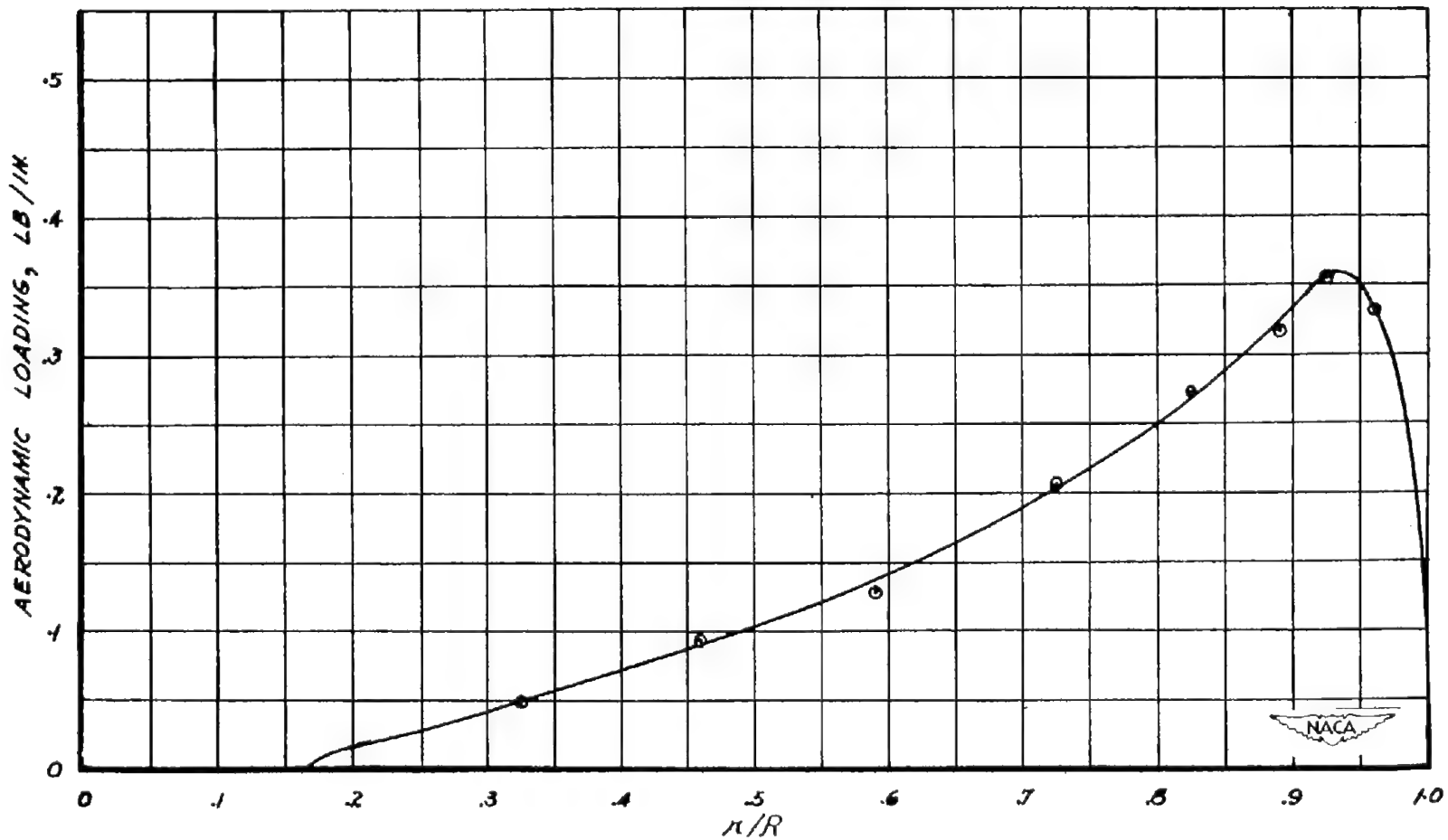


Figure 18.- Spanwise aerodynamic loading on hinged-at-root rotor blade.  
Profile, NACA 0015; condition, hovering; speed, 800 rpm;  $\theta = 8^\circ$ .

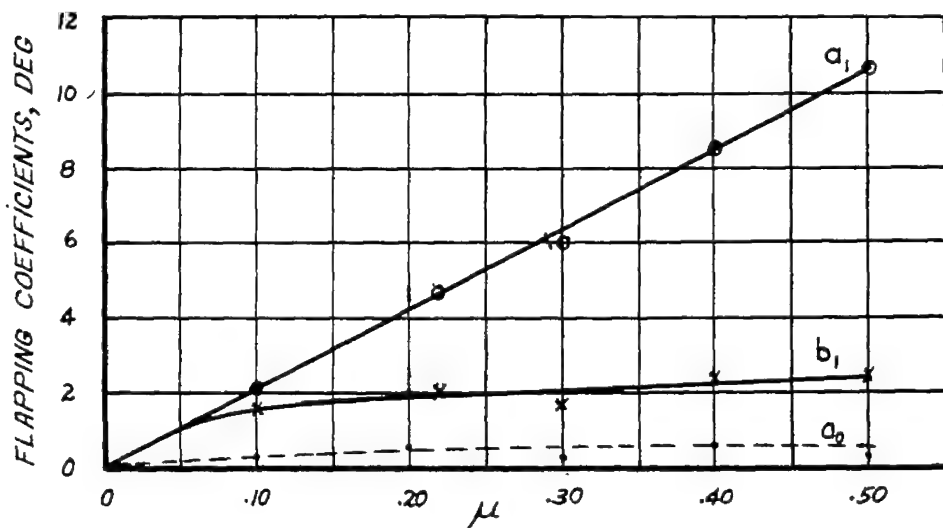
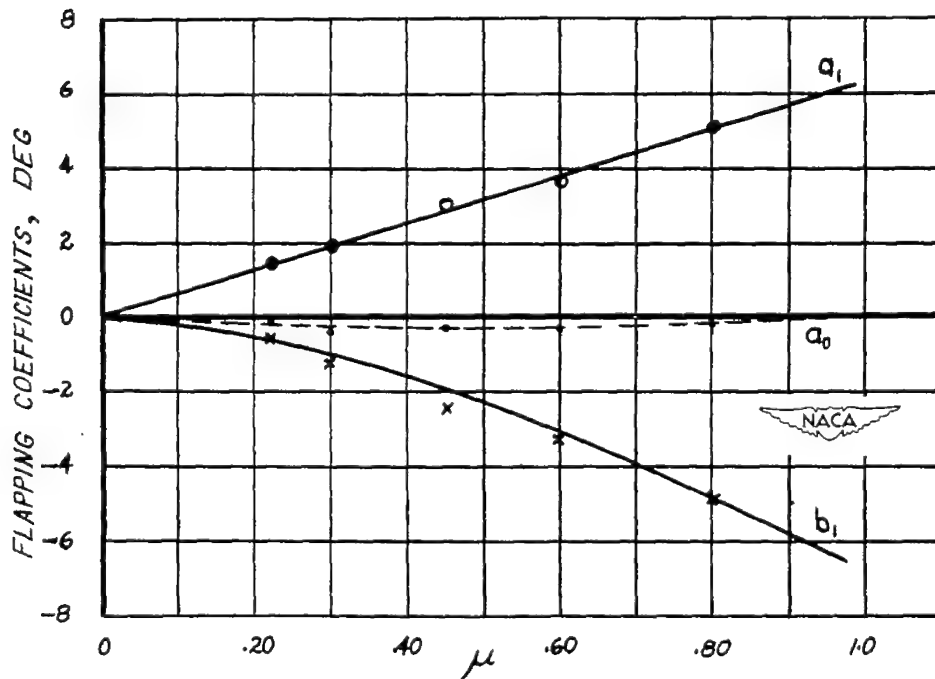
(a)  $\xi = 0.$ (b)  $\xi = 0.13.$ 

Figure 19.- Experimental variations of  $a_0$ ,  $a_1$ , and  $b_1$  with  $\mu$  for  $\xi = 0$  and  $\xi = 0.13$ . Profile, NACA 0015;  $\theta = 8^\circ$ ;  $\alpha = -5^\circ$ ;  $R = 2.5$  feet.

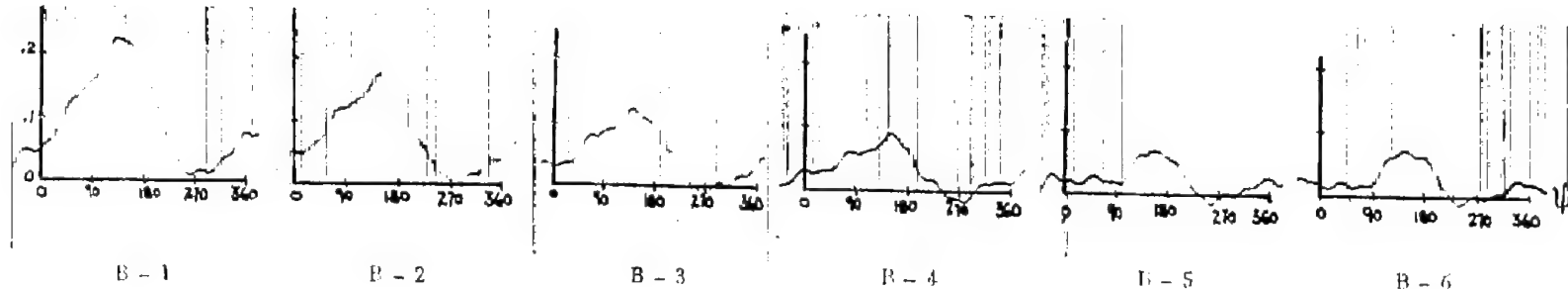
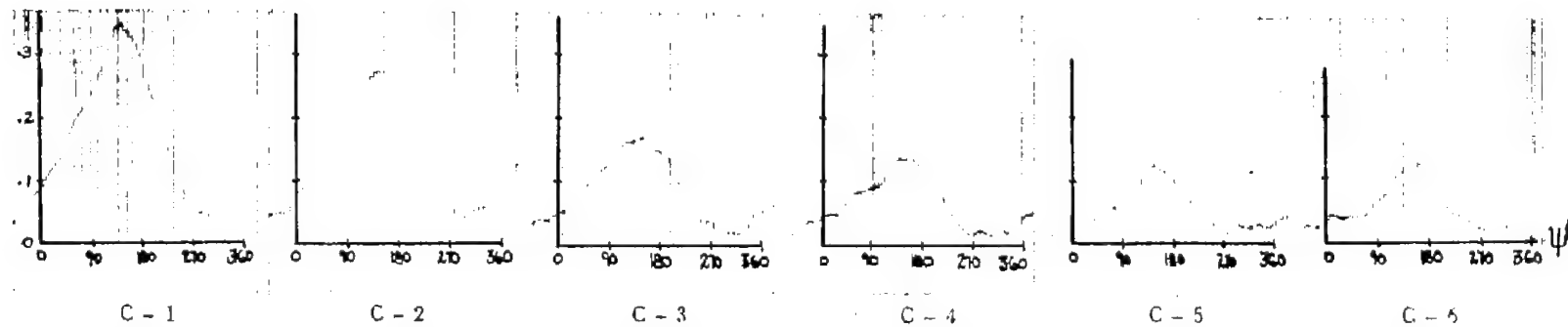
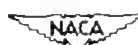
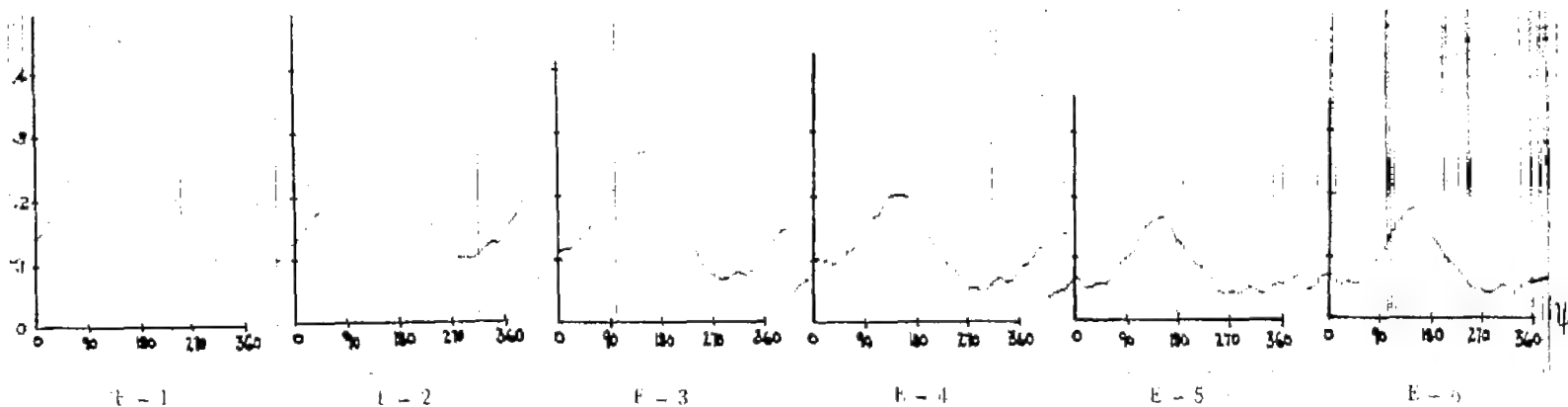
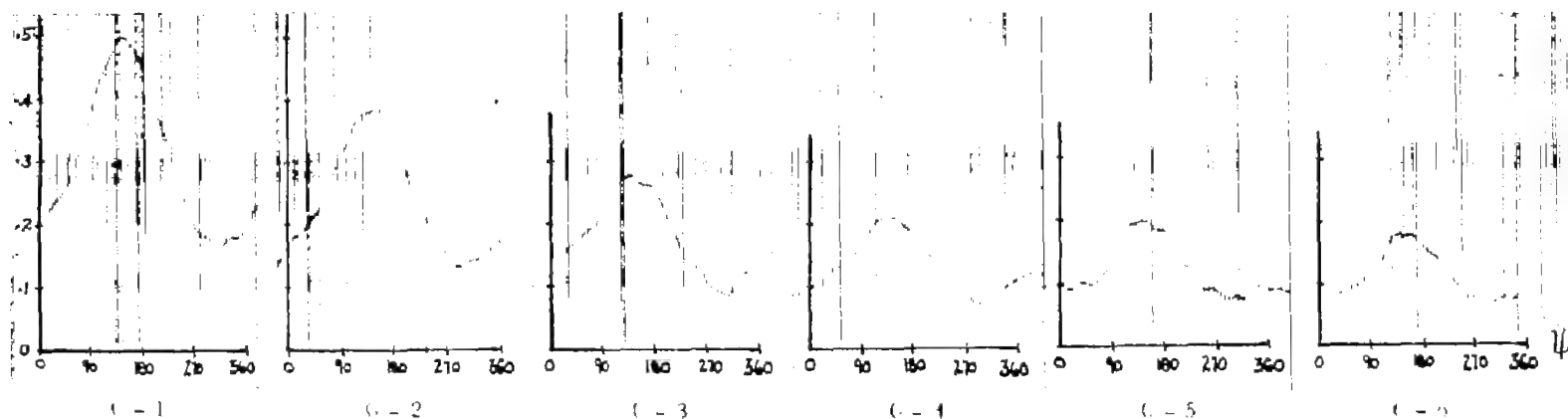
(a) Span station B;  $r/R = 0.460$ .(b) Span station C;  $r/R = 0.590$ .

Figure 20.- Pressure difference in pounds per square inch against azimuth in degrees. Profile, NACA 0015; speed, 800 rpm;  $\xi = 0.13$ ;  $\mu = 0.22$ ;  $\theta = 8^\circ$ ;  $\alpha = -5^\circ$ .



(c) Span station E;  $r/R = 0.725$ .



(d) Span station G;  $r/R = 0.825$ .

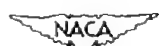


Figure 20.- Continued.

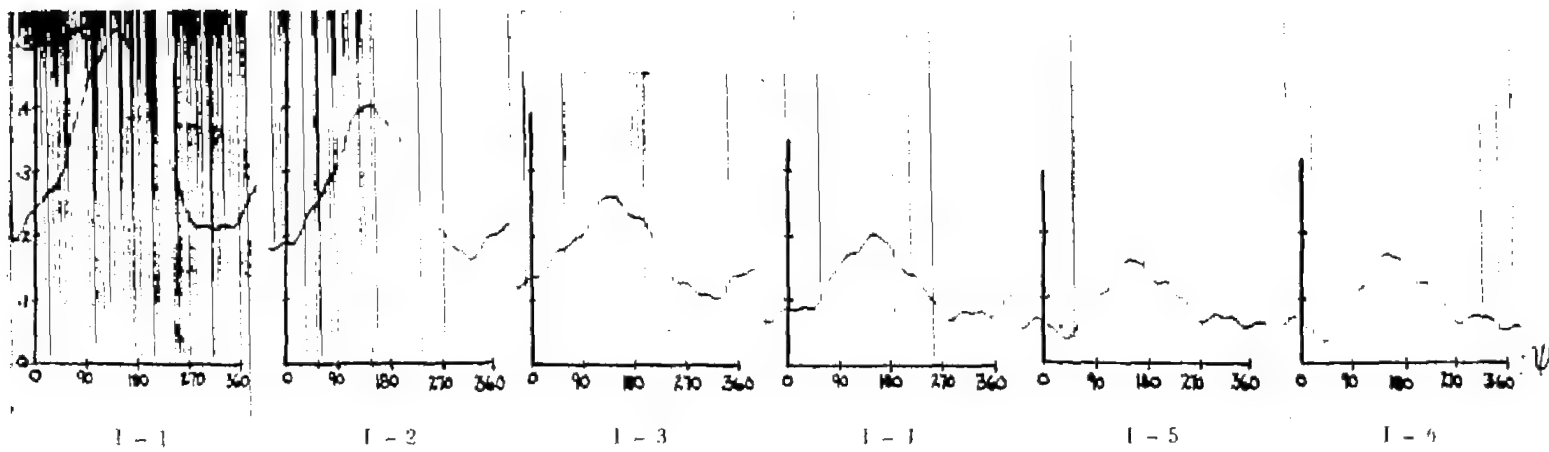
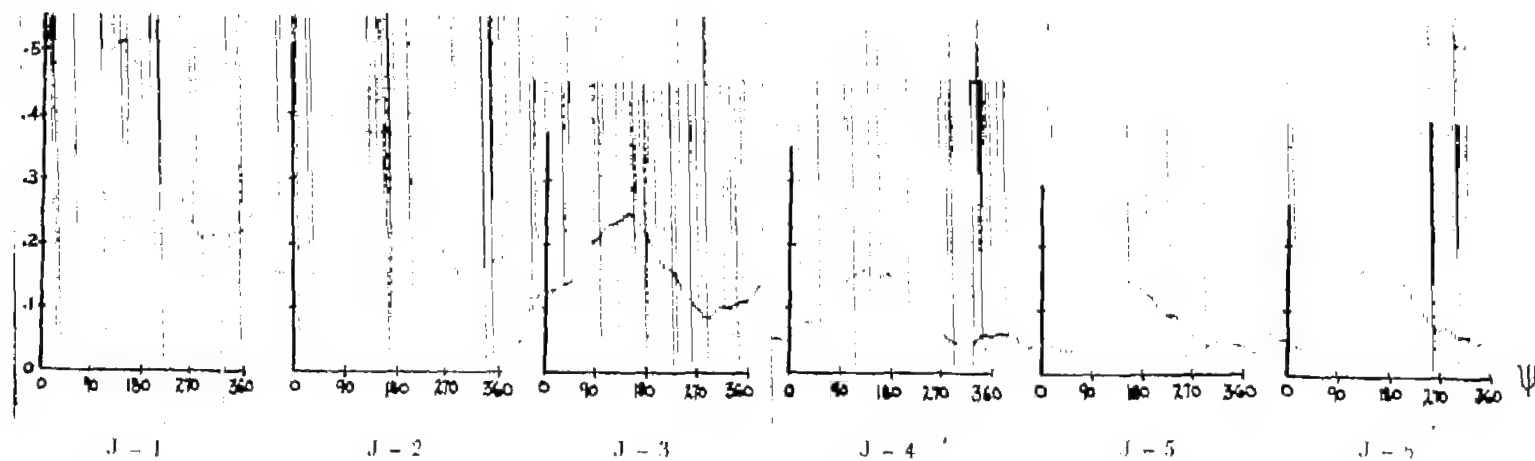
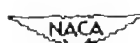
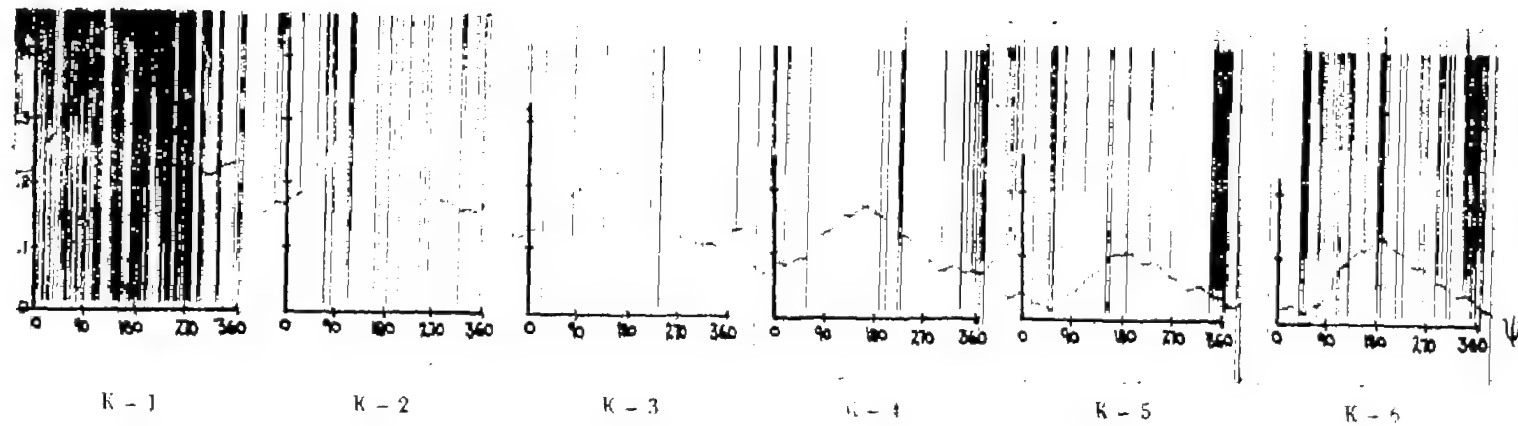
(e) Span station I;  $r/R = 0.890$ .(f) Span station J;  $r/R = 0.925$ .

Figure 20.- Continued.



(g) Span station K;  $r/R = 0.960$ .



Figure 20.- Concluded.

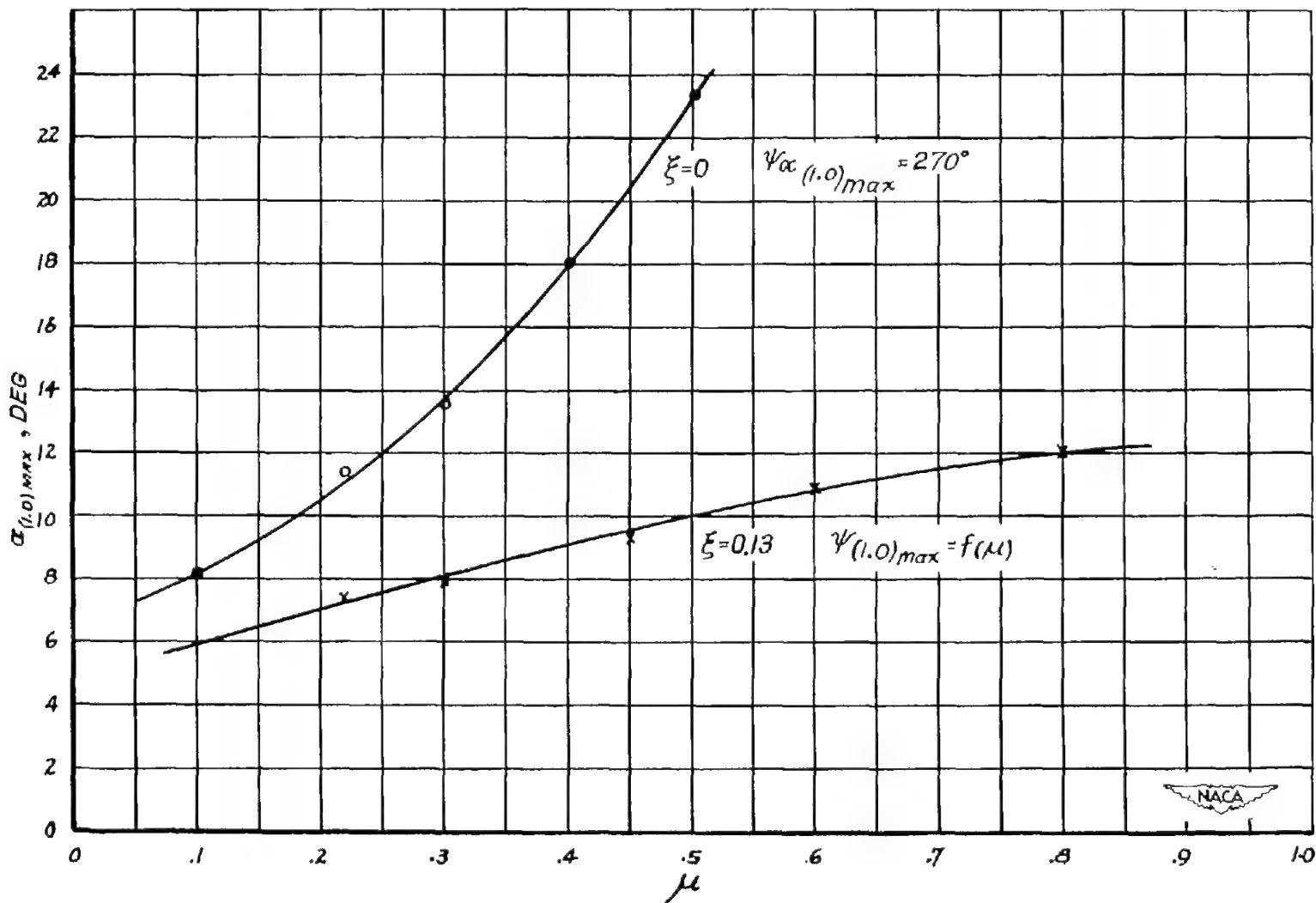
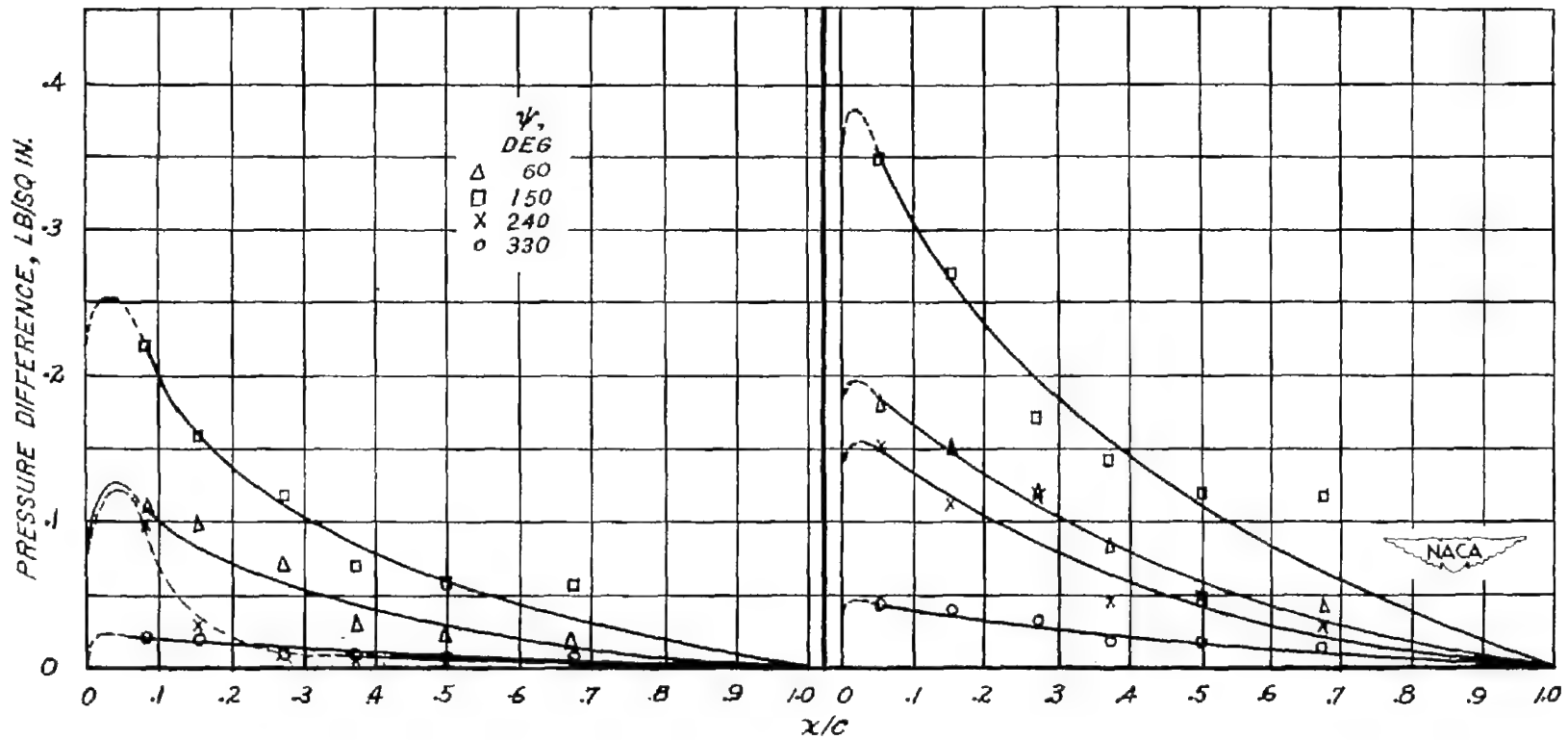


Figure 21.- Comparison of experimental maximum angles of attack at tip of rotors with offset ratios of  $\xi = 0$  and  $\xi = 0.13$ . Profile, NACA 0015;  $\theta = 8^\circ$ ;  $\alpha = -5^\circ$ ;  $\gamma = 1.8$ .



(a) Span station B;  $r/R = 0.460$ . (b) Span station C;  $r/R = 0.590$ .

Figure 22.- Chordwise pressure distribution on hinged rotor blade at various azimuth positions. Profile, NACA 0015; speed, 800 rpm;  $\xi = 0.13$ ;  $\mu = 0.22$ ;  $\theta = 8^\circ$ ;  $\alpha = -5^\circ$ .

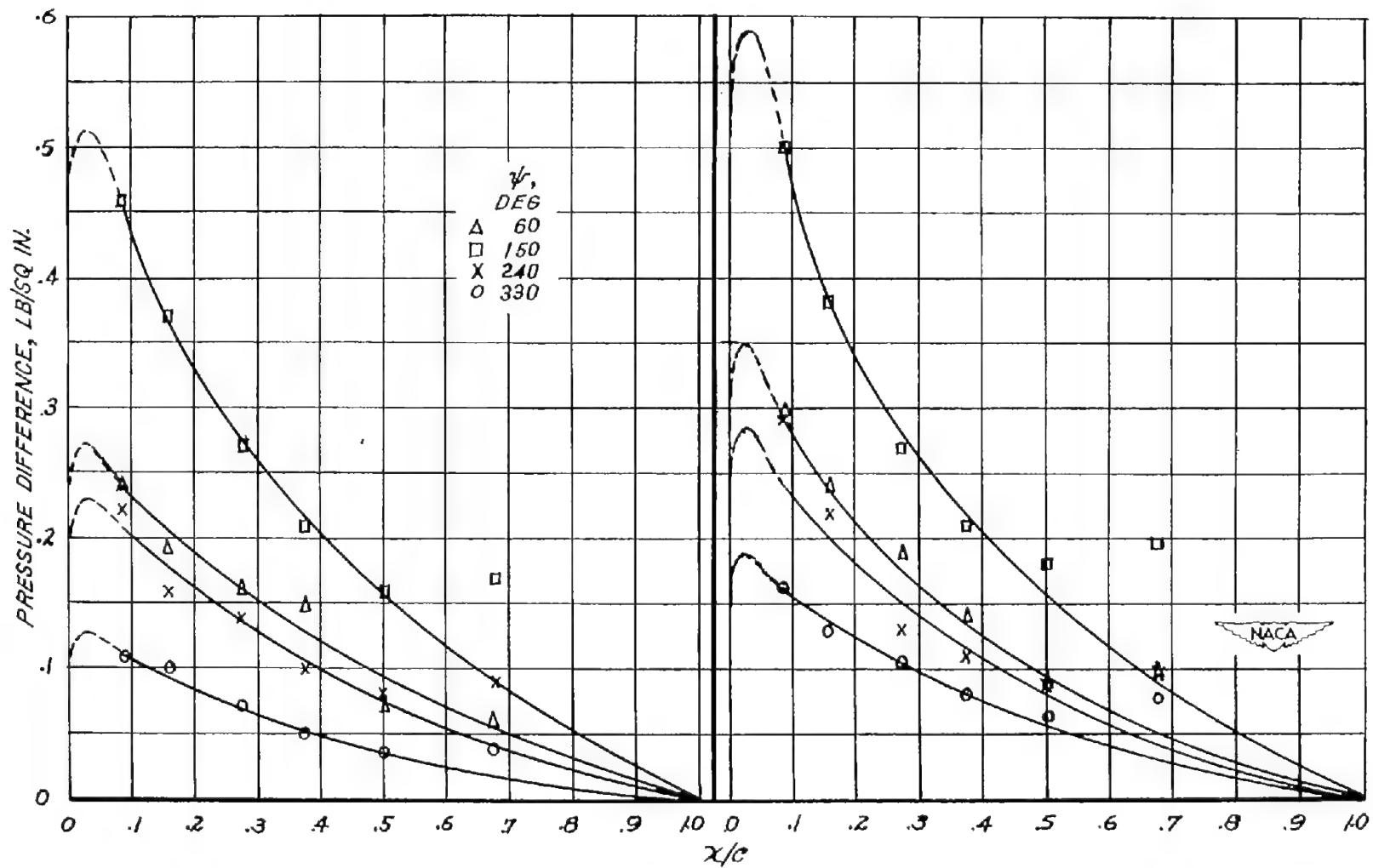
(c) Span station E;  $r/R = 0.725$ . (d) Span station G;  $r/R = 0.825$ .

Figure 22.- Continued.

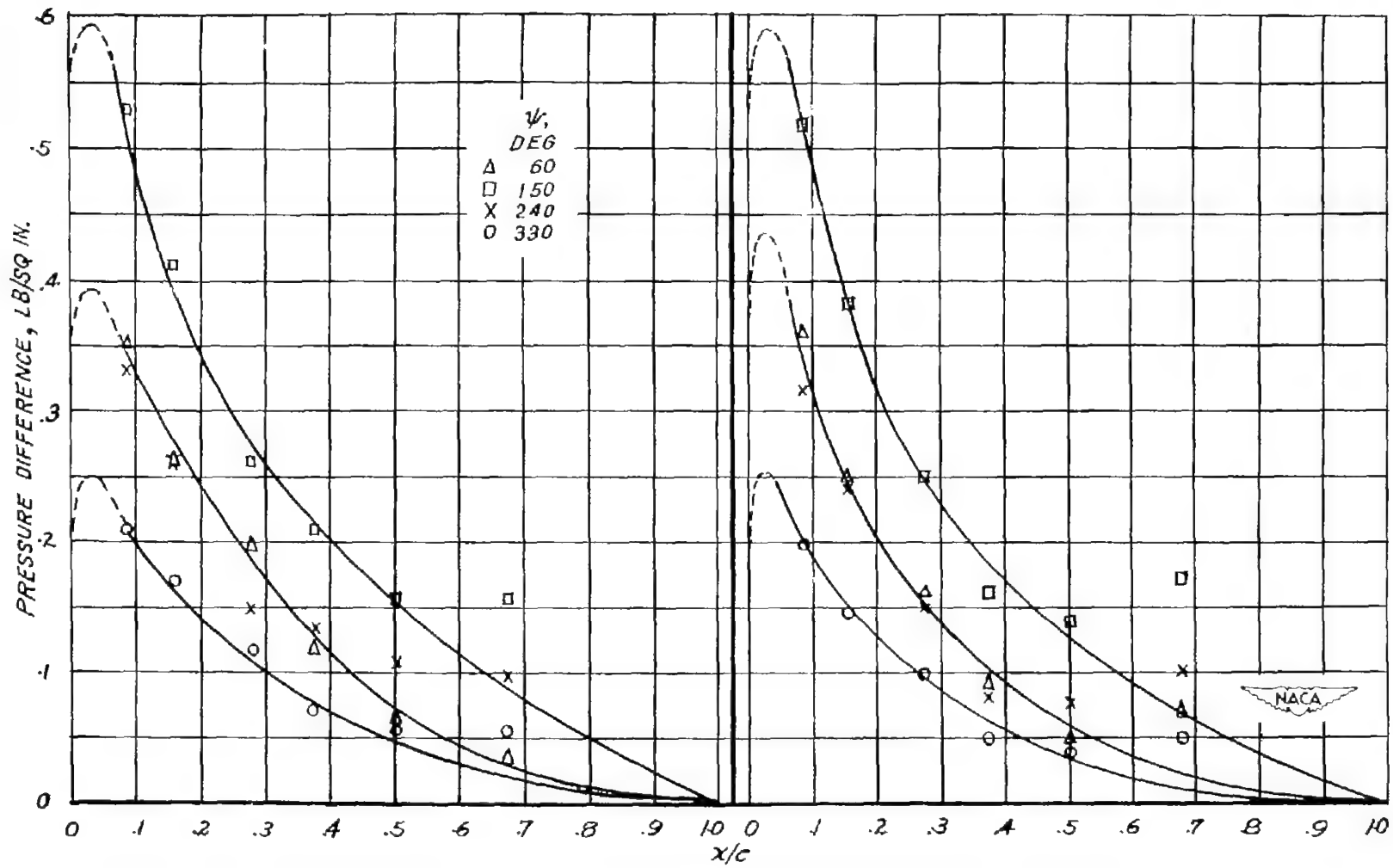


Figure 22.- Continued.

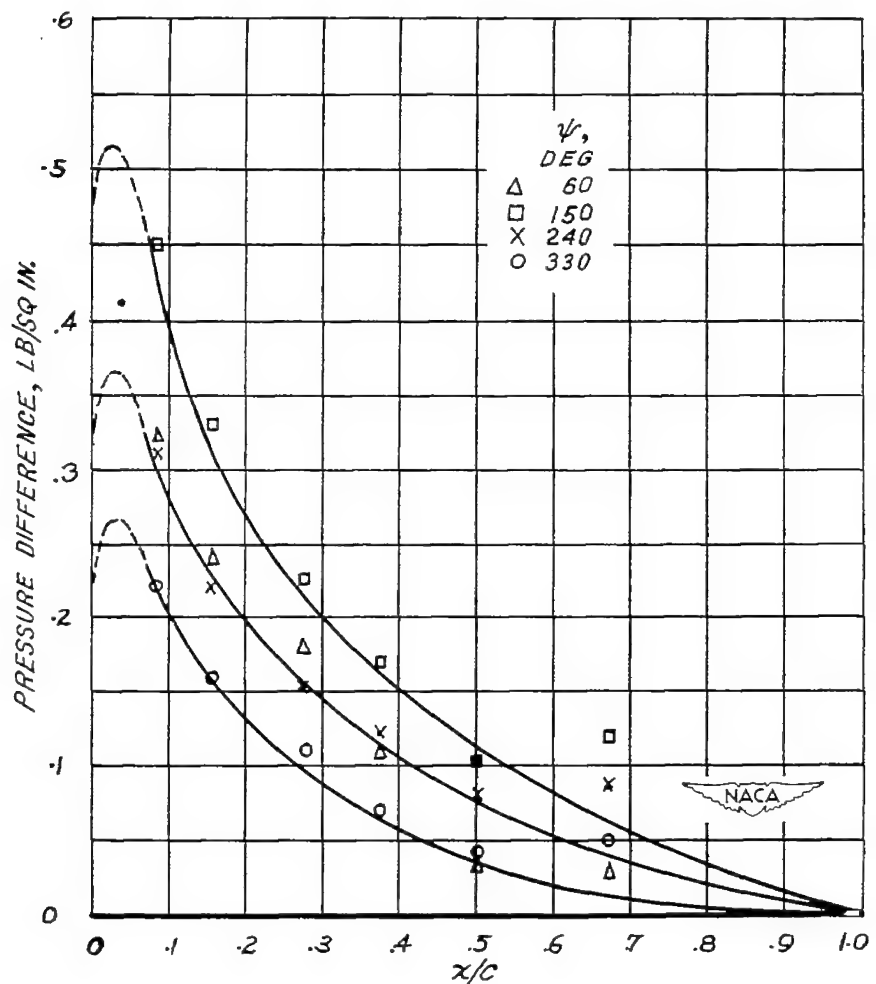
(g) Span station K;  $r/R = 0.960.$ 

Figure 22.- Concluded.

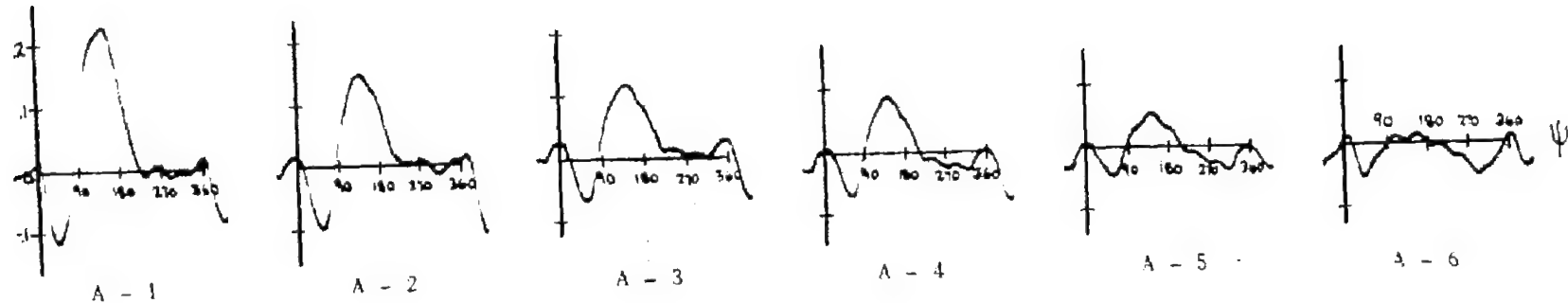
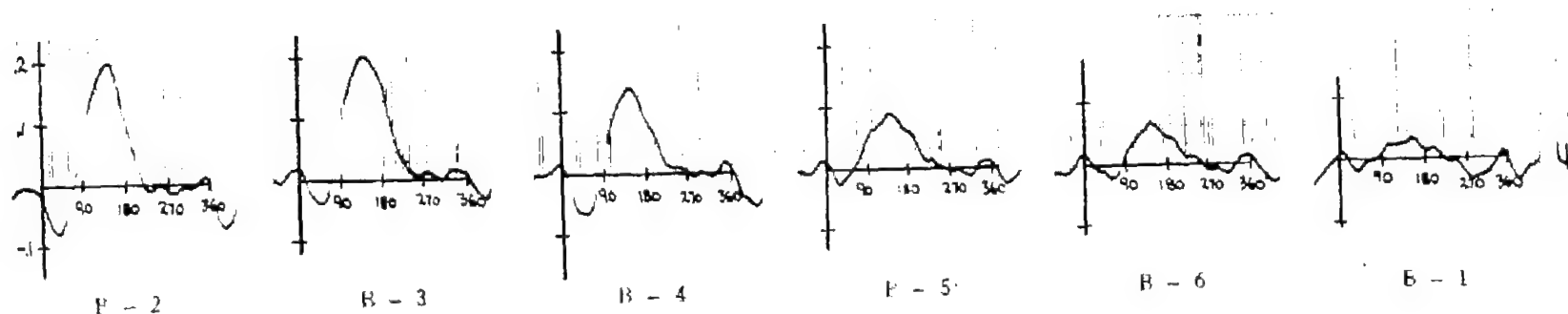
(a) Span station A;  $r/R = 0.325$ .(b) Span station B;  $r/R = 0.460$ . 

Figure 25.- Pressure difference in pounds per square inch against azimuth in degrees. Profile, NACA 0015; speed, 500 rpm;  $\xi = 0.13$ ;  $\mu = 1.0$ ;  $\theta = 4^\circ$ ;  $\alpha = -5^\circ$ .

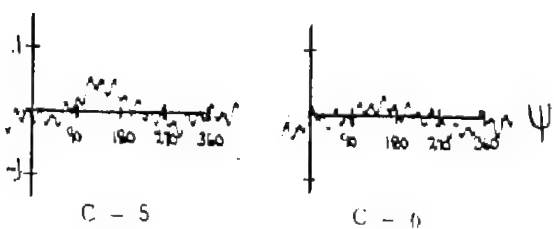
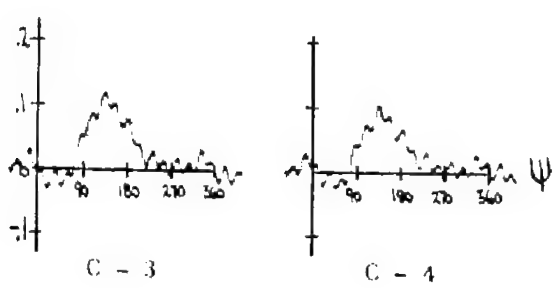
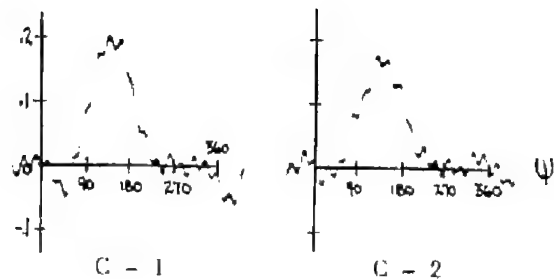
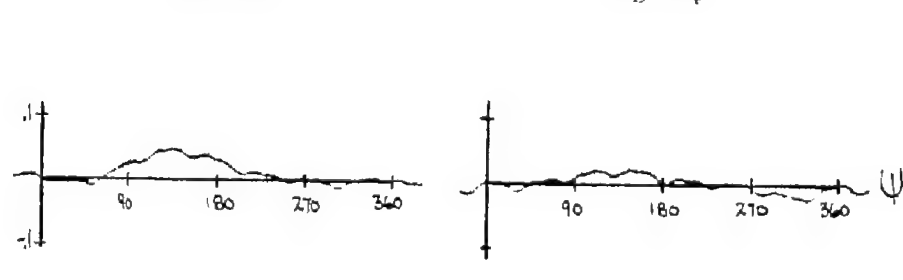
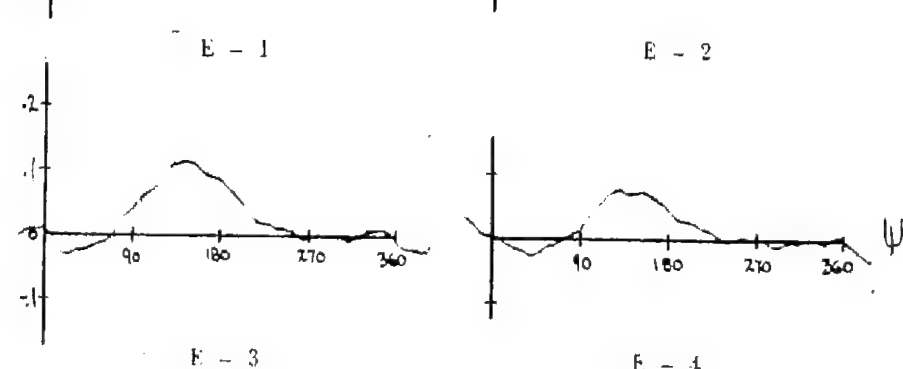
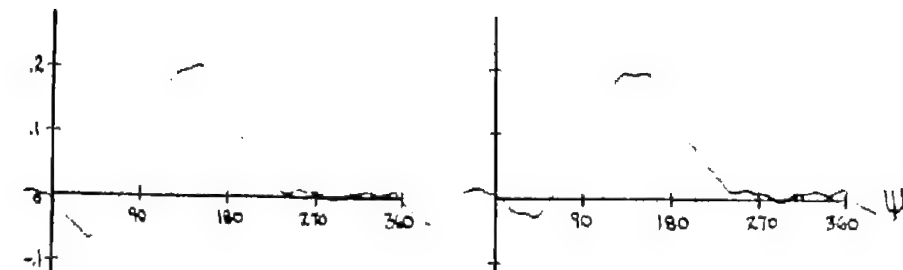
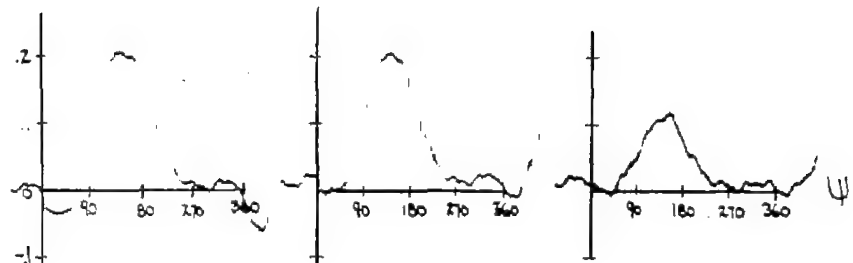
(c) Span station C;  $r/R = 0.590$ .(d) Span station E;  $r/R = 0.725$ .

Figure 25.- Continued.

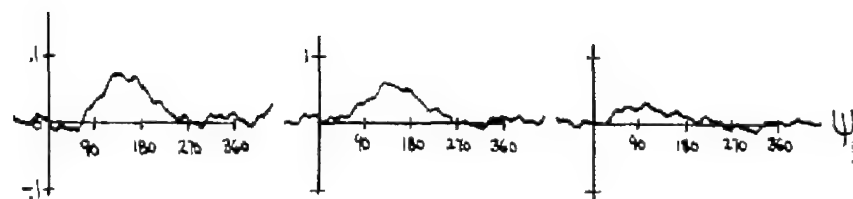




G - 1

G - 2

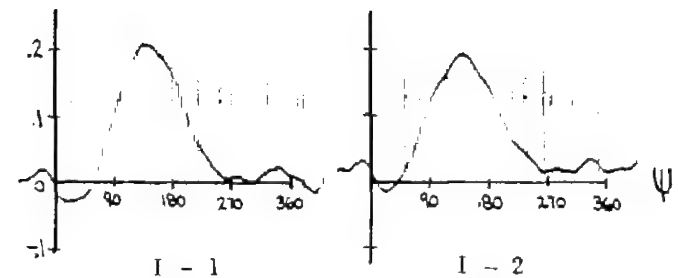
G - 3



G - 4

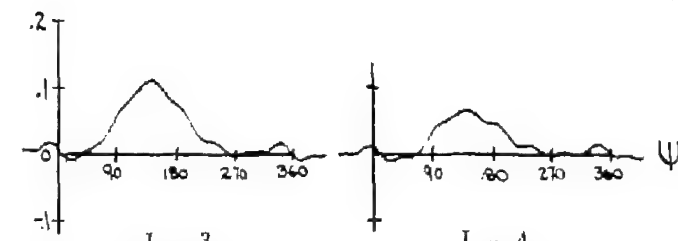
G - 5

G - 6

(e) Span station G;  $r/R = 0.825$ .

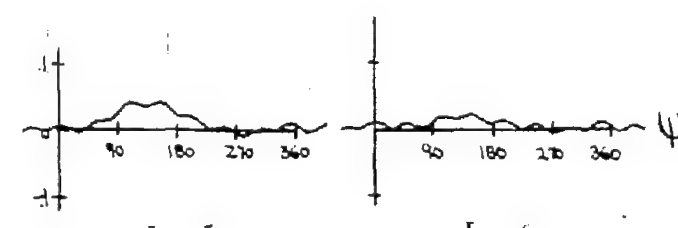
I - 1

I - 2



I - 3

I - 4

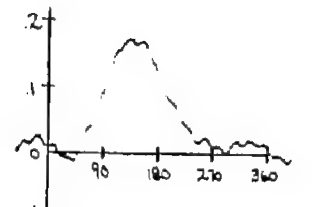


I - 5

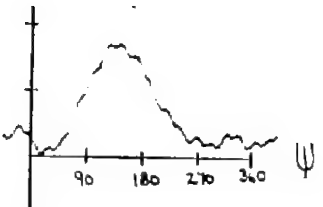
I - 6

(f) Span station I;  $r/R = 0.890$ .

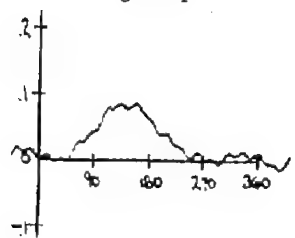
Figure 25.- Continued.



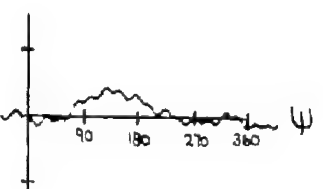
J - 1



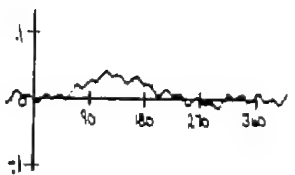
J - 2



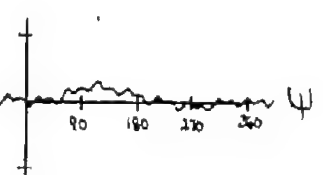
J - 3



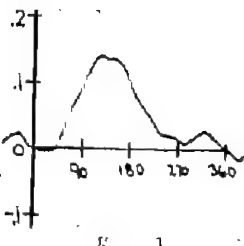
J - 4



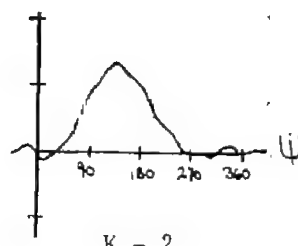
J - 5



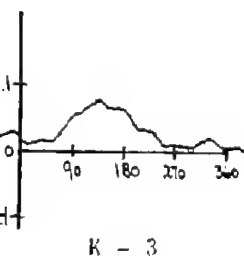
J - 6

(g) Span station J;  $r/R = 0.925$ 

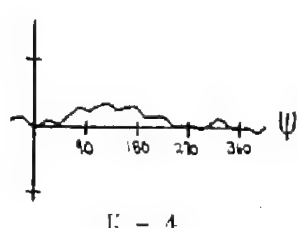
K - 1



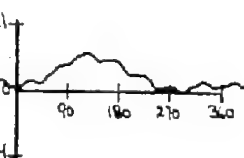
K - 2



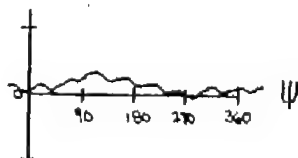
K - 3



K - 4



K - 5



K - 6

(h) Span station K;  $r/R = 0.960$ .

Figure 25.- Concluded.

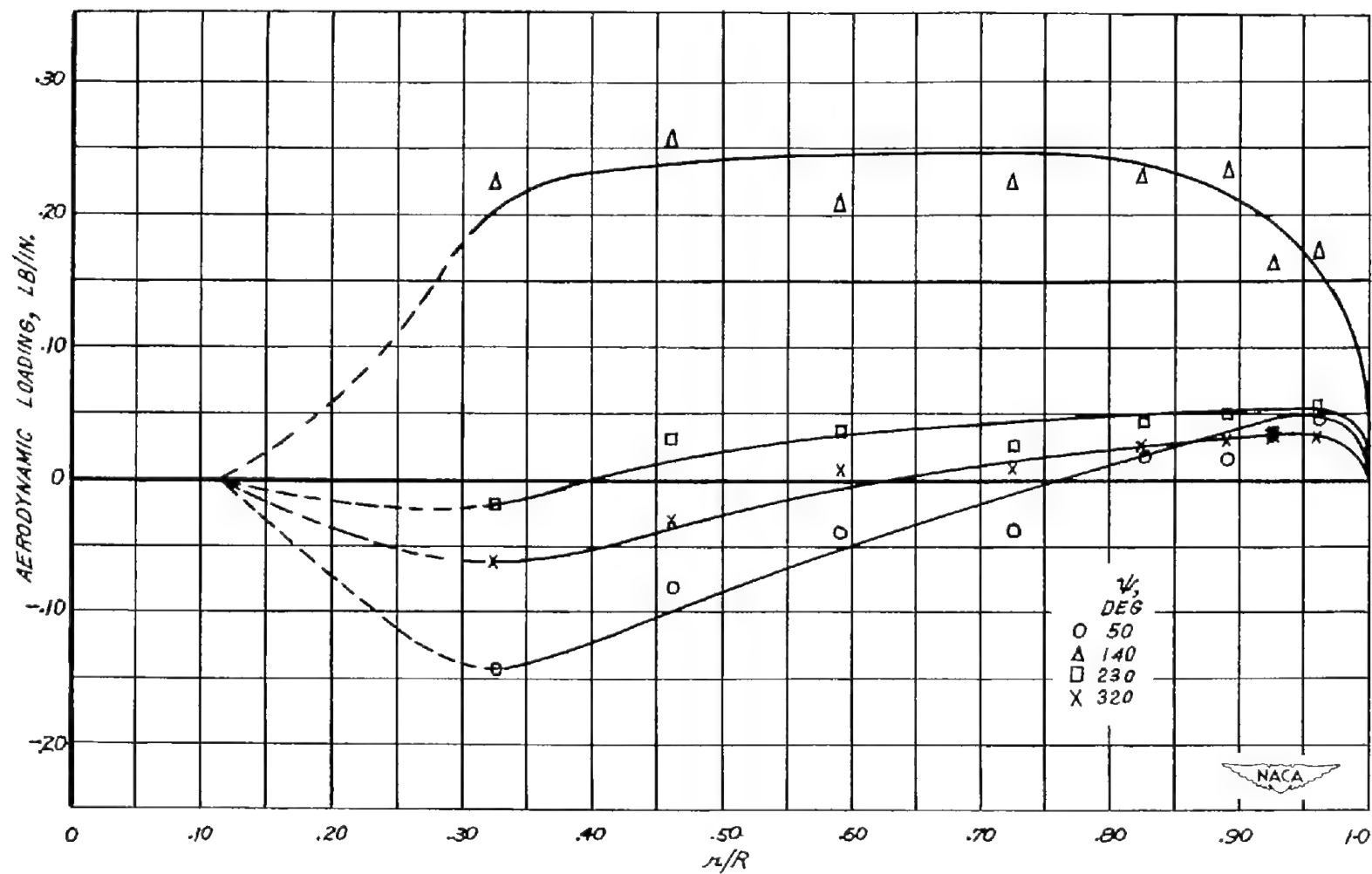


Figure 26.- Spanwise aerodynamic loading at various azimuth positions.

Profile, NACA 0015; speed, 500 rpm;  $\xi = 0.13$ ;  $\mu = 1.0$ ;  $\theta = 4^\circ$ ;  
 $\alpha = -5^\circ$ ;  $C_T/\sigma = 0.019$ .

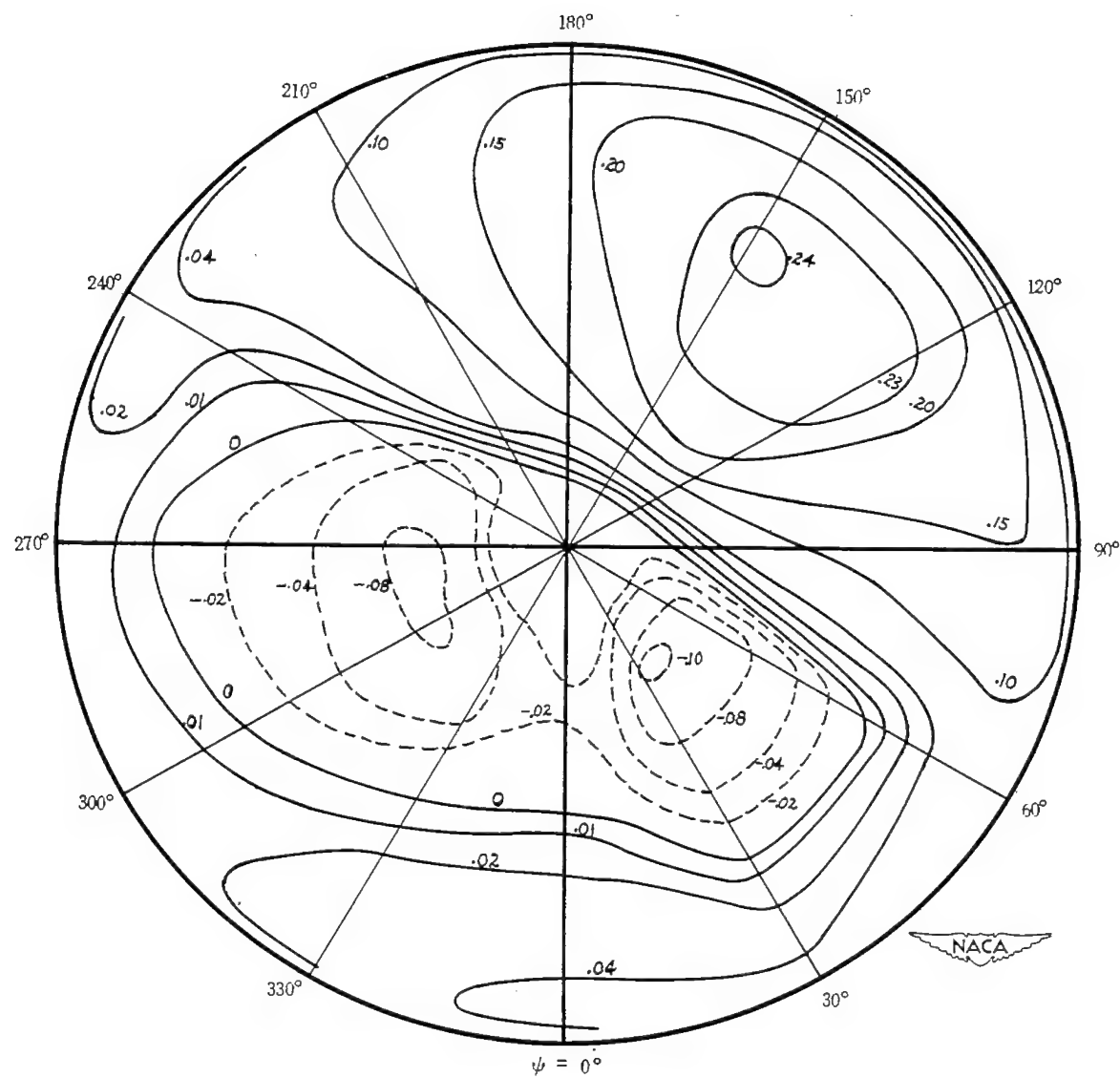
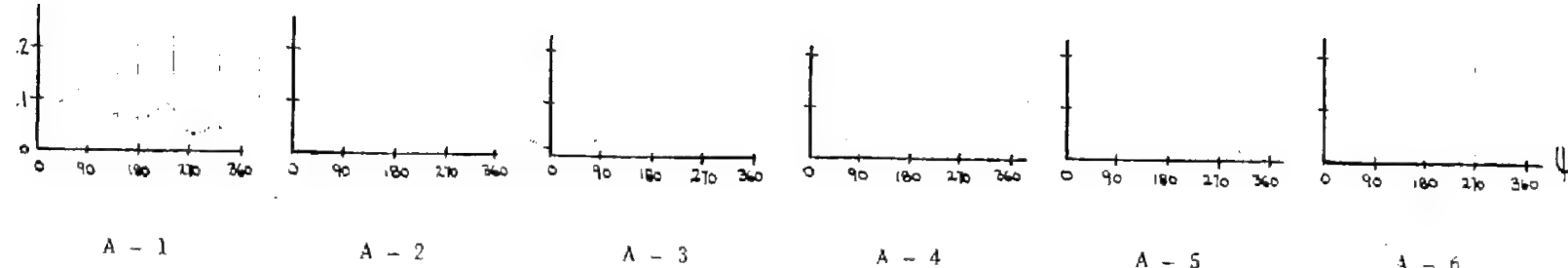
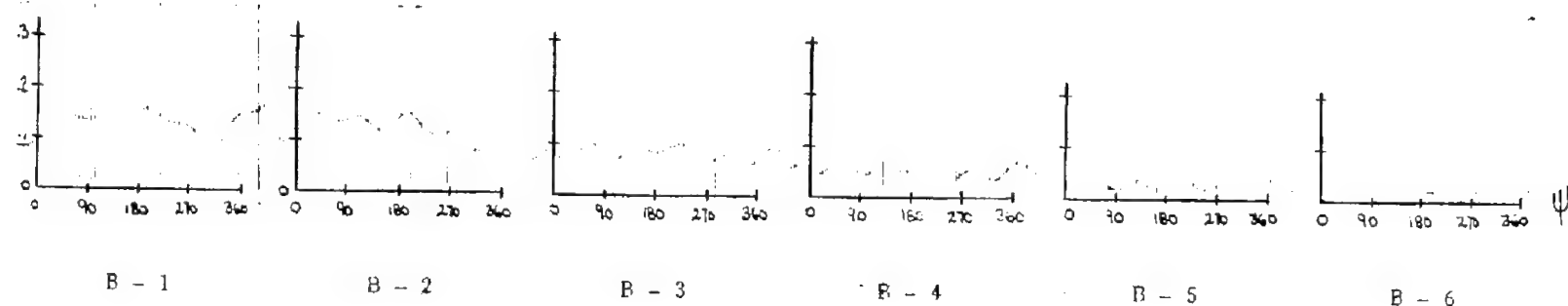


Figure 27.- Curves of constant aerodynamic loading in pounds per inch.  
 Profile, NACA 0015; speed, 500 rpm;  $\xi = 0.13$ ;  $\mu = 1.0$ ;  $\theta = 4^\circ$ ;  
 $\alpha = -5^\circ$ ;  $C_T/\sigma = 0.019$ .



(a) Span station A;  $r/R = 0.325$ .



(b) Span station B;  $r/R = 0.460$ .



Figure 28.- Pressure difference in pounds per square inch against azimuth in degrees. Profile, NACA 0015; speed, 800 rpm;  $\xi = 0$ ;  $\mu = 0.22$ ;  $\theta = 8^\circ$ ;  $\alpha = -5^\circ$ .

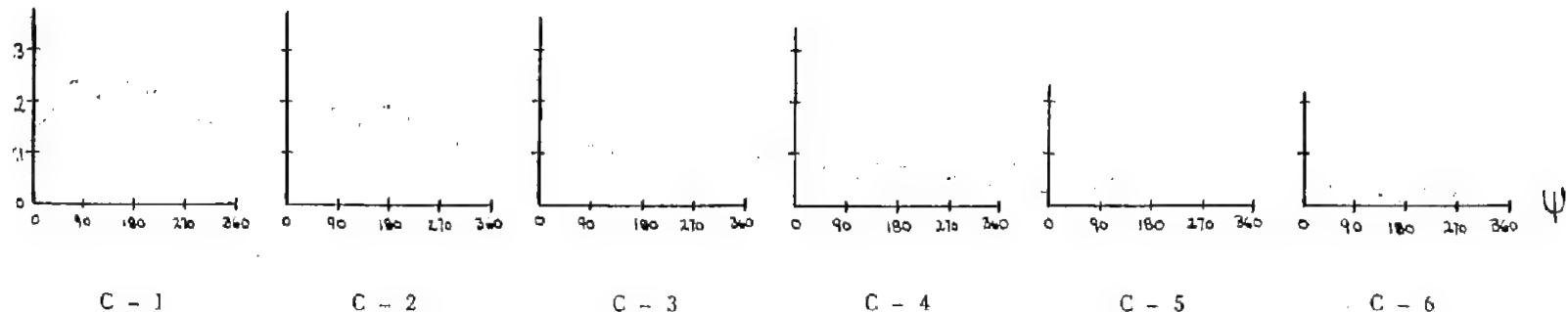
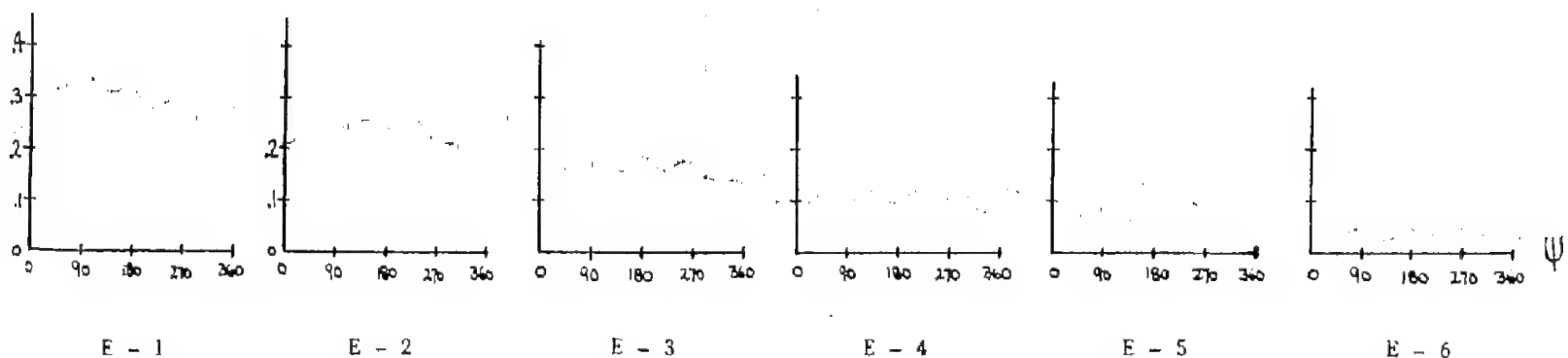
(c) Span station C;  $r/R = 0.590$ .(d) Span station E;  $r/R = 0.725$ .

Figure 28.- Continued.

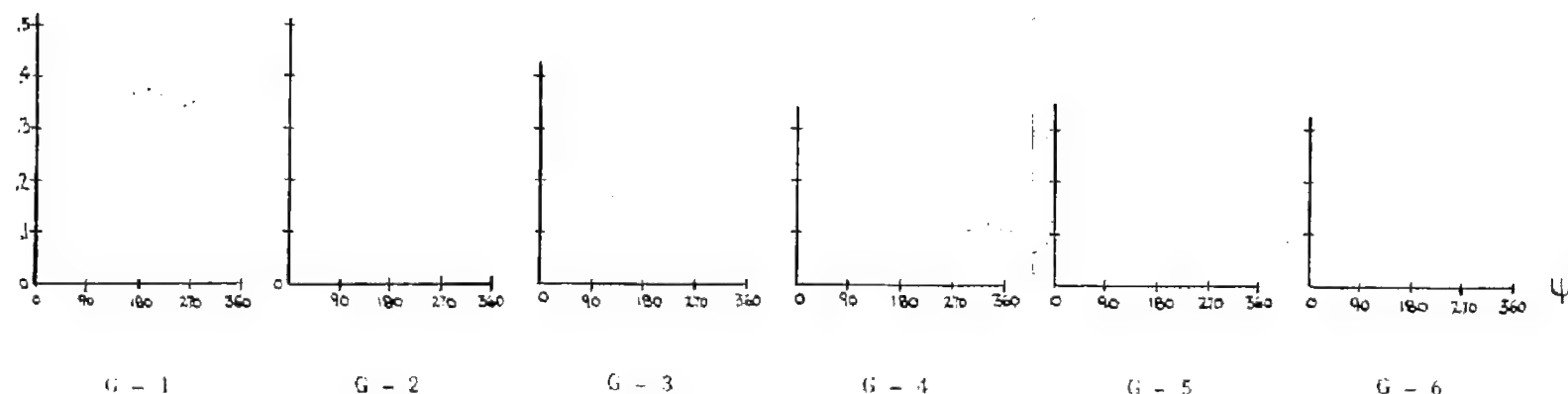
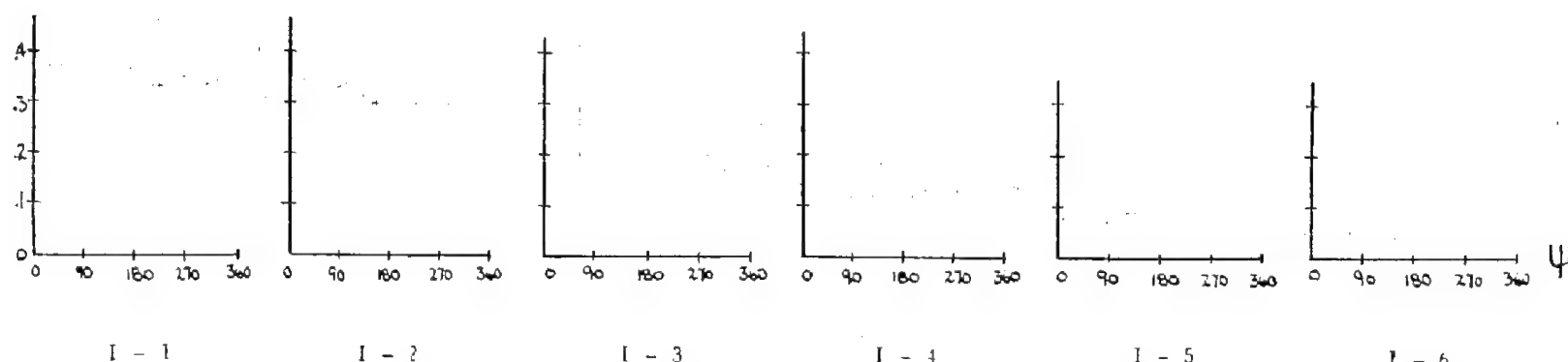
(e) Span station G;  $r/R = 0.825$ .(f) Span station I;  $r/R = 0.890$ .

Figure 28.- Continued.

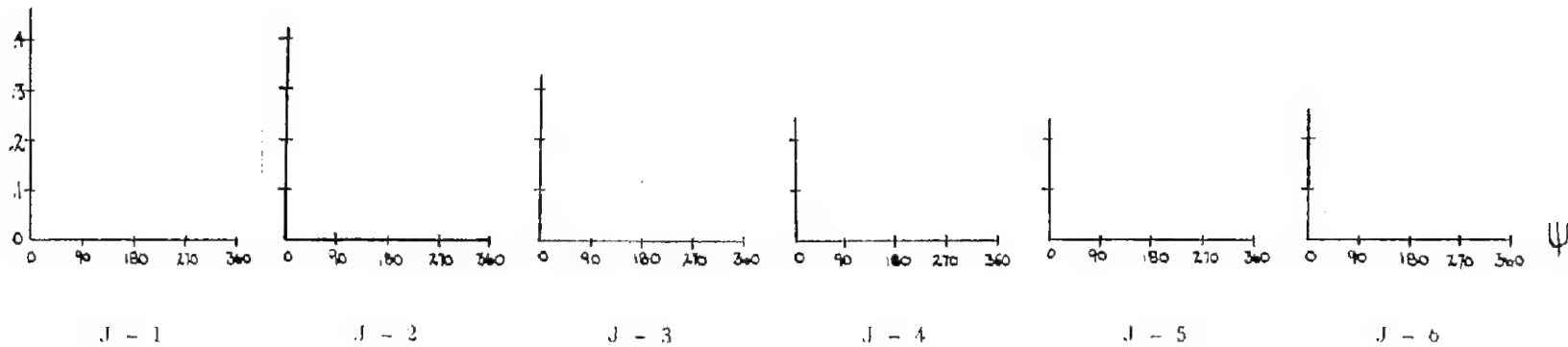
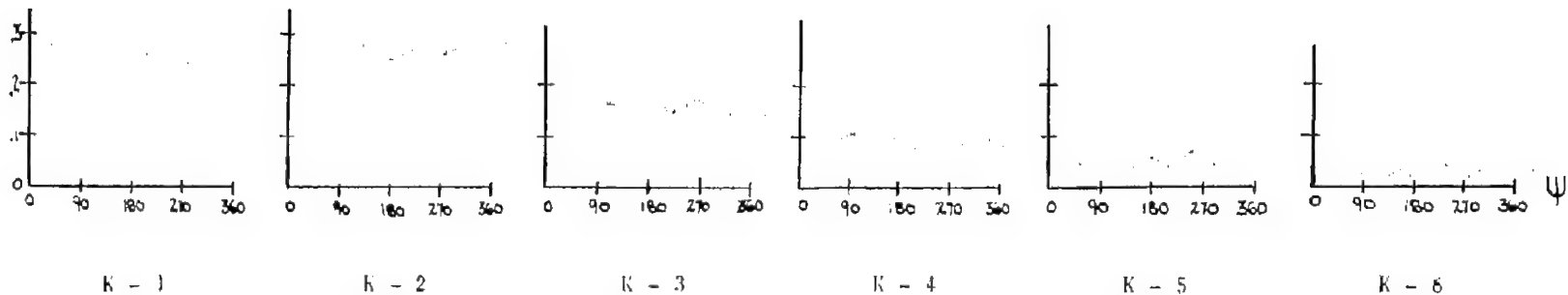
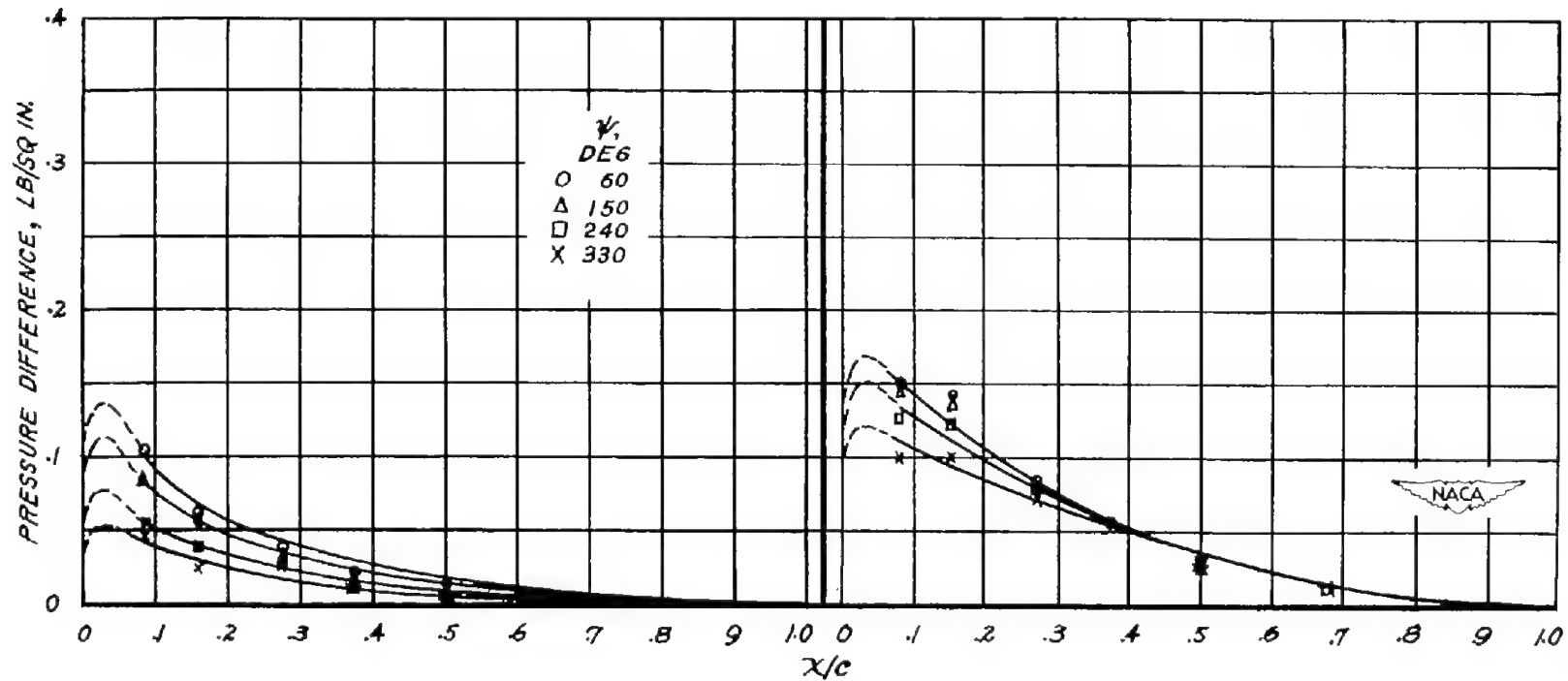
(g) Span station J;  $r/R = 0.925$ .(h) Span station K;  $r/R = 0.960$ .

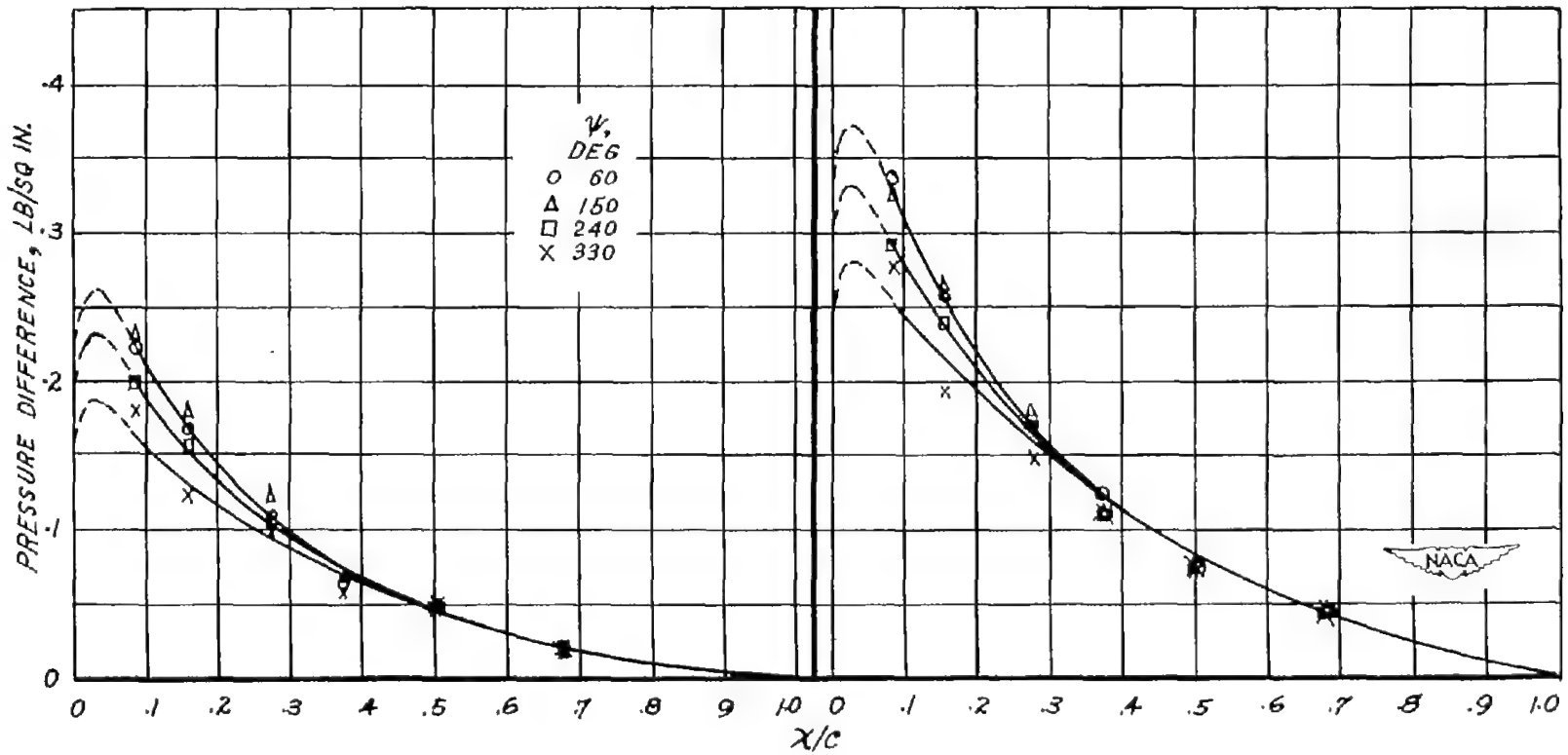
Figure 28.- Concluded.





(a) Span station A;  $r/R = 0.325$ . (b) Span station B;  $r/R = 0.460$ .

Figure 29.- Chordwise pressure distribution on hinged rotor blade at various azimuth positions. Profile, NACA 0015; speed, 800 rpm;  $\xi = 0$ ;  $\mu = 0.22$ ;  $\theta = 8^\circ$ ;  $\alpha = -5^\circ$ .



(c) Span station C;  $r/R = 0.590$ . (d) Span station E;  $r/R = 0.725$ .

Figure 29.- Continued.

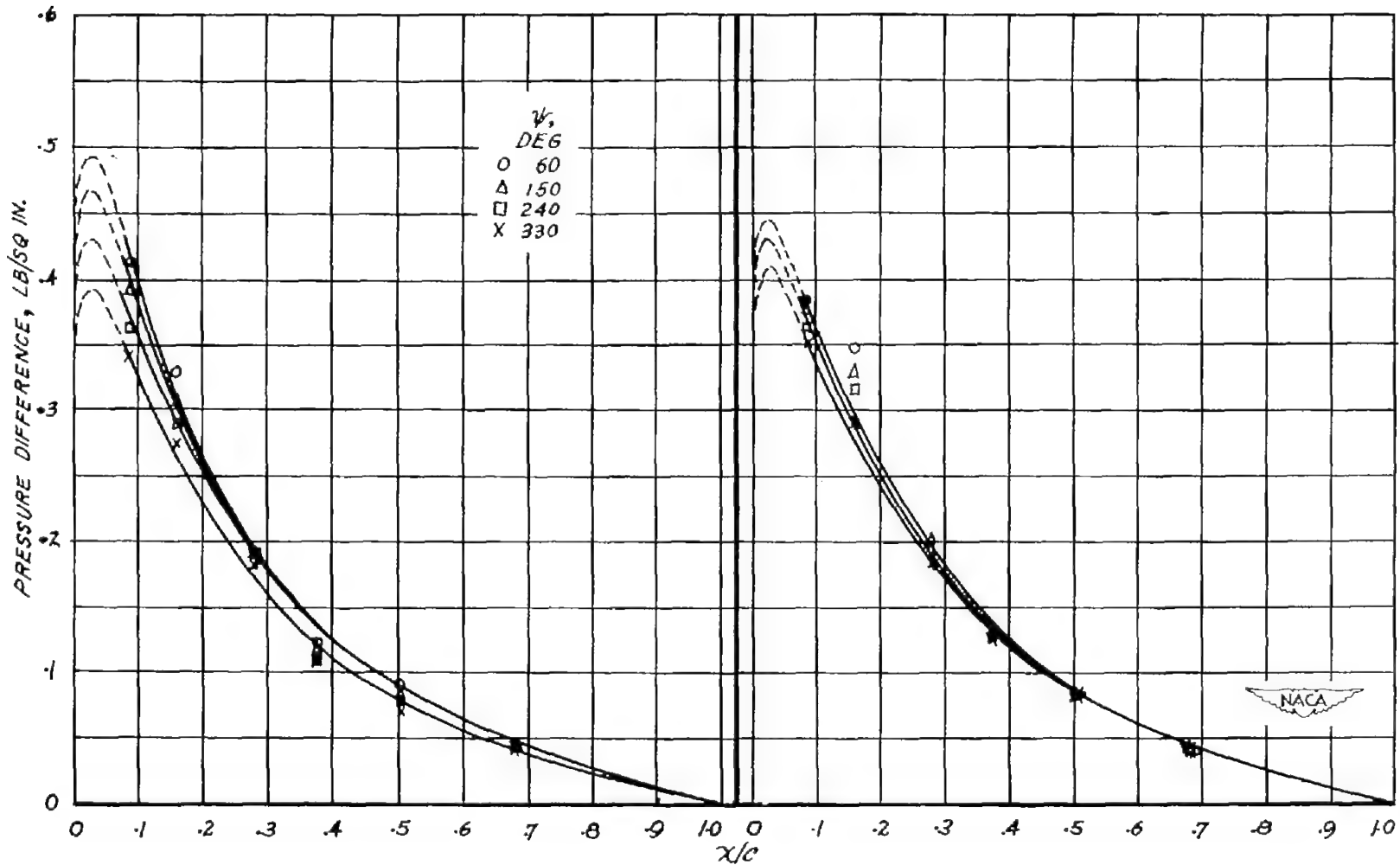
(e) Span station G;  $r/R = 0.825$ . (f) Span station I;  $r/R = 0.890$ .

Figure 29.- Continued.

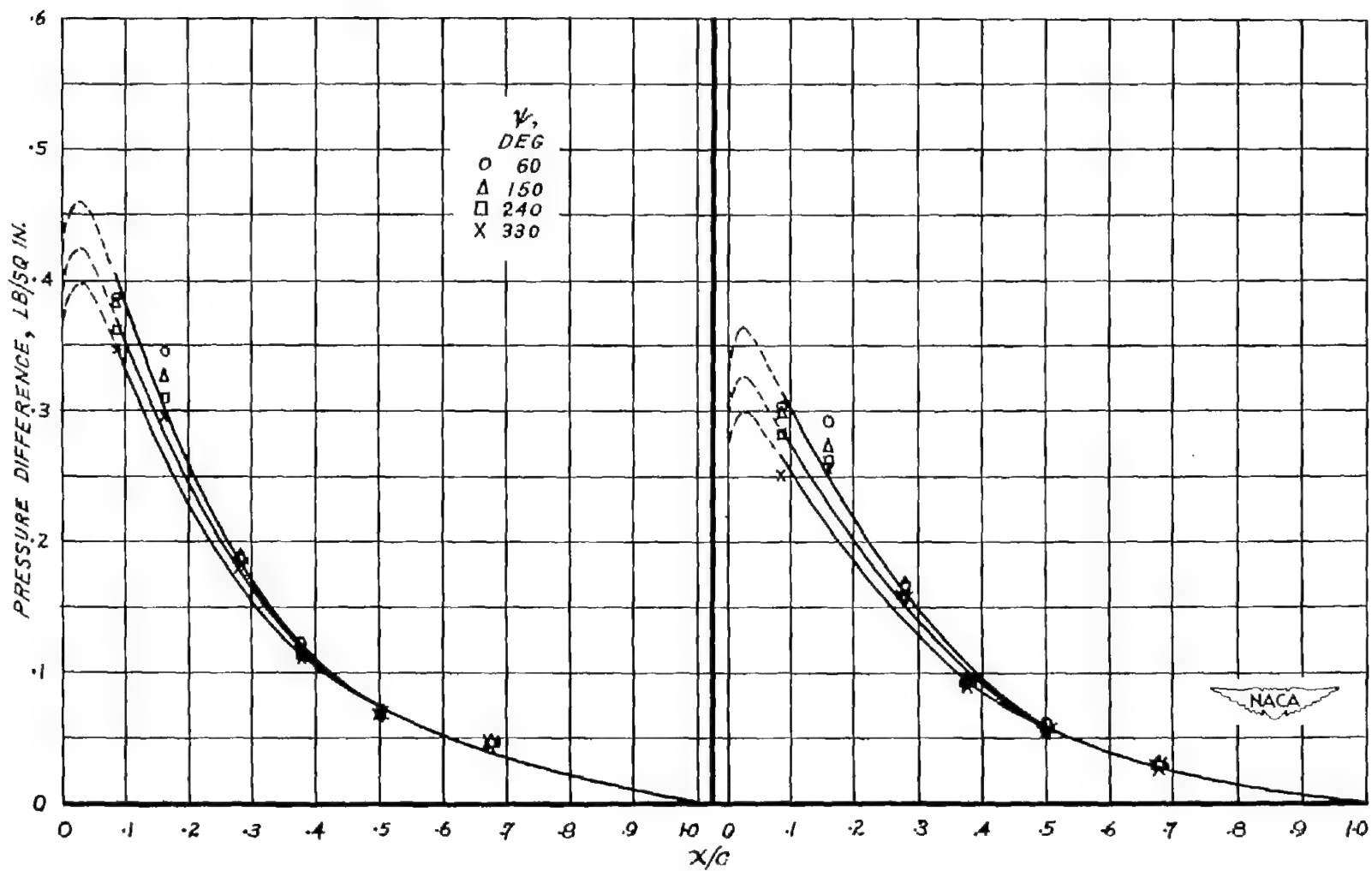
(g) Span station J;  $r/R = 0.925$ . (h) Span station K;  $r/R = 0.960$ .

Figure 29.- Concluded.

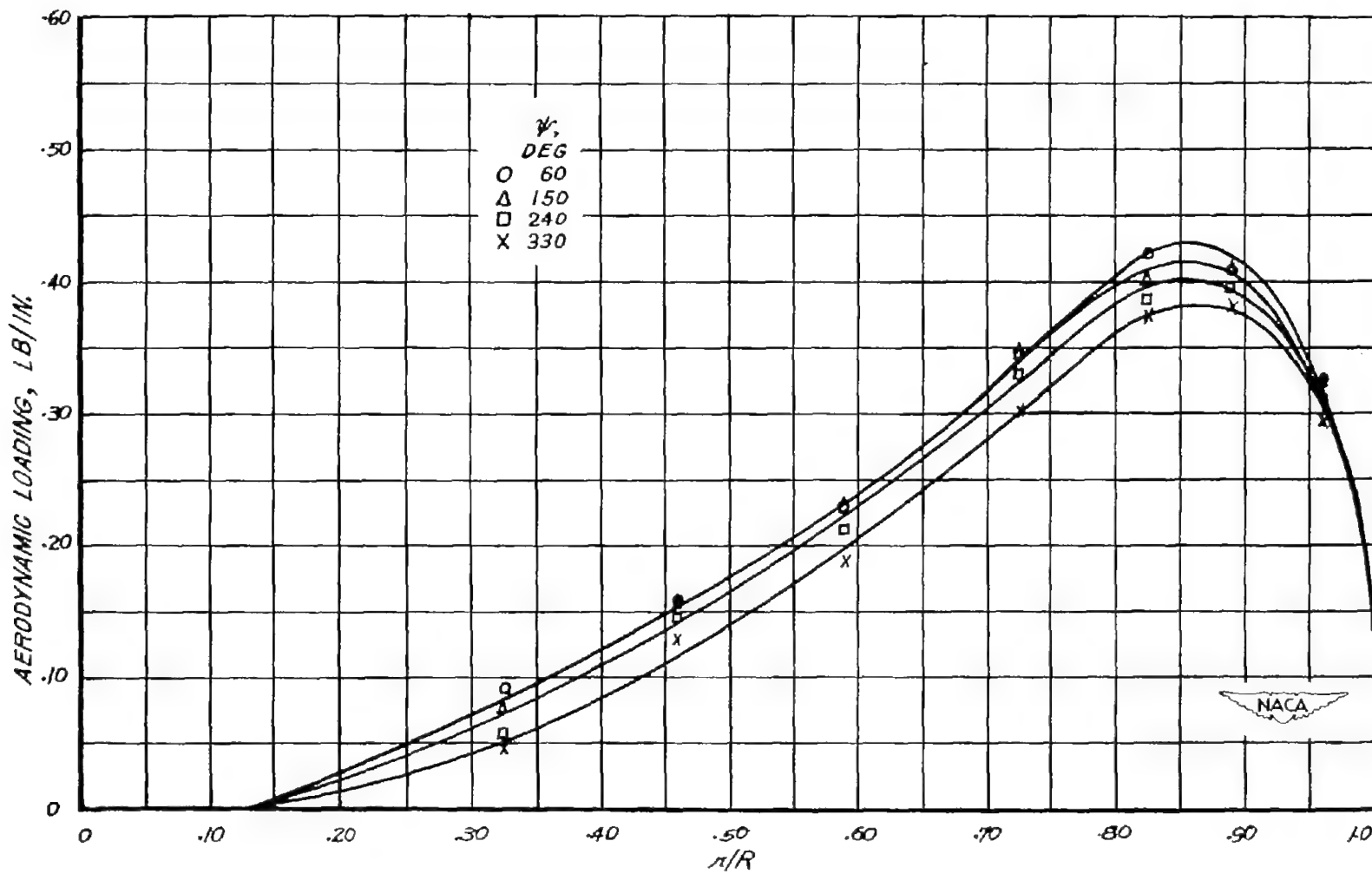


Figure 30.- Spanwise aerodynamic loading at various azimuth positions.  
 Profile, NACA 0015; speed, 800 rpm;  $\xi = 0$ ;  $\mu = 0.22$ ;  $\theta = 8^\circ$ ;  $\alpha = -5^\circ$ ;  
 $C_T/\sigma = 0.083$ .

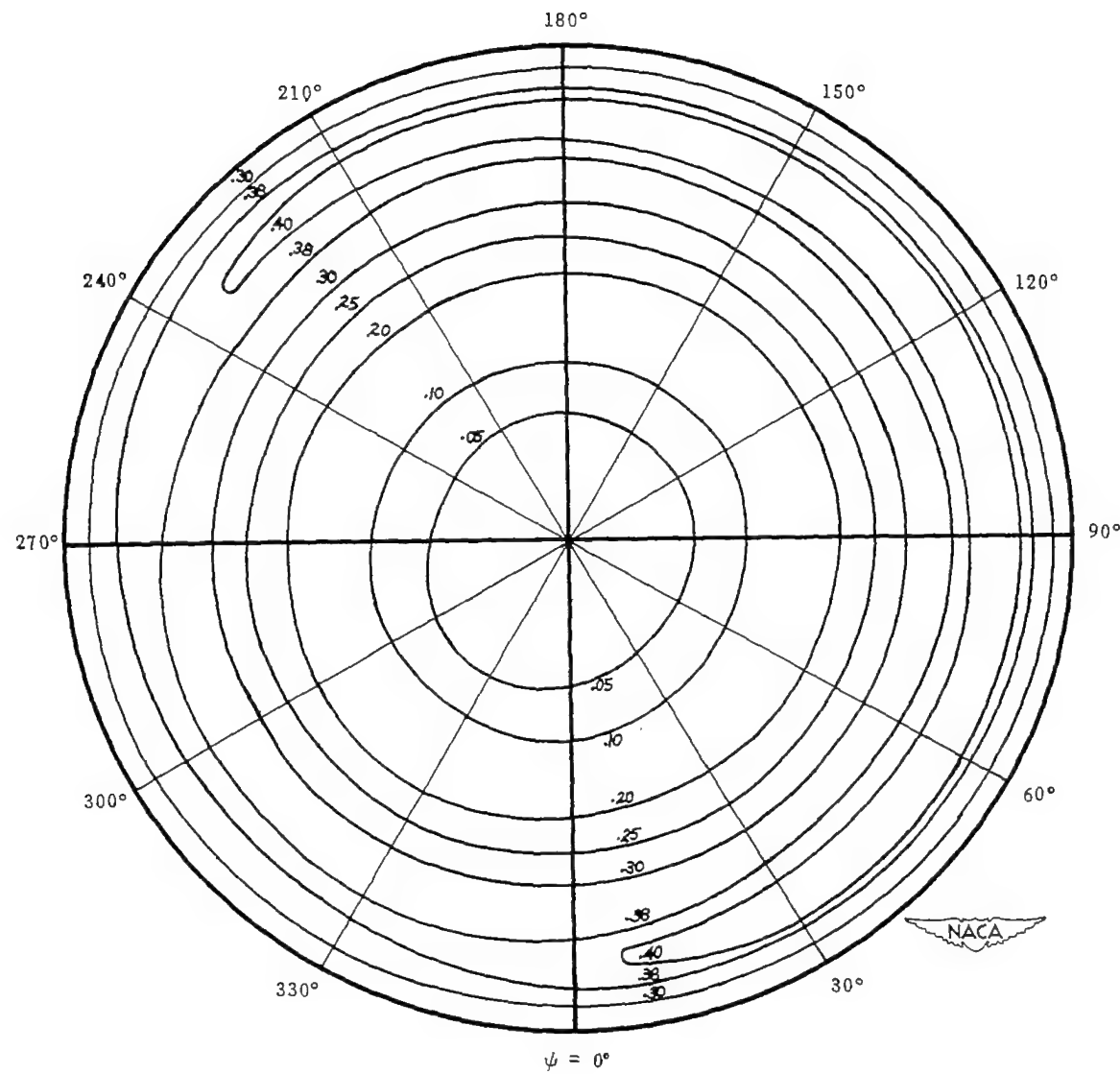


Figure 31.- Curves of constant aerodynamic loading in pounds per inch.  
 Profile, NACA 0015; speed, 800 rpm;  $\xi = 0$ ;  $\mu = 0.22$ ;  $\theta = 8^\circ$ ;  $\alpha = -5^\circ$ ;  
 $C_T/\sigma = 0.083$ .

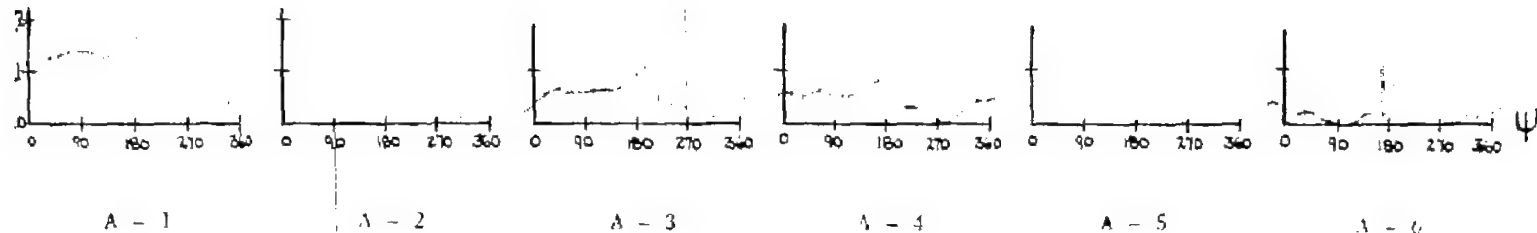
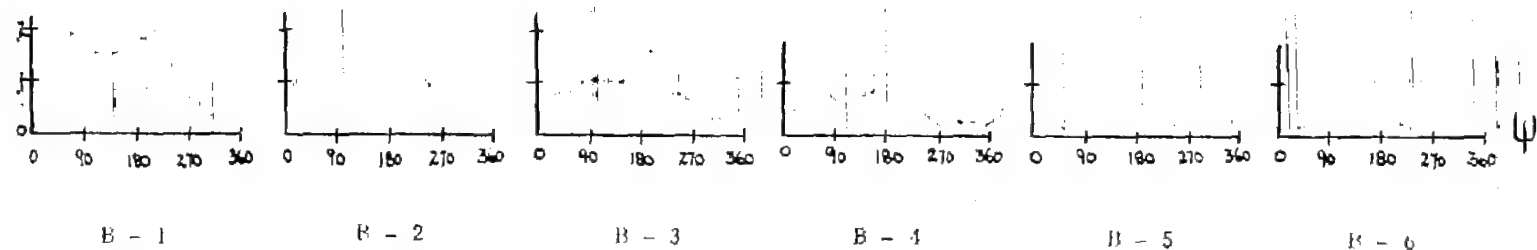
(a) Span station A;  $r/R = 0.325$ .(b) Span station B;  $r/R = 0.460$ .

Figure 32.- Pressure difference in pounds per square inch against azimuth in degrees. Profile, NACA 0015; speed, 800 rpm;  $\xi = 0$ ;  $\mu = 0.50$ ;  $\theta = 8^\circ$ ;  $\alpha = -5^\circ$ .

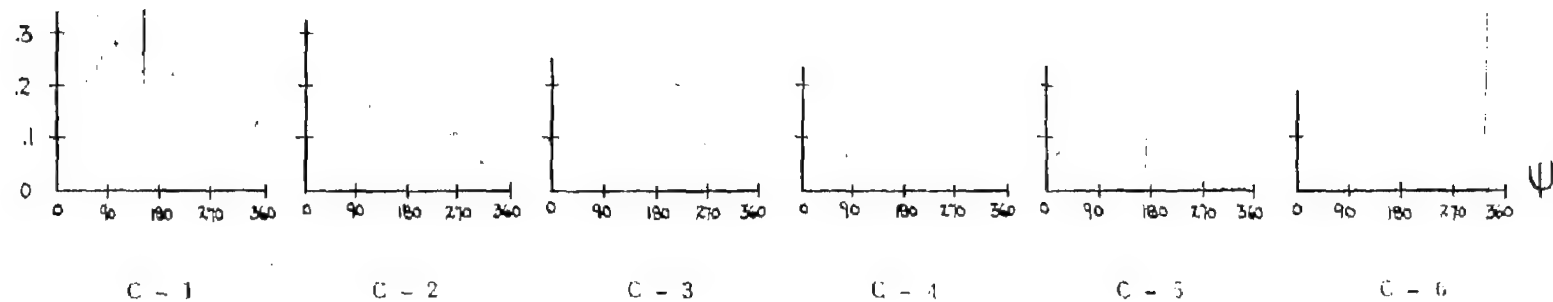
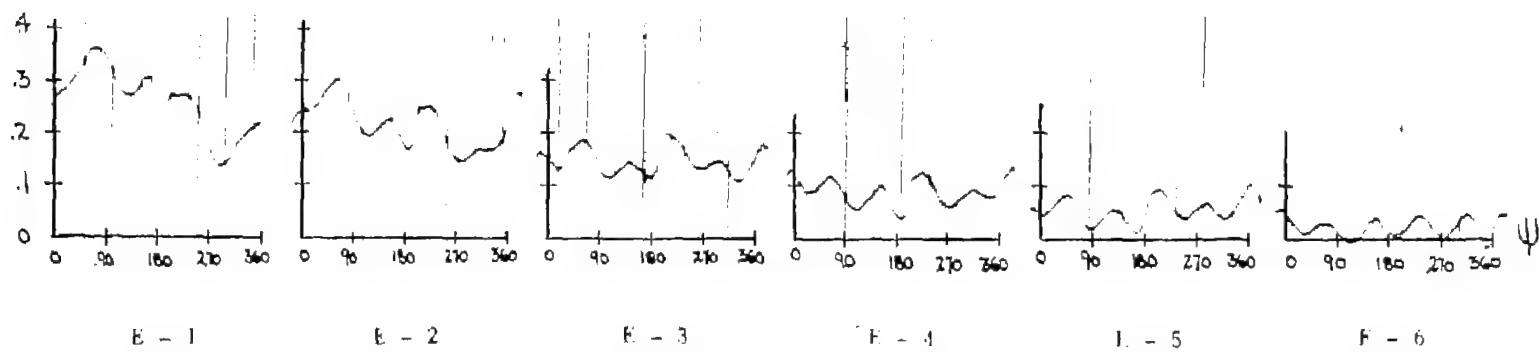
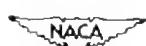
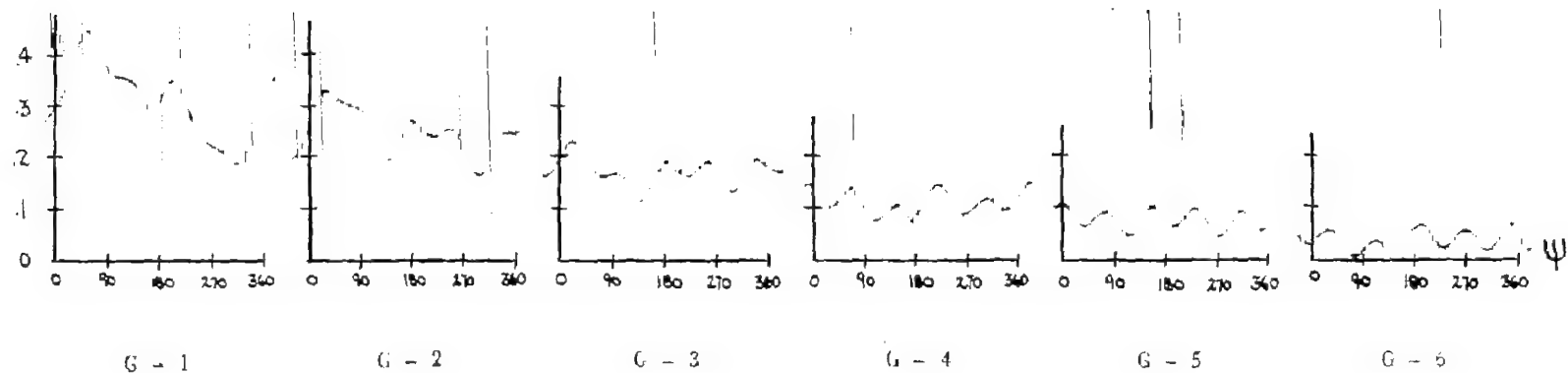
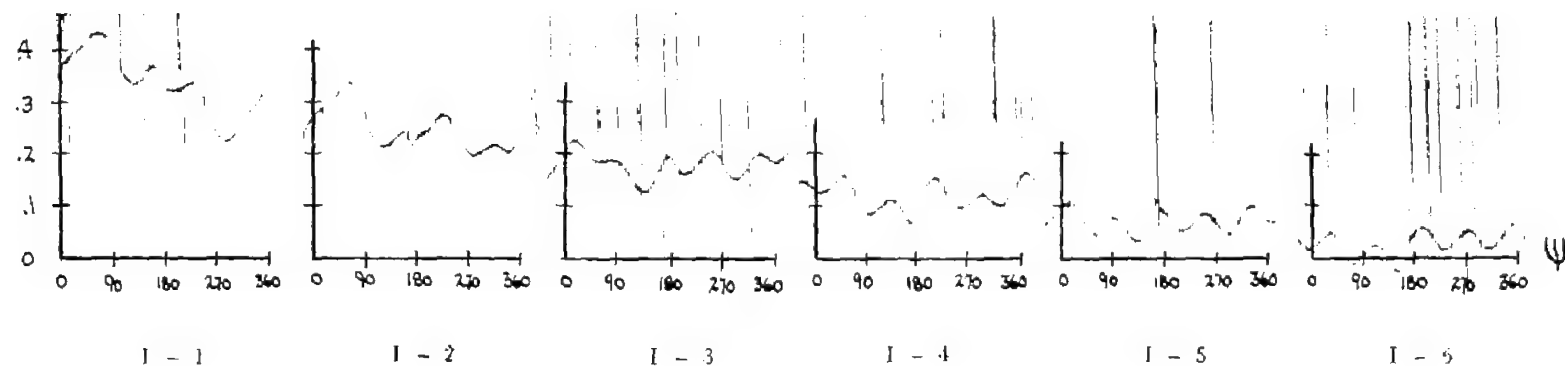
(c) Span station C;  $r/R = 0.590$ .(d) Span station E;  $r/R = 0.725$ .

Figure 32.- Continued.





(e) Span station G;  $r/R = 0.825$ .



(f) Span station I;  $r/R = 0.890$ .

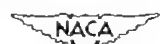


Figure 32.- Continued.

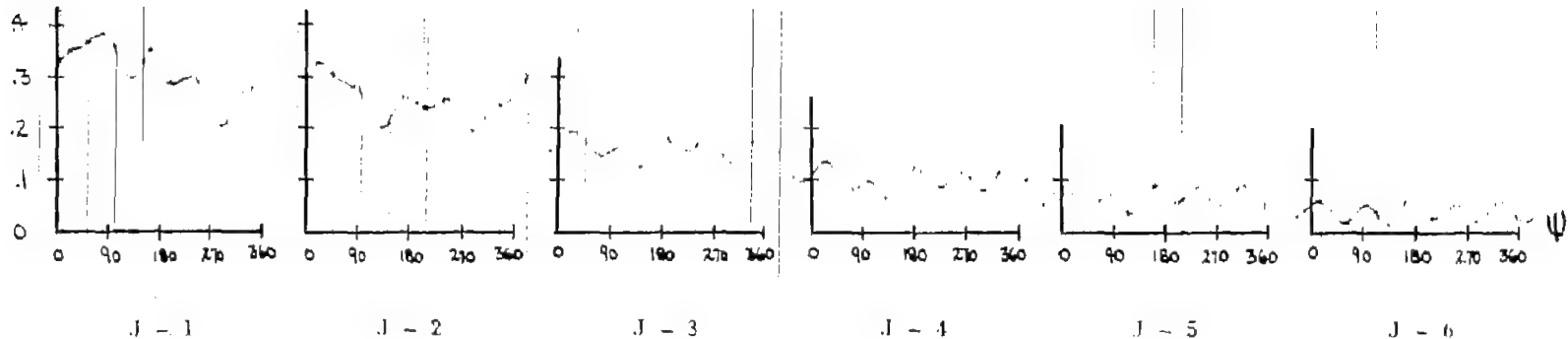
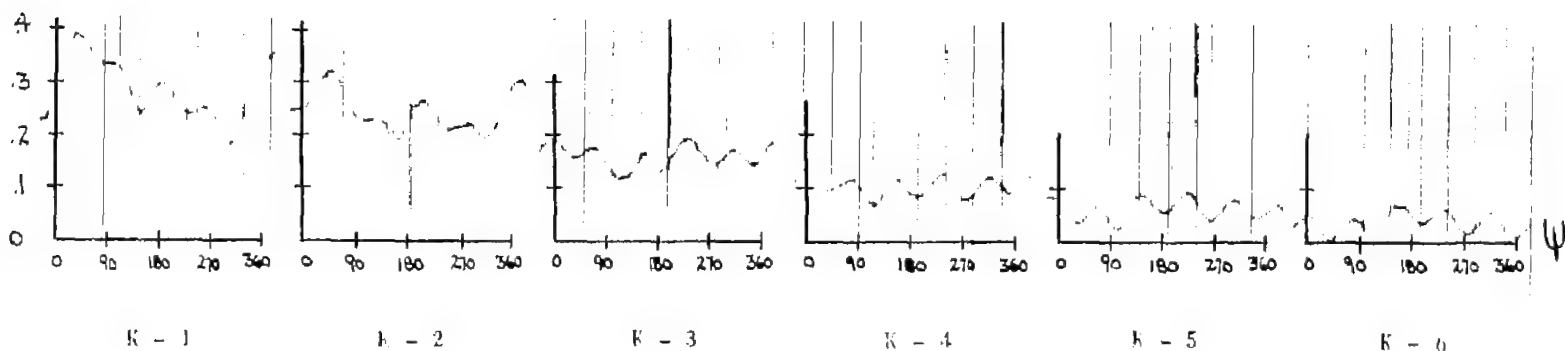
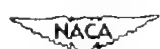
(g) Span station J;  $r/R = 0.925$ .(h) Span station K;  $r/R = 0.960$ .

Figure 32.- Concluded.

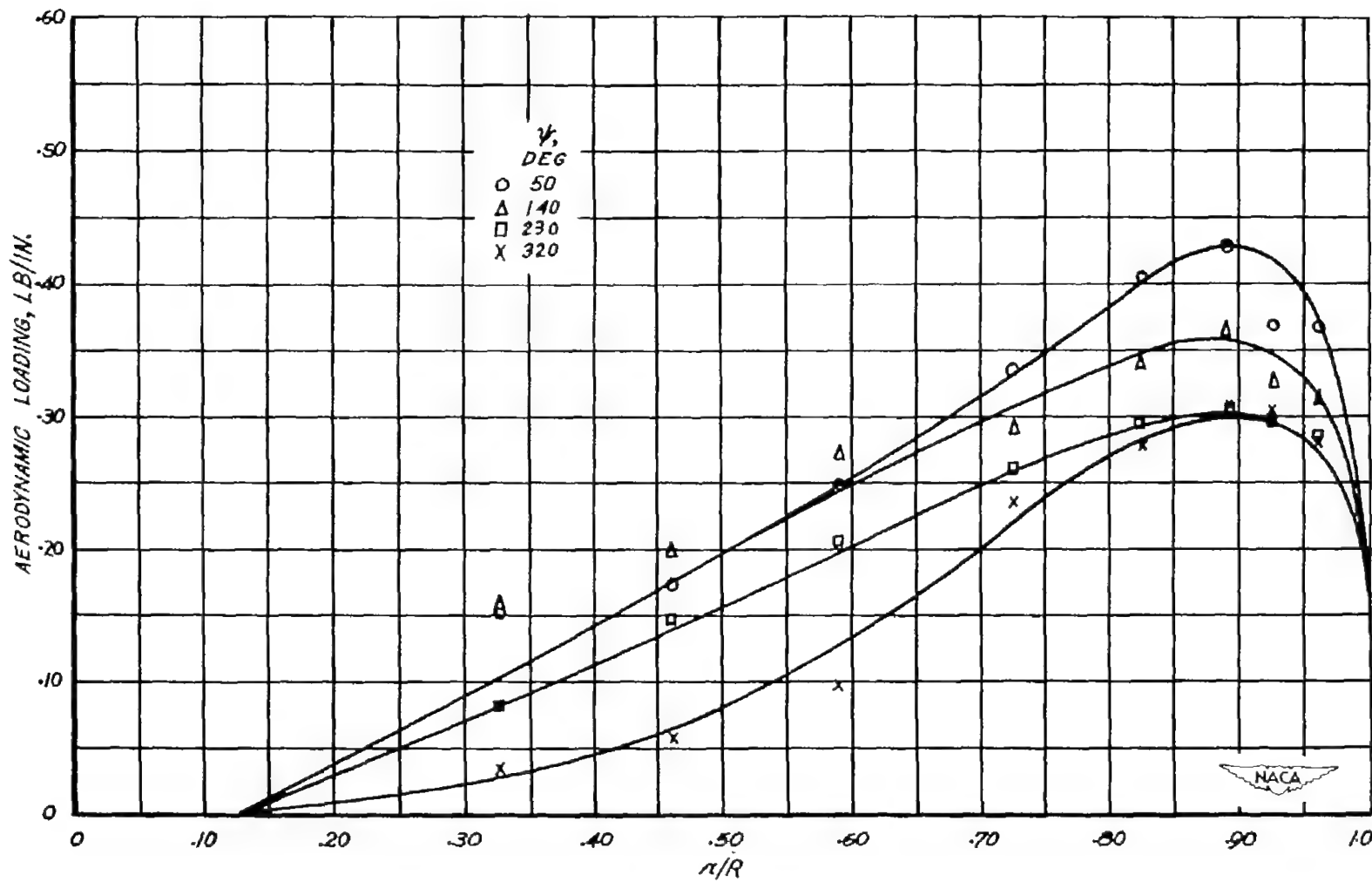


Figure 33.- Spanwise aerodynamic loading at various azimuth positions.  
 Profile, NACA 0015; speed, 800 rpm;  $\xi = 0$ ;  $\mu = 0.50$ ;  $\theta = 8^\circ$ ;  $\alpha = -5^\circ$ ;  
 $C_T/\sigma = 0.076$ .

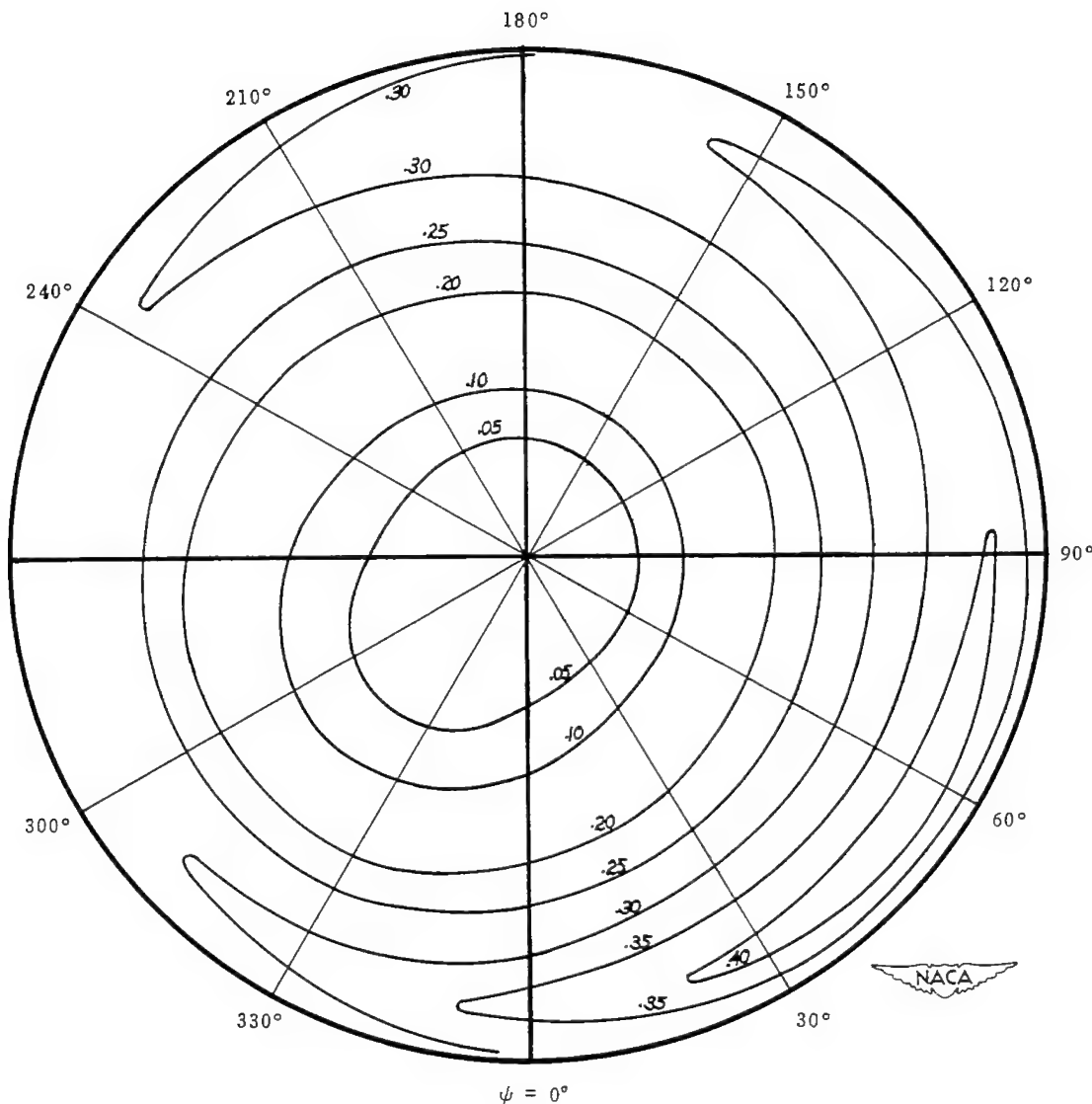


Figure 34.- Curves of constant aerodynamic loading in pounds per inch.  
 Profile, NACA 0015; speed, 800 rpm;  $\xi = 0$ ;  $\mu = 0.50$ ;  $\theta = 8^\circ$ ;  $\alpha = -5^\circ$ ;  
 $C_T/\sigma = 0.076$ .

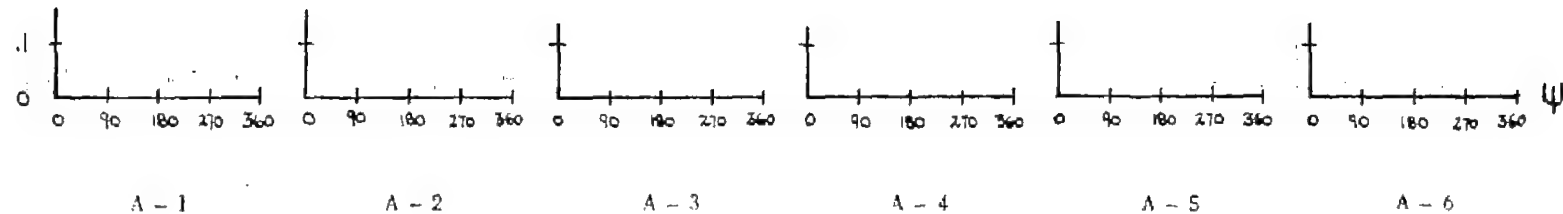
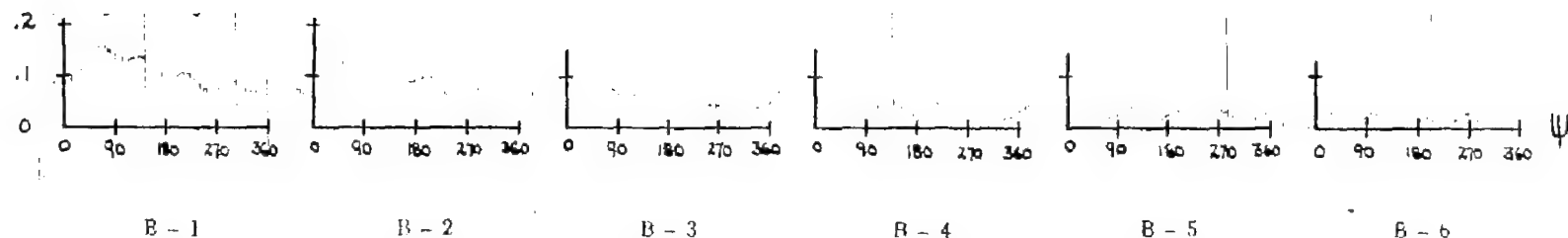
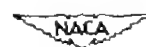
(a) Span station A;  $r/R = 0.325$ .(b) Span station B;  $r/R = 0.460$ .

Figure 35.- Pressure difference in pounds per square inch against azimuth in degrees. Profile, NACA 0015; speed, 800 rpm;  $\xi = 0$ ;  $\mu = 0.10$ ;  $\theta = 8^\circ$ ;  $\alpha = -5^\circ$ .

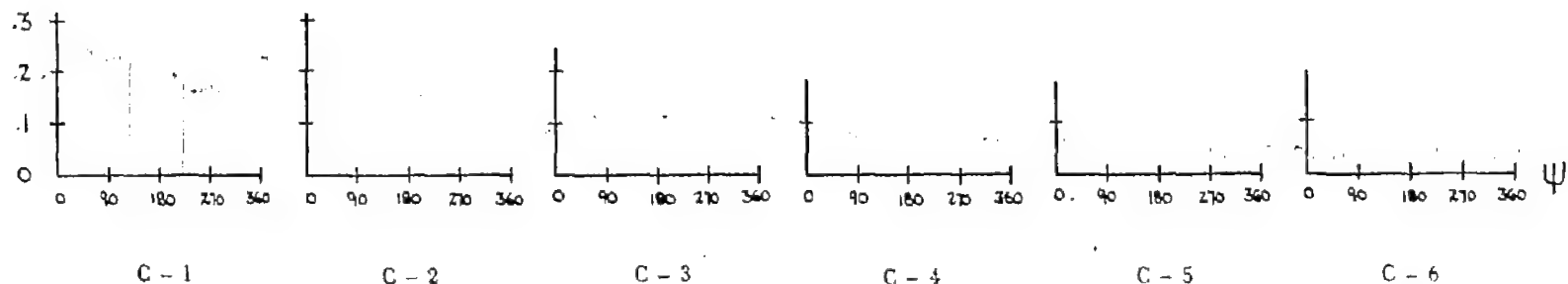
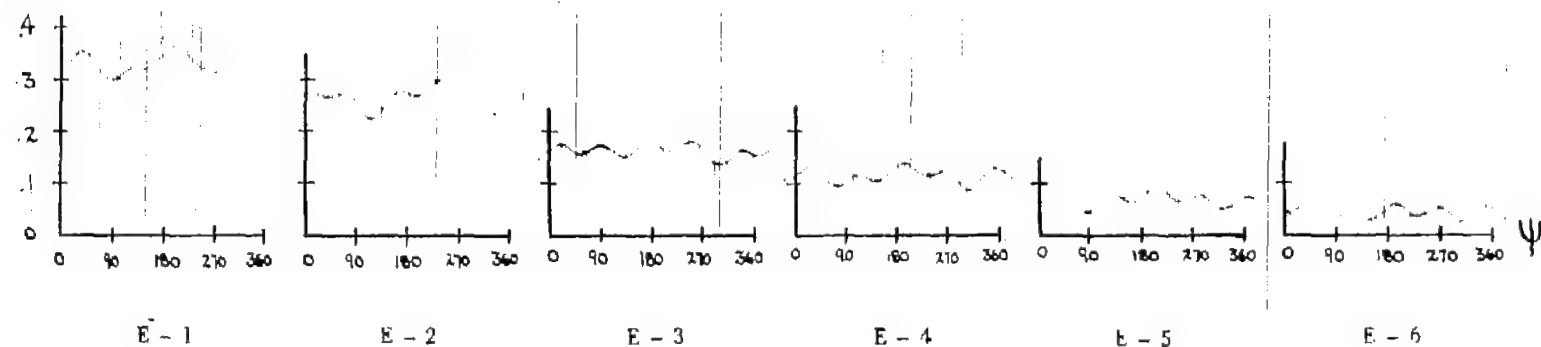
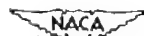
(c) Span station C;  $r/R = 0.590$ .(d) Span station E;  $r/R = 0.725$ .

Figure 35.- Continued.

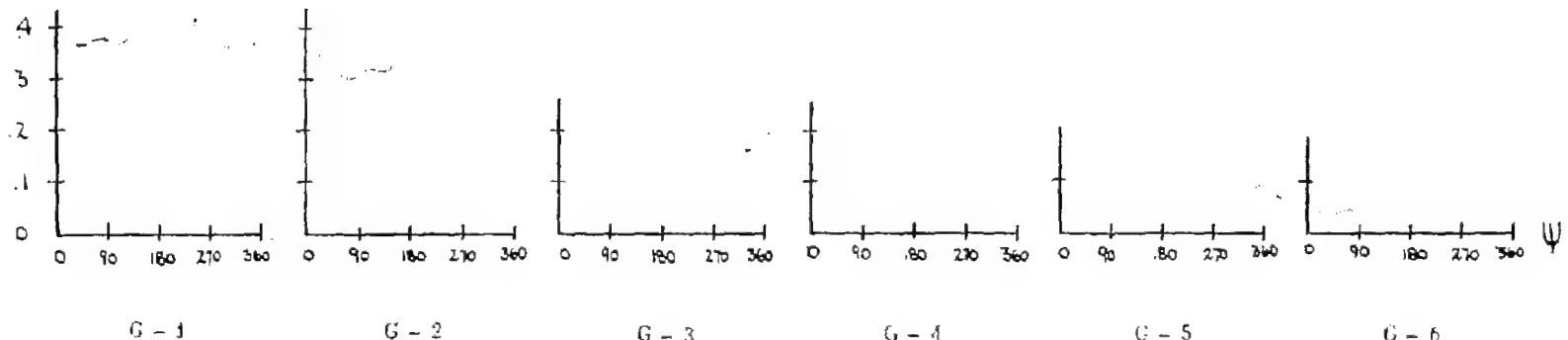
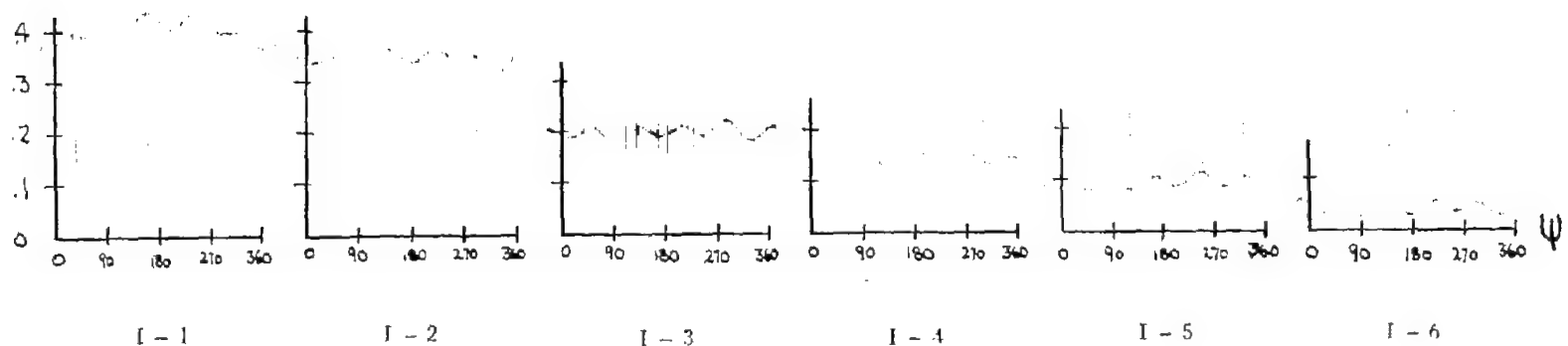
(e) Span station G;  $r/R = 0.825$ .(f) Span station I;  $r/R = 0.890$ .

Figure 35.- Continued.

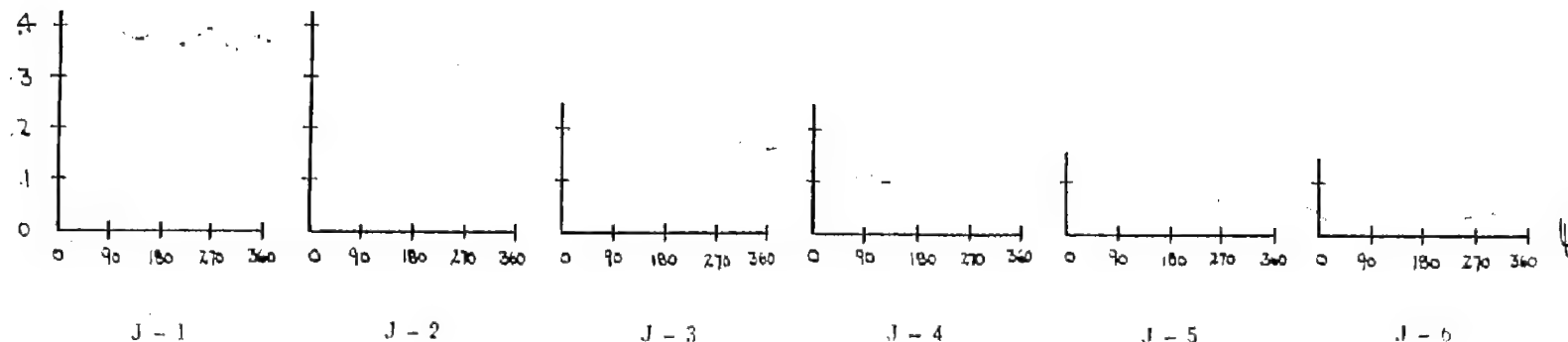
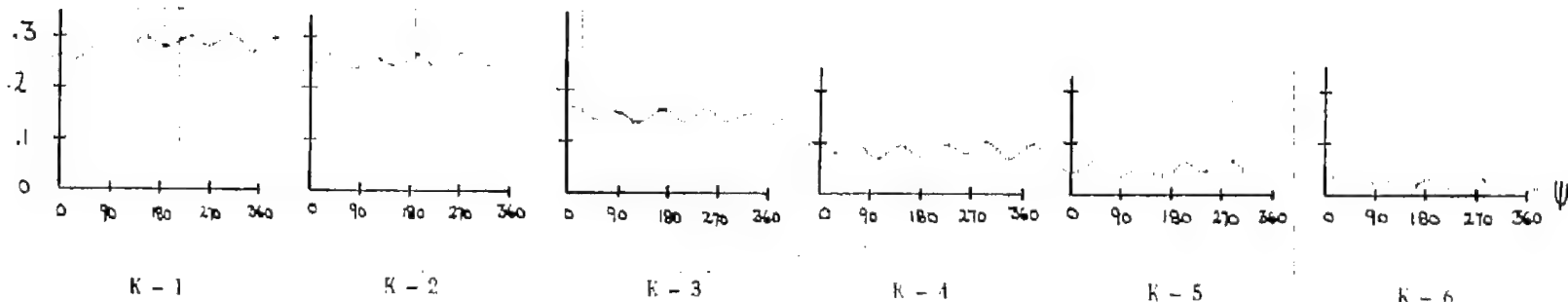
(g) Span station  $J$ ;  $r/R = 0.925$ .(h) Span station  $K$ ;  $r/R = 0.960$ .

Figure 35.- Concluded.

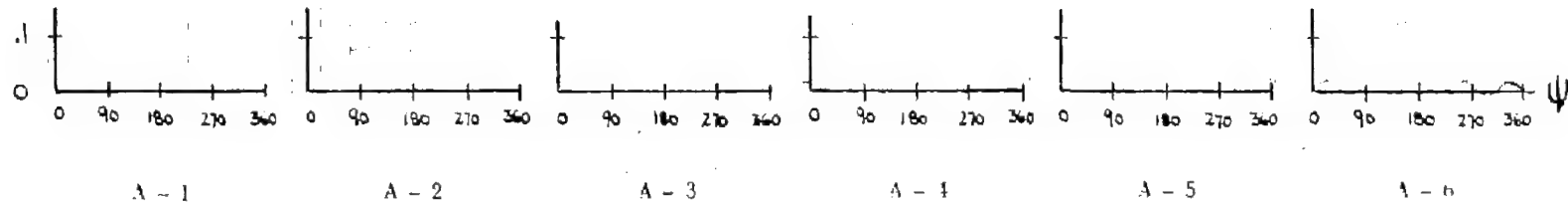
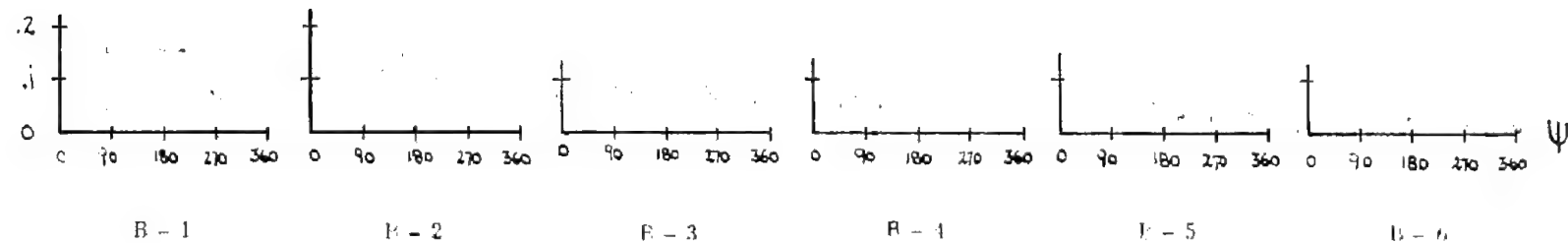
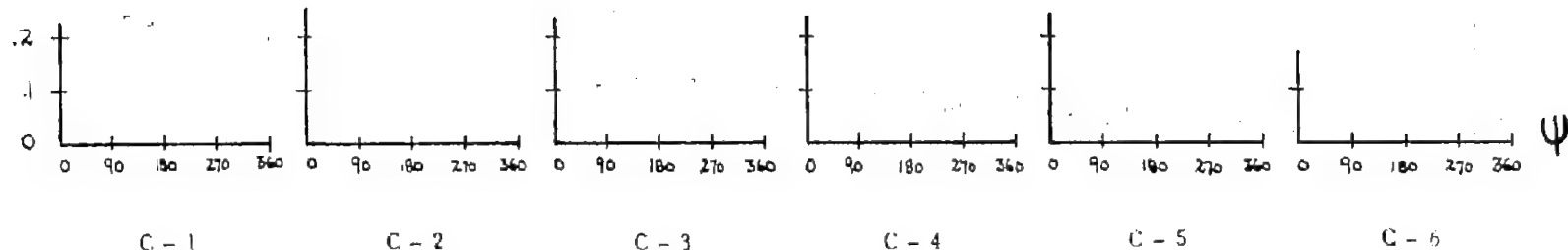
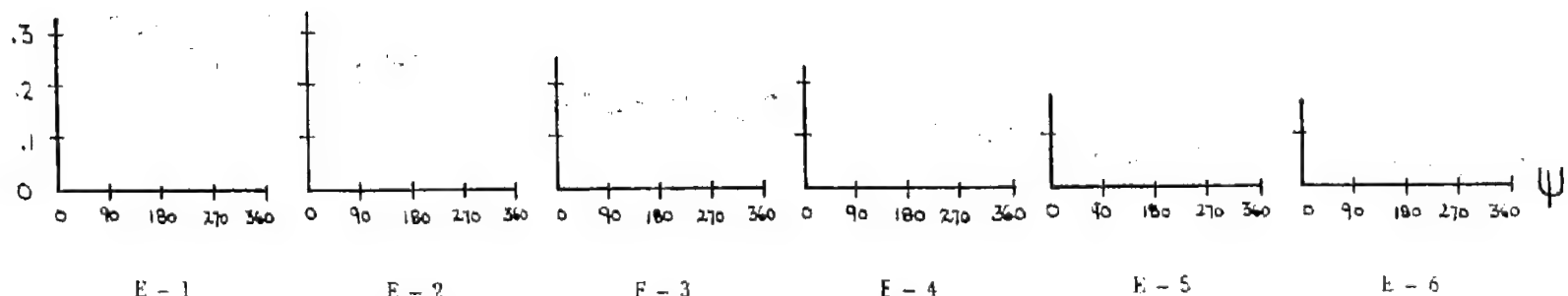
(a) Span station A;  $r/R = 0.325$ .(b) Span station B;  $r/R = 0.460$ .

Figure 36.- Pressure difference in pounds per square inch against azimuth in degrees. Profile, NACA 0015; speed, 800 rpm;  $\xi = 0$ ;  $\mu = 0.30$ ;  $\theta = 8^\circ$ ;  $\alpha = -5^\circ$ .



(c) Span station C;  $r/R = 0.590$ .



(d) Span station E;  $r/R = 0.725$ .



Figure 36.- Continued.

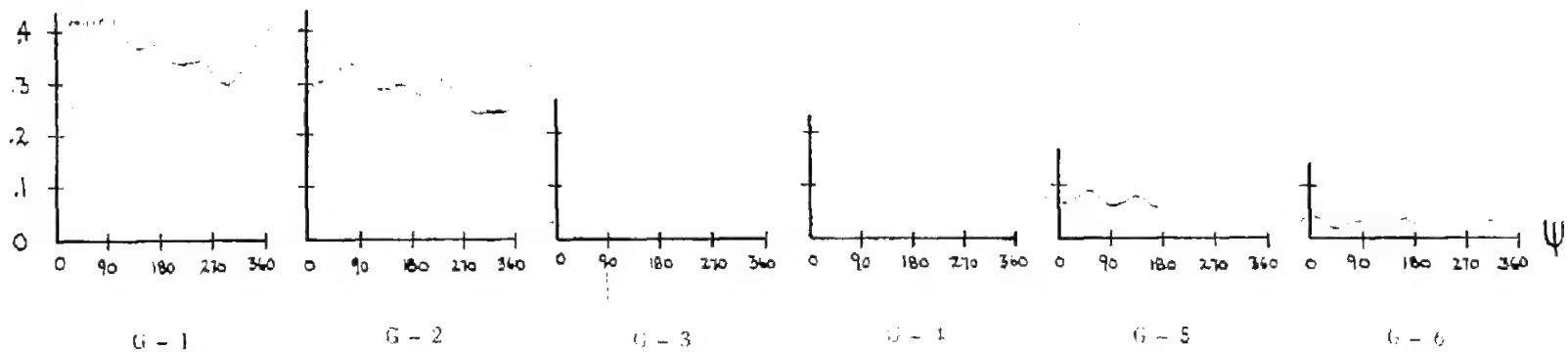
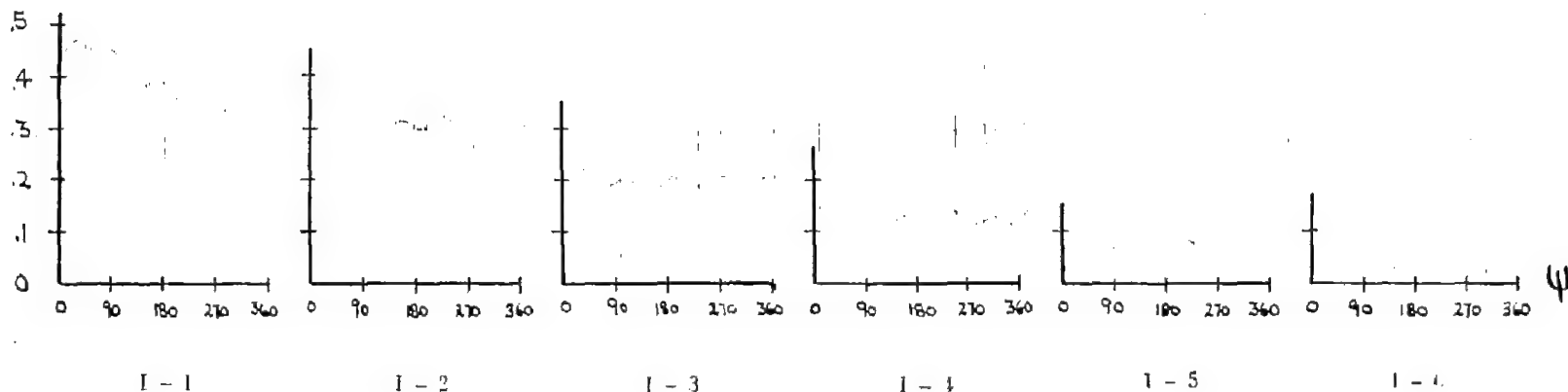
(e) Span station G;  $r/R = 0.825$ .(f) Span station I;  $r/R = 0.890$ .

Figure 36.- Continued.

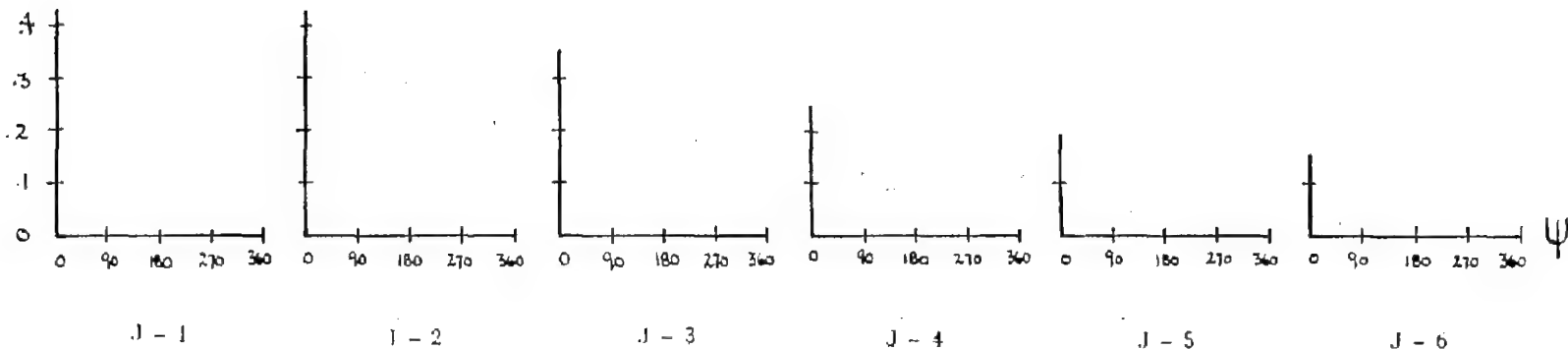
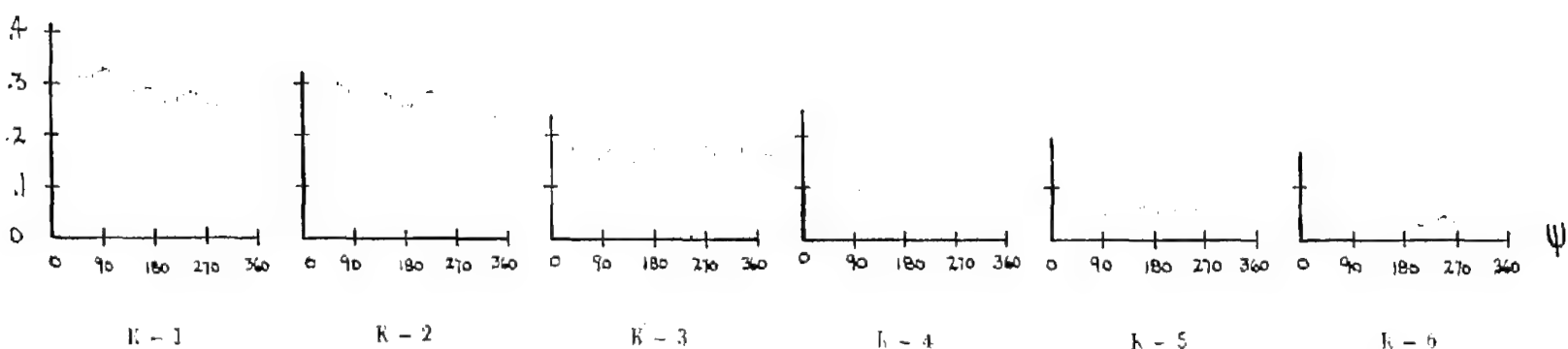
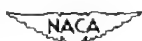
(g) Span station  $J$ ;  $r/R = 0.925$ .(h) Span station  $K$ ;  $r/R = 0.960$ .

Figure 36.- Concluded.

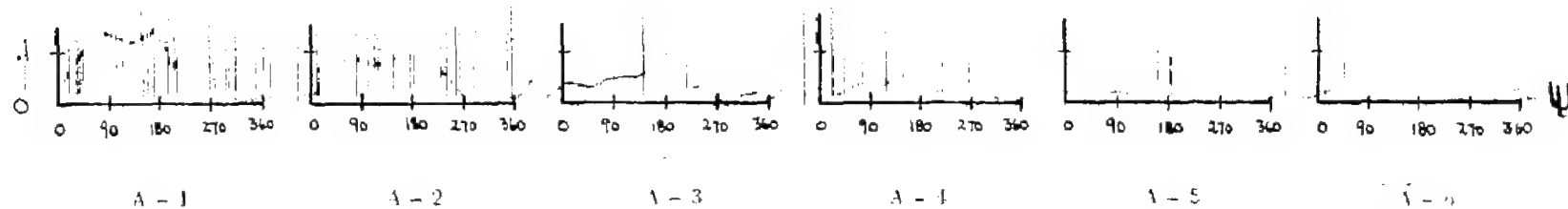
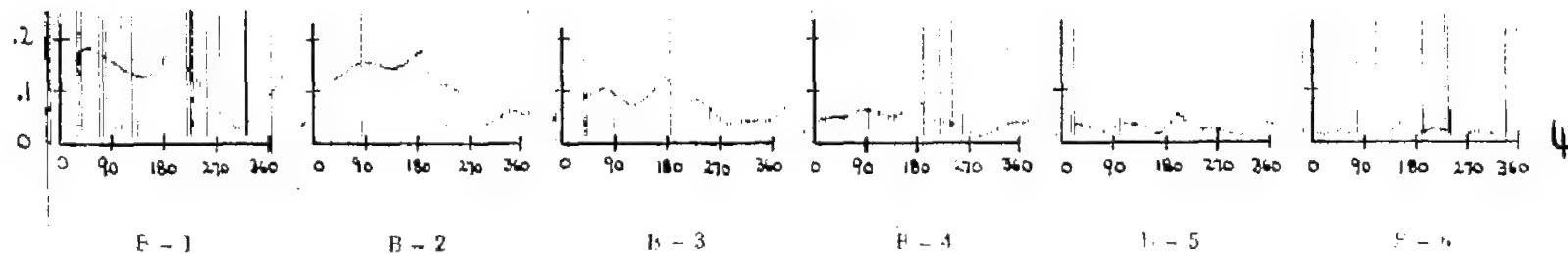
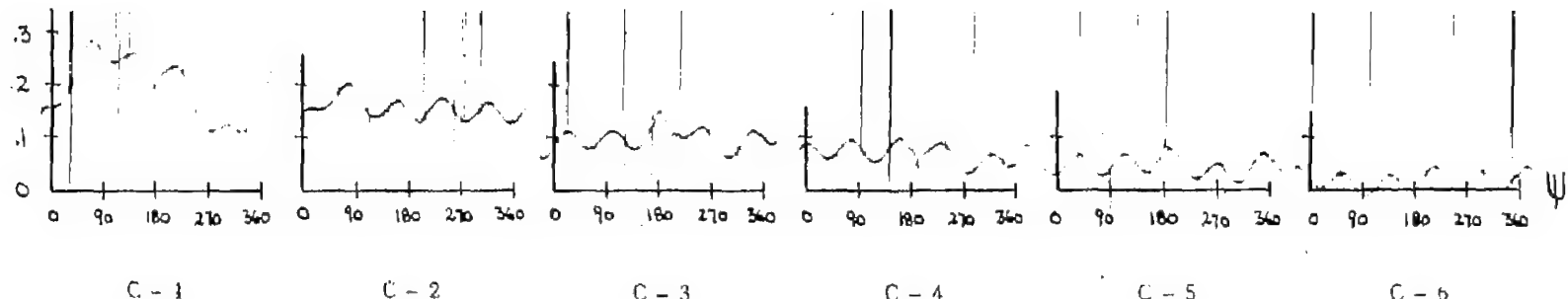
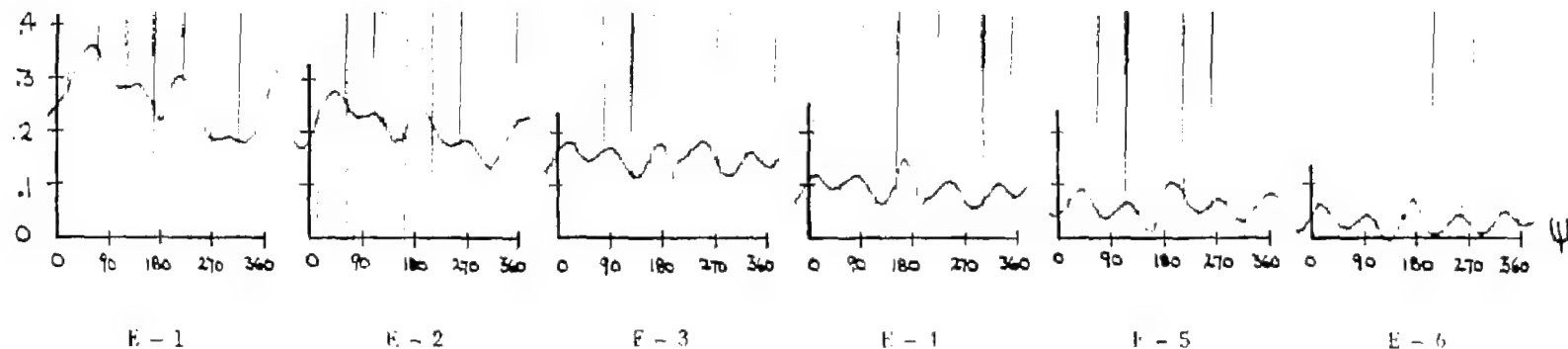
(a) Span station A;  $r/R = 0.325$ .(b) Span station B;  $r/R = 0.460$ .

Figure 37.- Pressure difference in pounds per square inch against azimuth in degrees. Profile, NACA 0015; speed, 800 rpm;  $\xi = 0$ ;  $\mu = 0.40$ ;  $\theta = 8^\circ$ ;  $\alpha = -5^\circ$ .



(c) Span station C;  $r/R = 0.590.$



(d) Span station E;  $r/R = 0.725.$

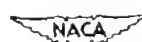


Figure 37.- Continued.

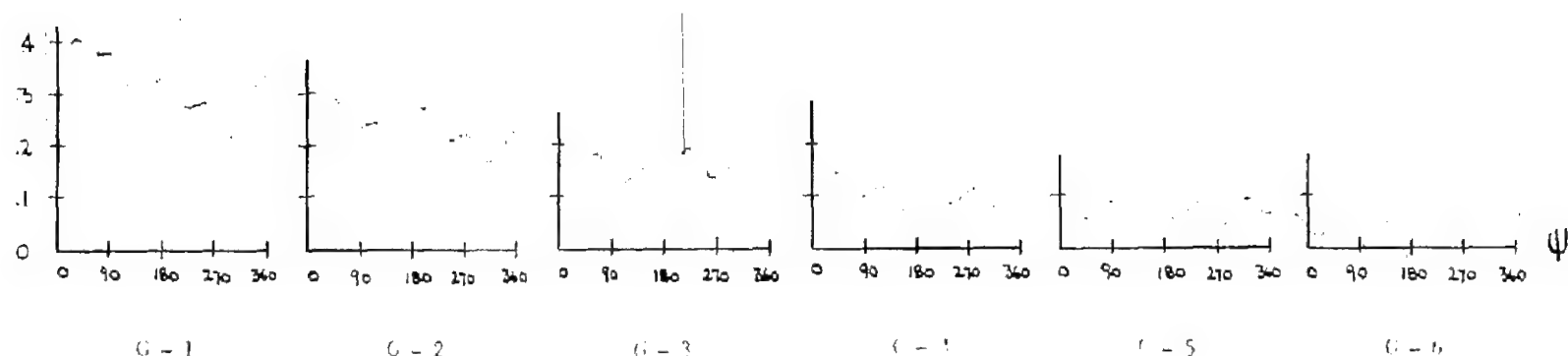
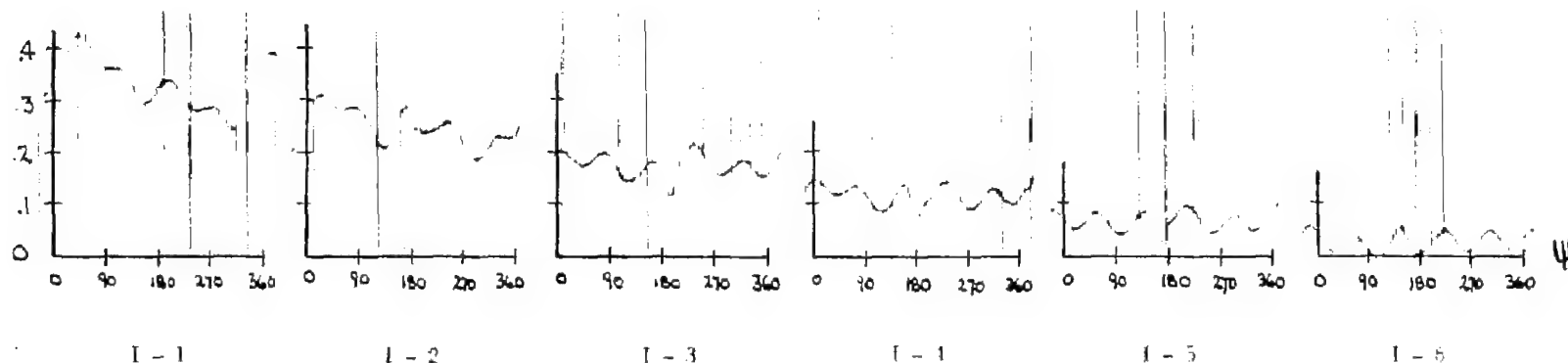
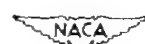
(e) Span station G;  $r/R = 0.825$ .(f) Span station I;  $r/R = 0.890$ .

Figure 37.- Continued.

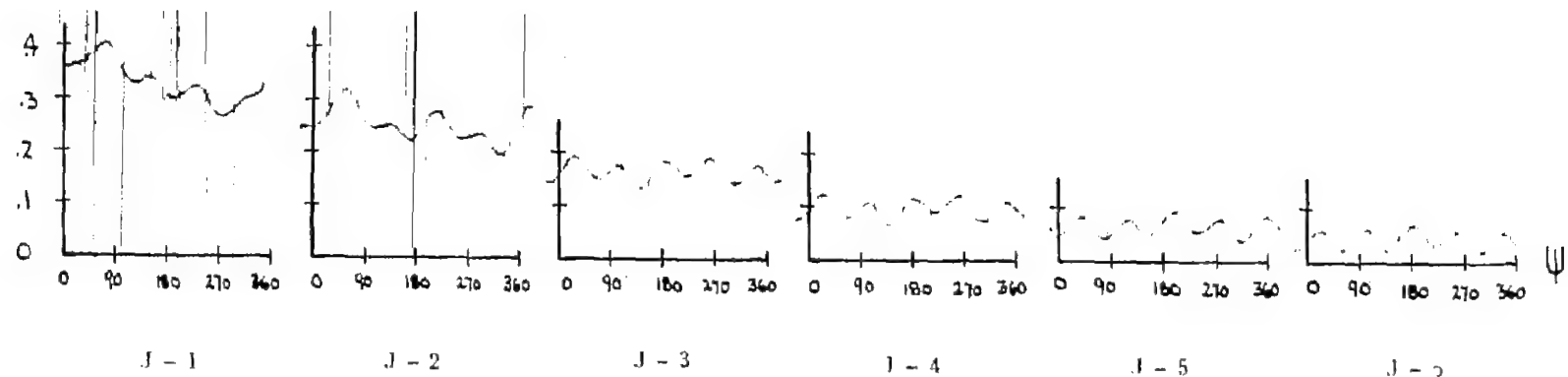
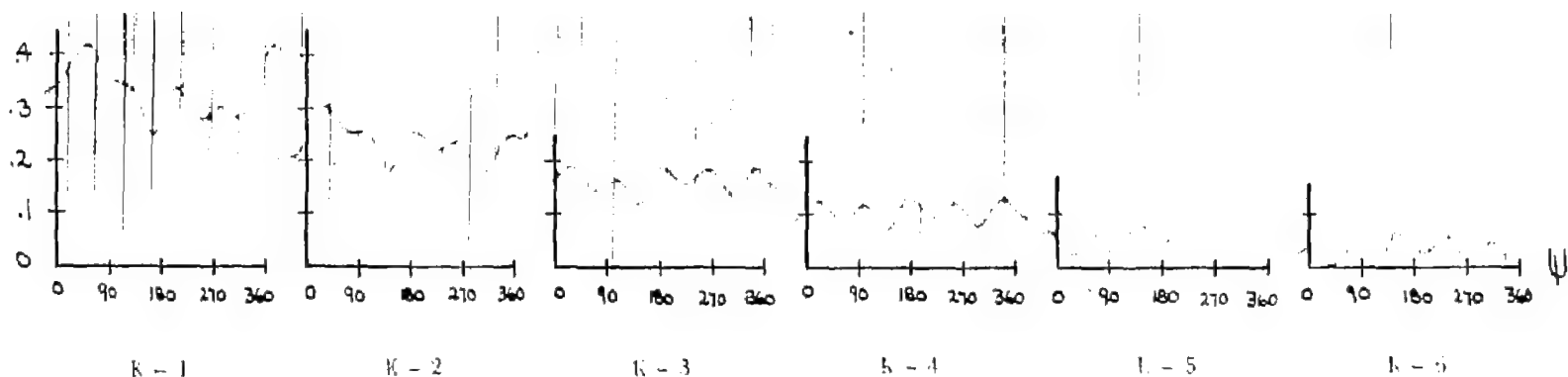
(g) Span station J;  $r/R = 0.925$ .(h) Span station K;  $r/R = 0.960$ .

Figure 37.- Concluded.

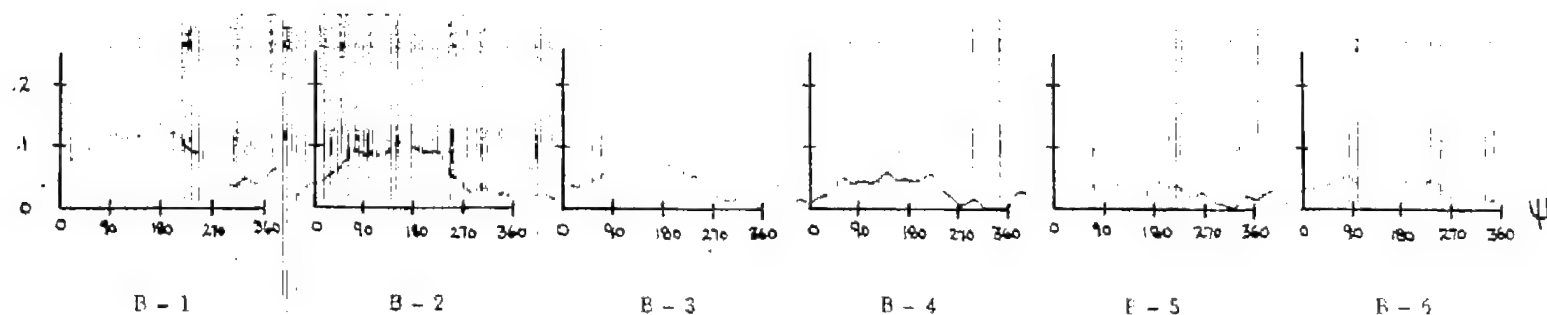
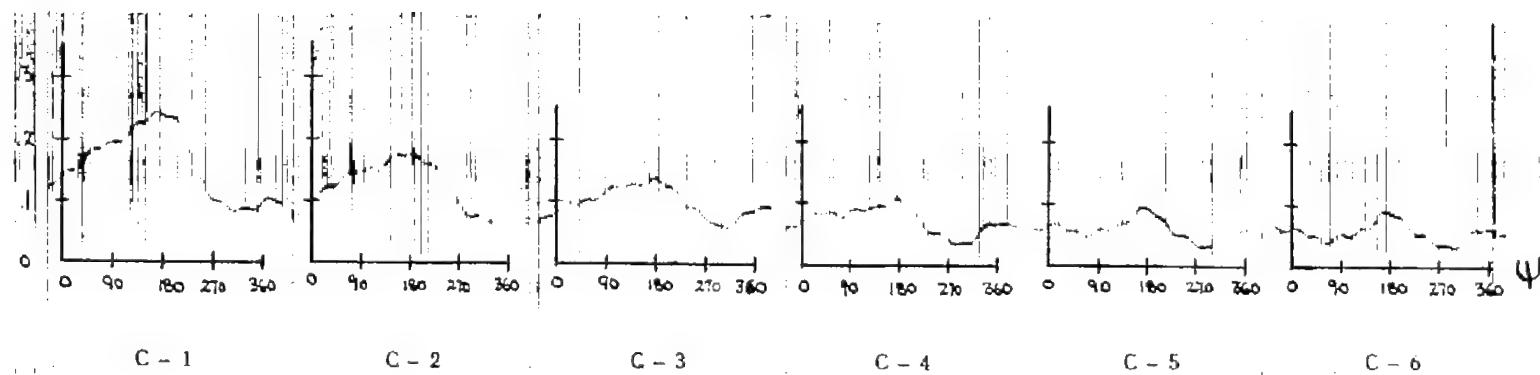
(a) Span station B;  $r/R = 0.460$ .(b) Span station C;  $r/R = 0.590$ .

Figure 38.- Pressure difference in pounds per square inch against azimuth in degrees. Profile, NACA 0015; speed, 800 rpm;  $\xi = 0.13$ ;  $\mu = 0.10$ ;  $\theta = 8^\circ$ ;  $\alpha = -5^\circ$ .

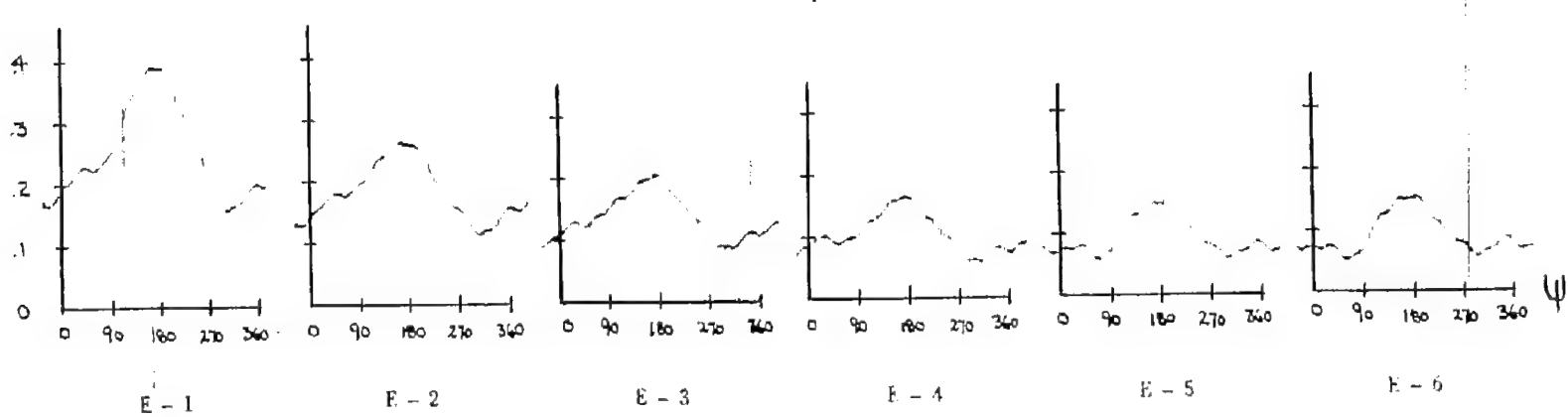
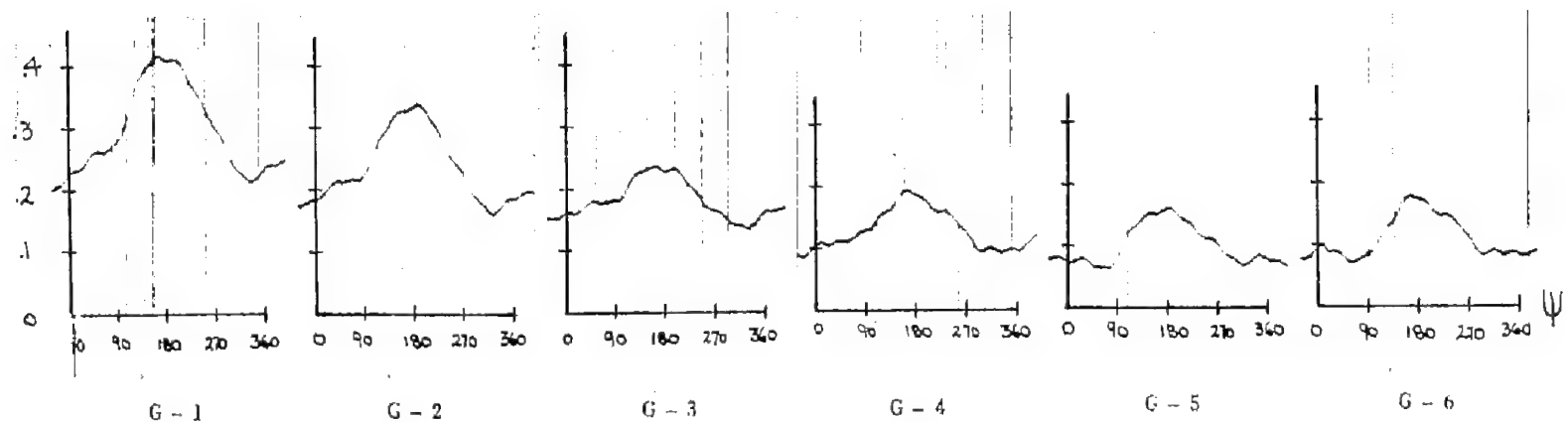
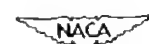
(c) Span station E;  $r/R = 0.725$ .(d) Span station G;  $r/R = 0.825$ .

Figure 38.- Continued.

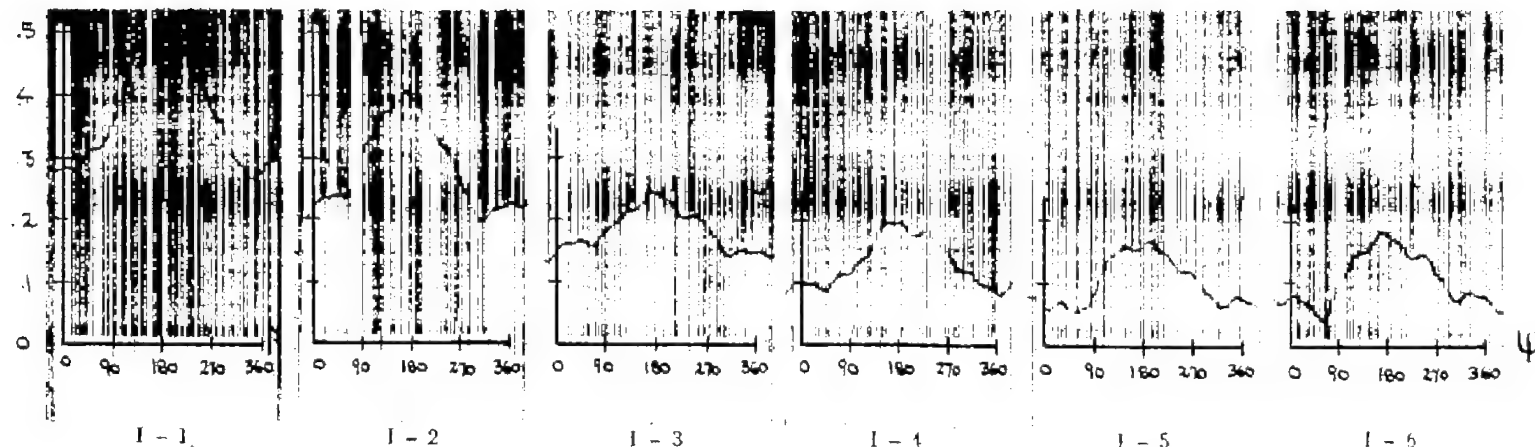
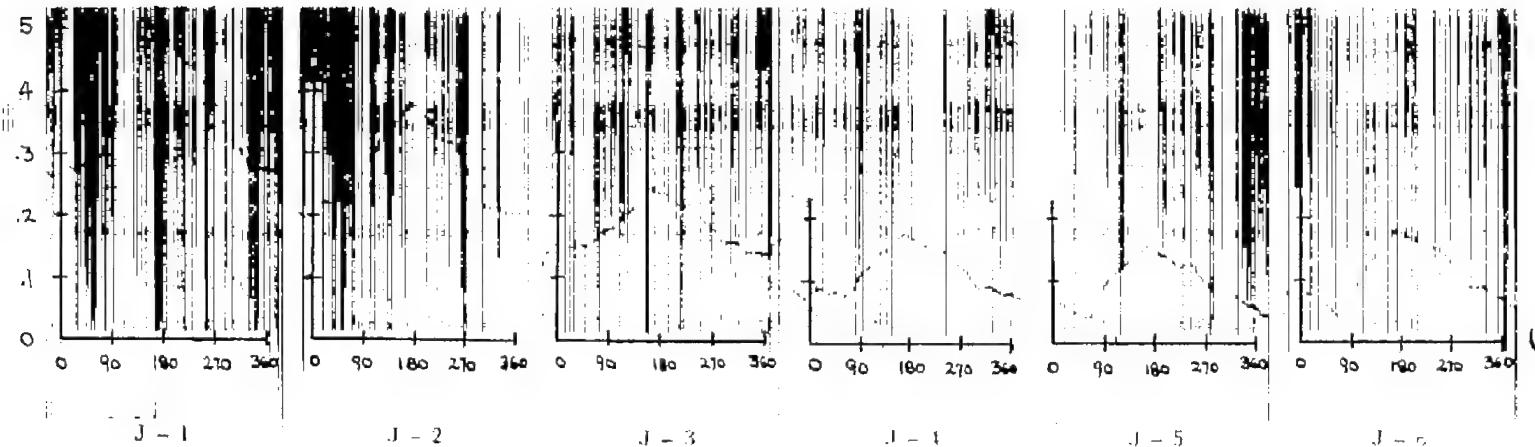
(e) Span station I;  $r/R = 0.890$ .(f) Span station J;  $r/R = 0.925$ .

Figure 38.- Continued.

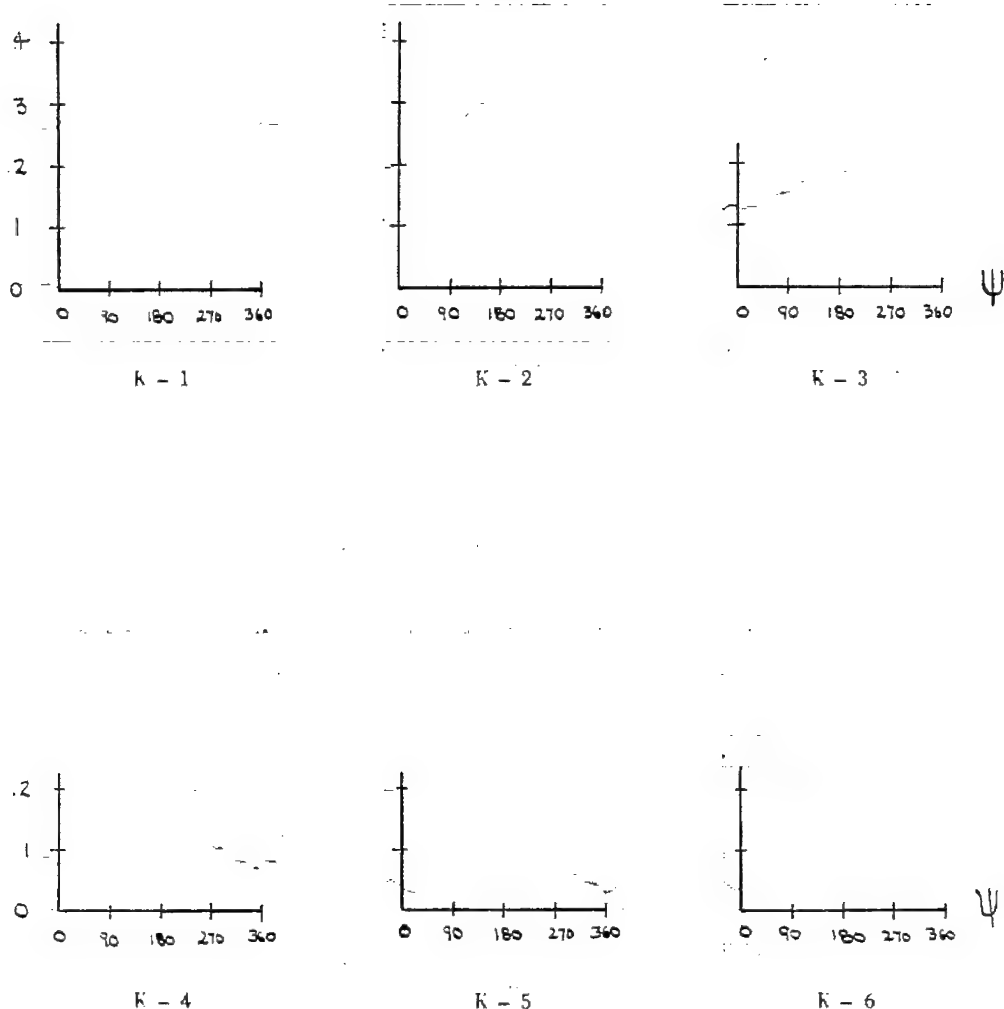
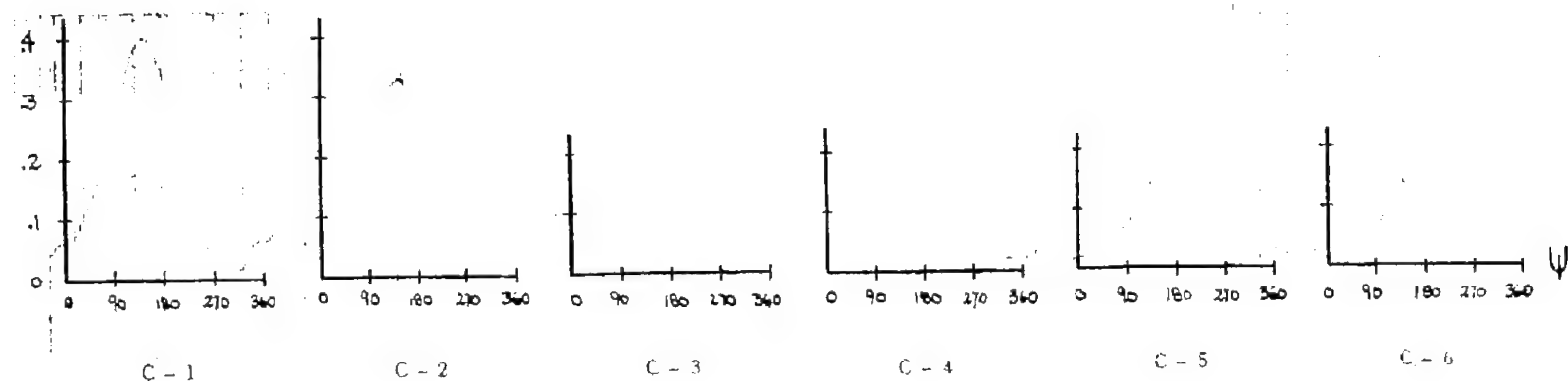
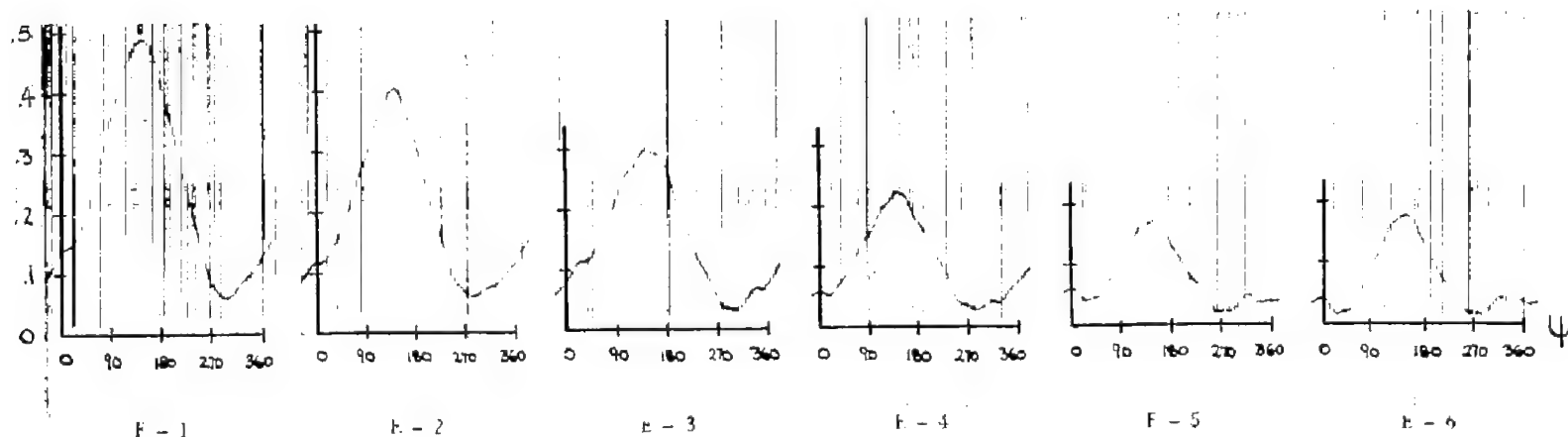
(g) Span station K;  $r/R = 0.960.$ 

Figure 38.- Concluded.



(a) Span station C;  $r/R = 0.590$ .



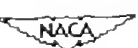
(b) Span station E;  $r/R = 0.725$ . 

Figure 39.- Pressure difference in pounds per square inch against azimuth in degrees. Profile, NACA 0015; speed, 800 rpm;  $\xi = 0.13$ ;  $\mu = 0.30$ ;  $\theta = 8^{\circ}$ ;  $\alpha = -5^{\circ}$ .

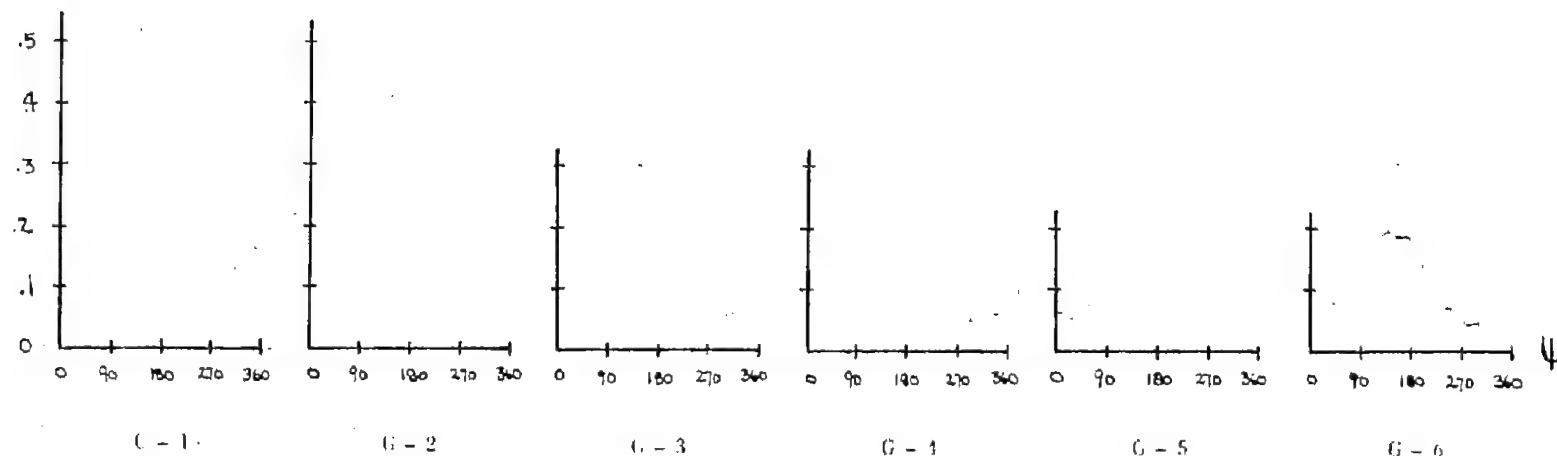
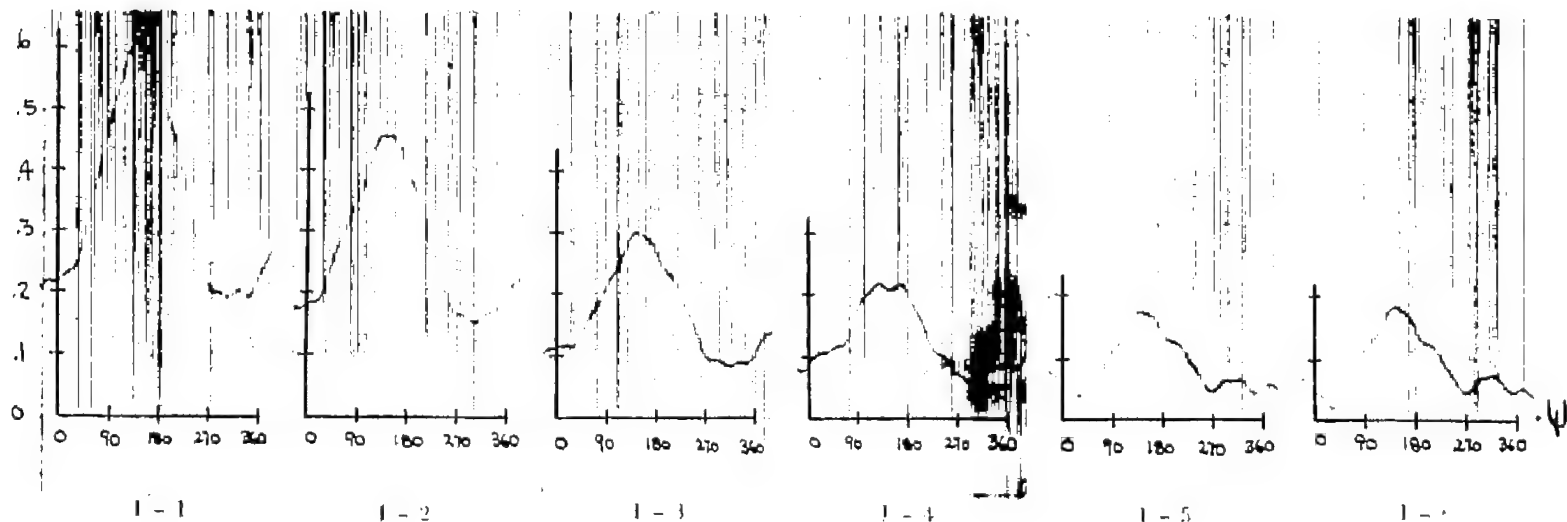
(c) Span station G;  $r/R = 0.825$ .(d) Span station I;  $r/R = 0.890$ .

Figure 39.- Continued.

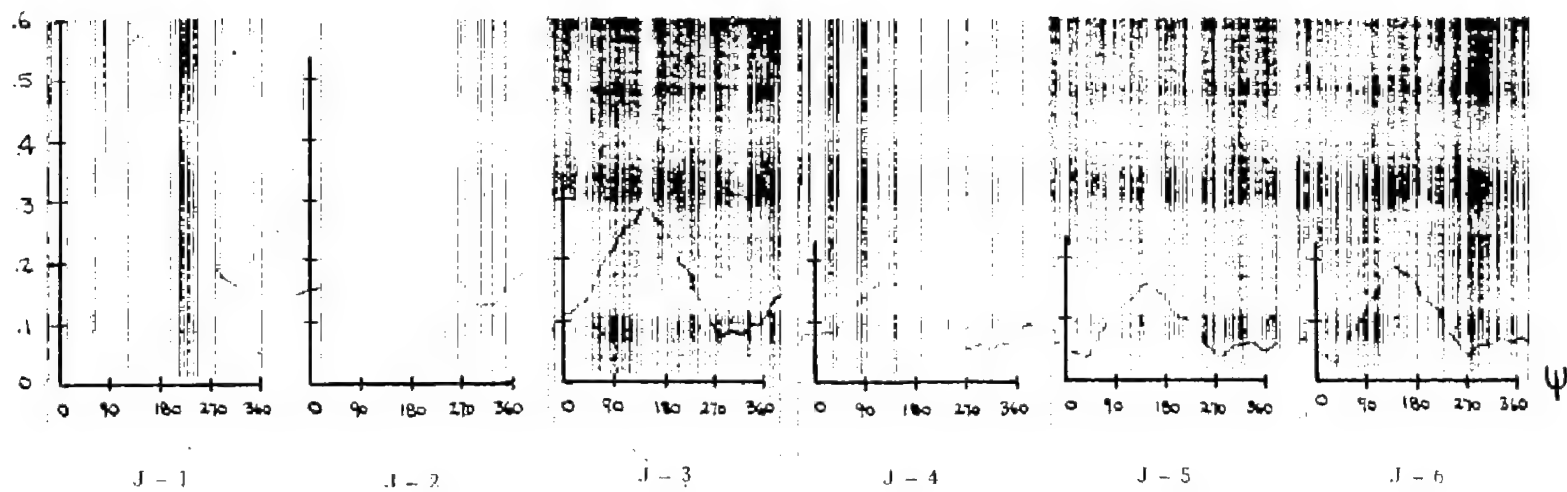
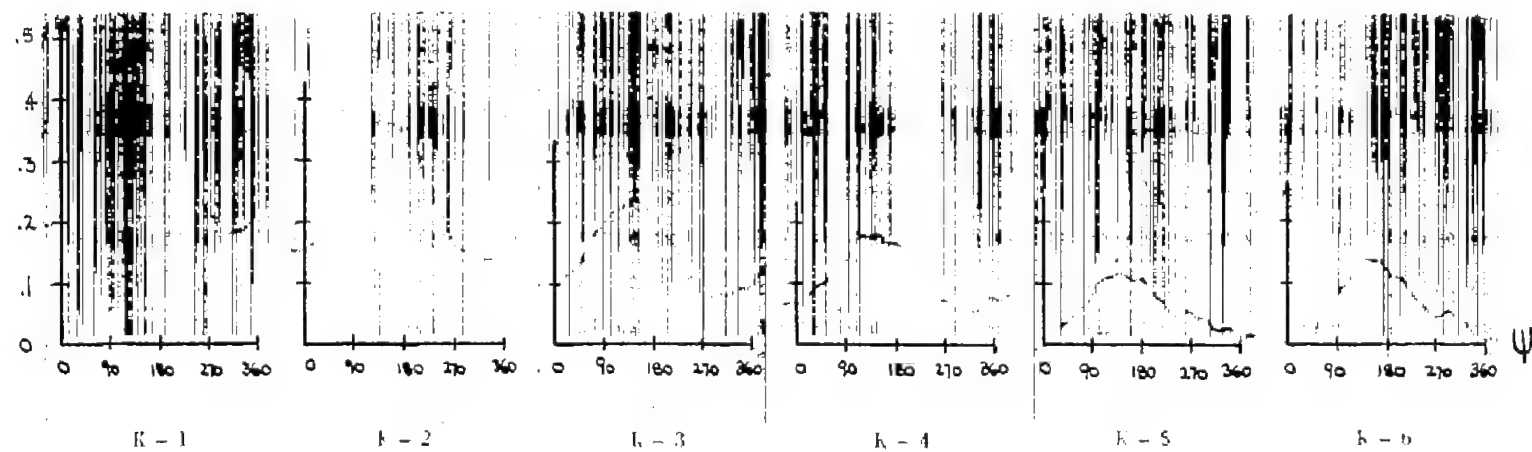
(e) Span station J;  $r/R = 0.925$ .(f) Span station K;  $r/R = 0.960$ .

Figure 39.- Concluded.



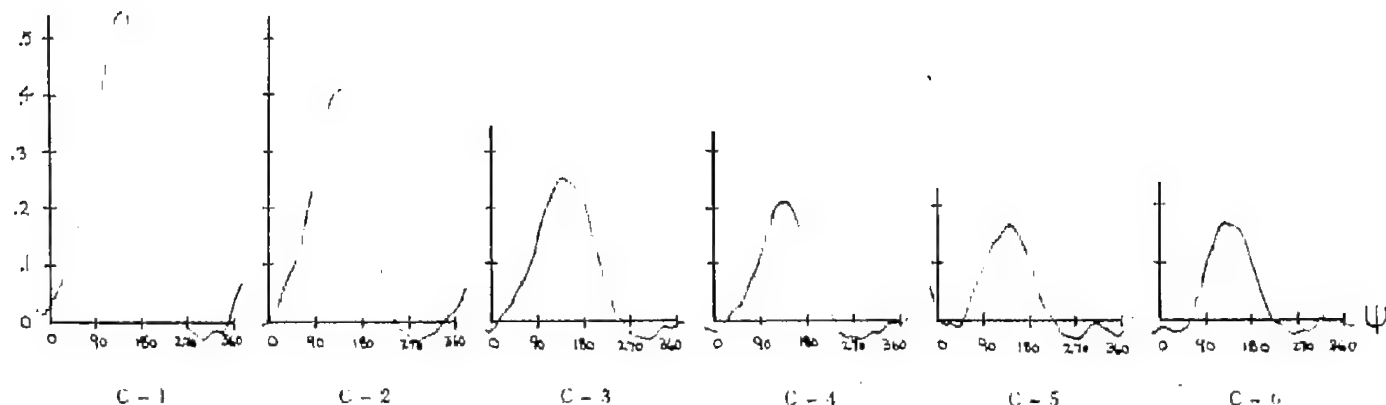
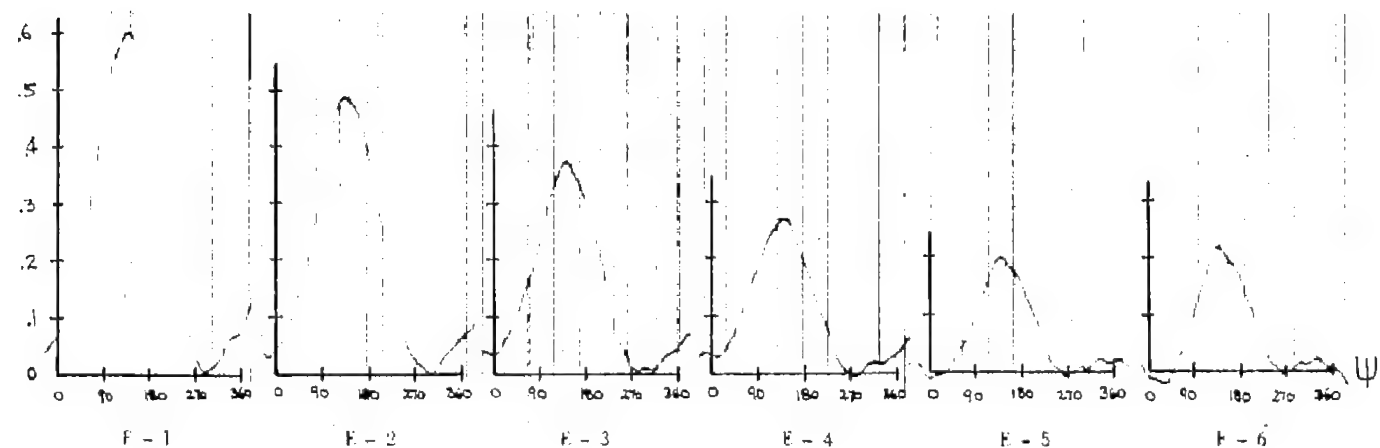
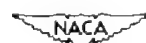
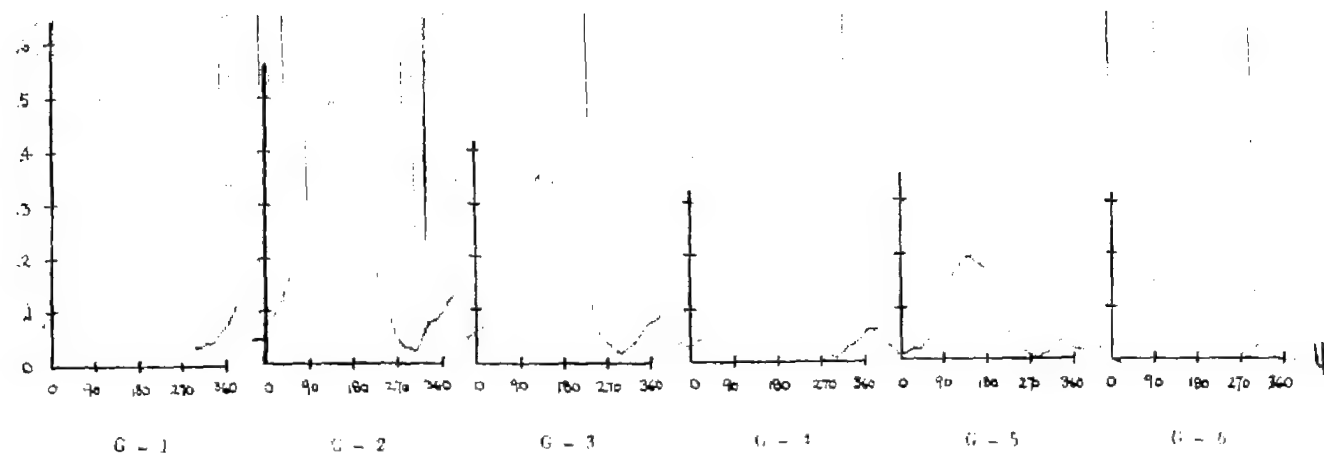
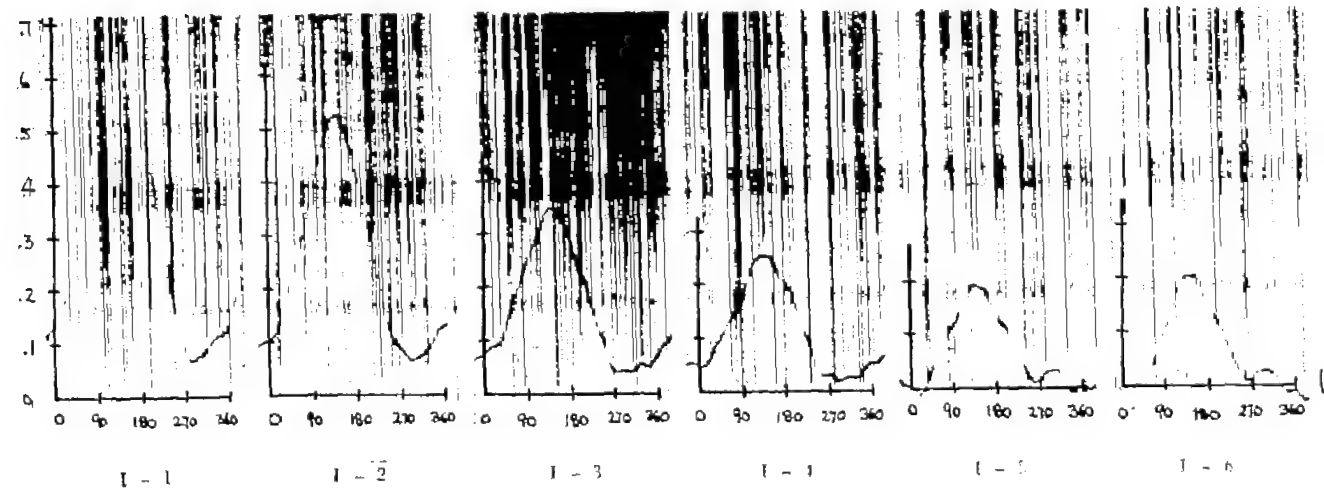
(a) Span station C;  $r/R = 0.590$ .(b) Span station E;  $r/R = 0.725$ .

Figure 40.- Pressure difference in pounds per square inch against azimuth in degrees. Profile, NACA 0015; speed, 800 rpm;  $\xi = 0.13$ ;  $\mu = 0.45$ ;  $\theta = 8^\circ$ ;  $\alpha = -5^\circ$ .



(c) Span station G;  $r/R = 0.825$ .



(d) Span station I;  $r/R = 0.890$ .



Figure 40.- Continued.

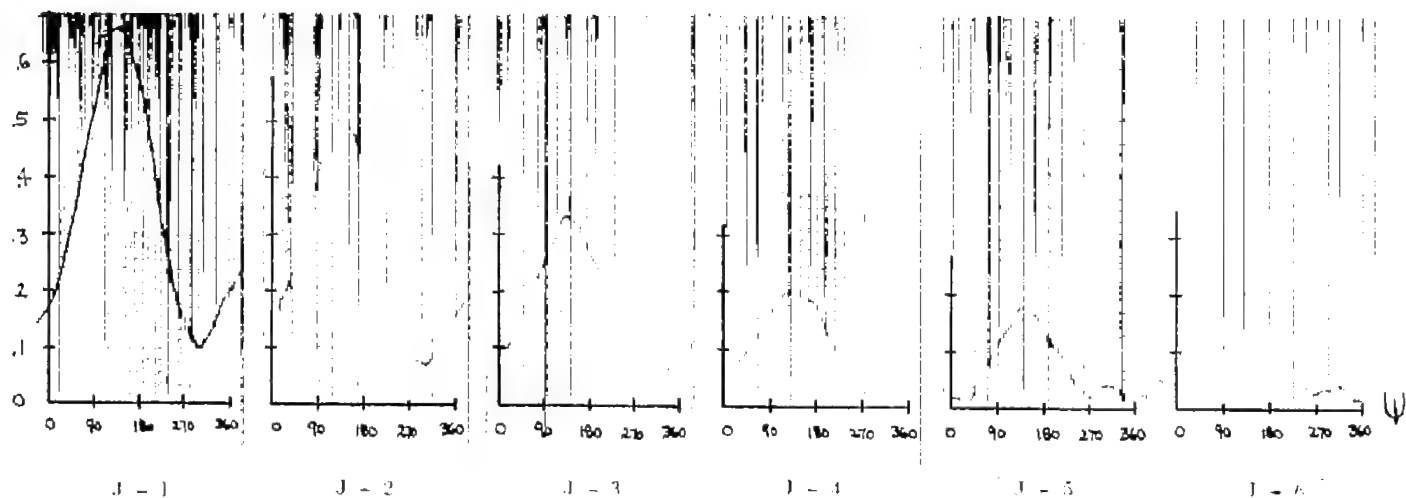
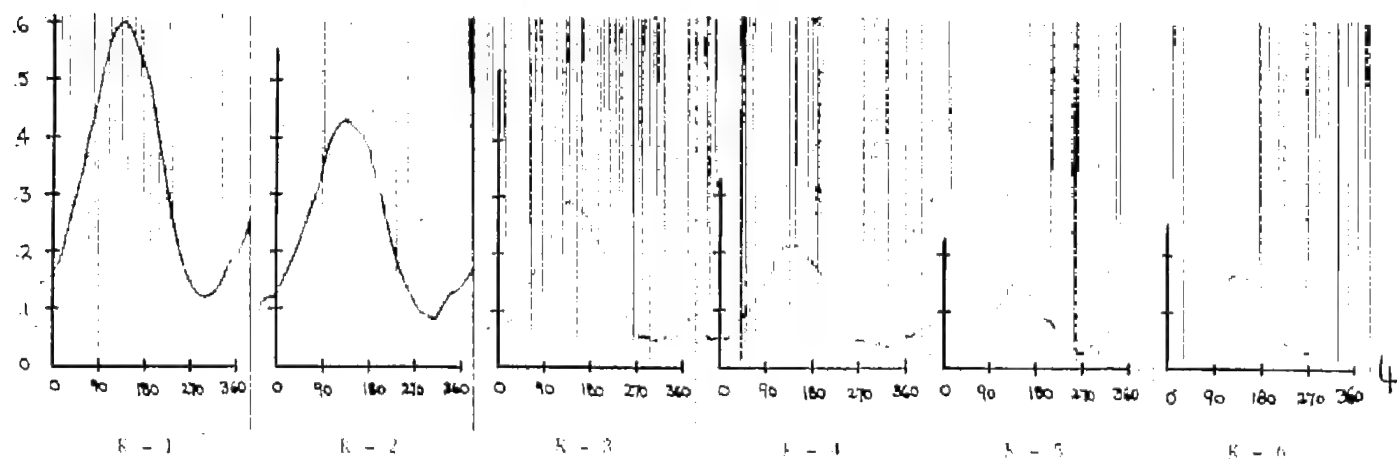
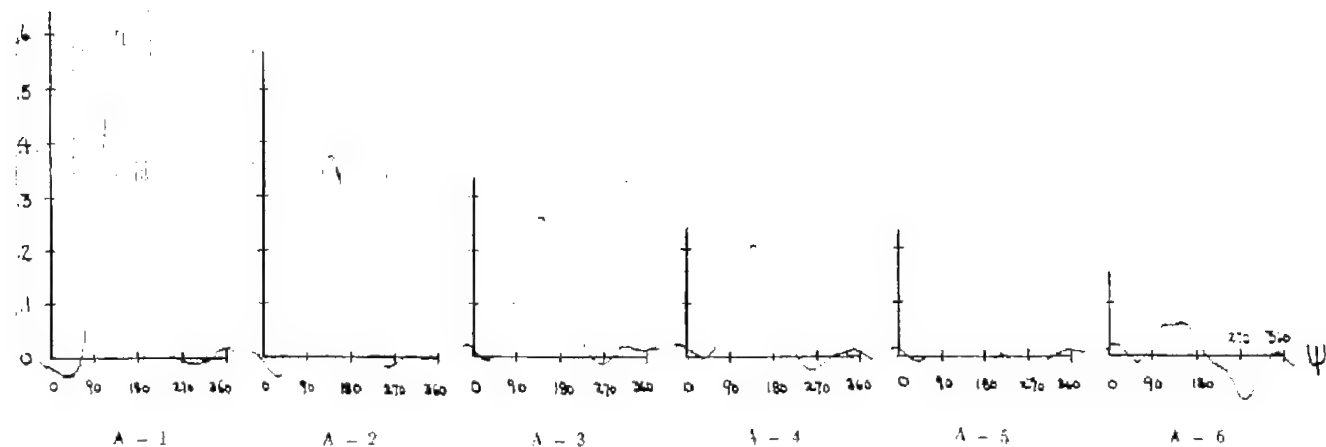
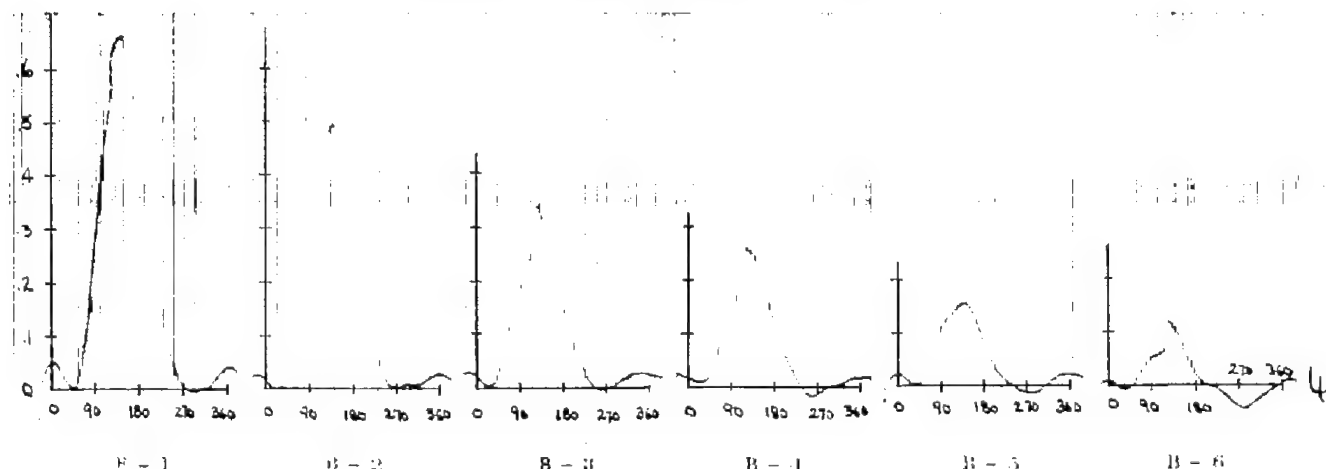
(e) Span station J;  $r/R = 0.925$ .(f) Span station K;  $r/R = 0.960$ .

Figure 40.- Concluded.



(a) Span station A;  $r/R = 0.325$ .



(b) Span station B;  $r/R = 0.460$



Figure 41.- Pressure difference in pounds per square inch against azimuth in degrees. Profile, NACA 0015; speed, 800 rpm;  $\xi = 0.13$ ;  $\mu = 0.60$ ;  $\theta = 8^\circ$ ;  $\alpha = -5^\circ$ .

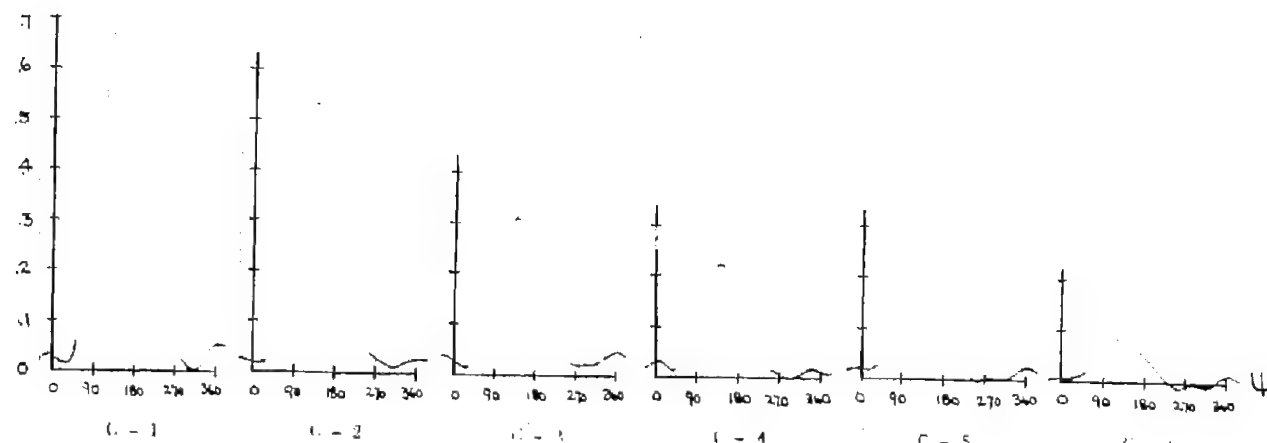
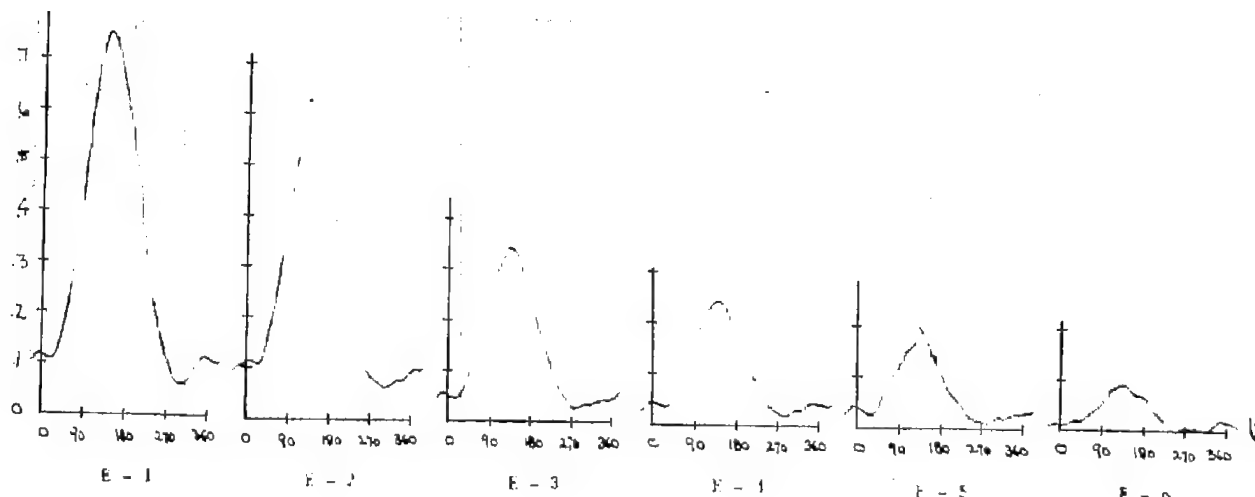
(c) Span station C;  $r/R = 0.590$ .(d) Span station E;  $r/R = 0.725$ .

Figure 41.- Continued.

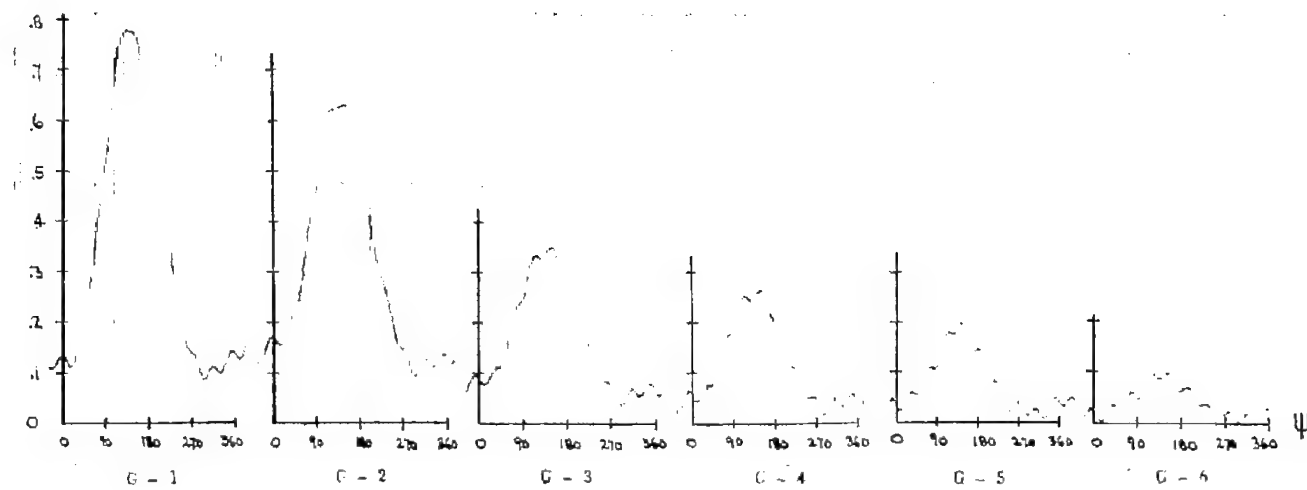
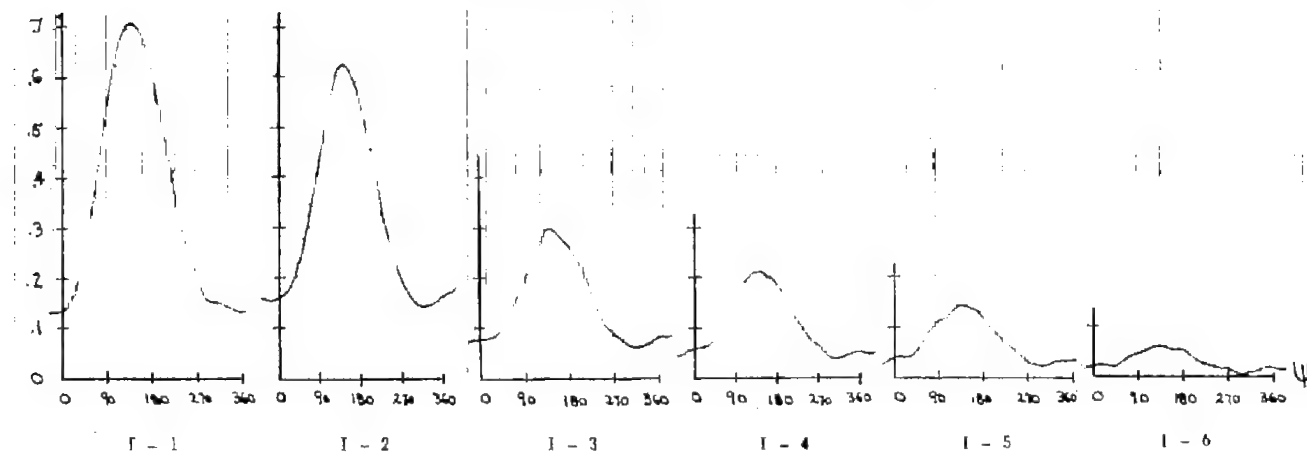
(e) Span station G;  $r/R = 0.825$ .(f) Span station I;  $r/R = 0.890$ .

Figure 41.- Continued.

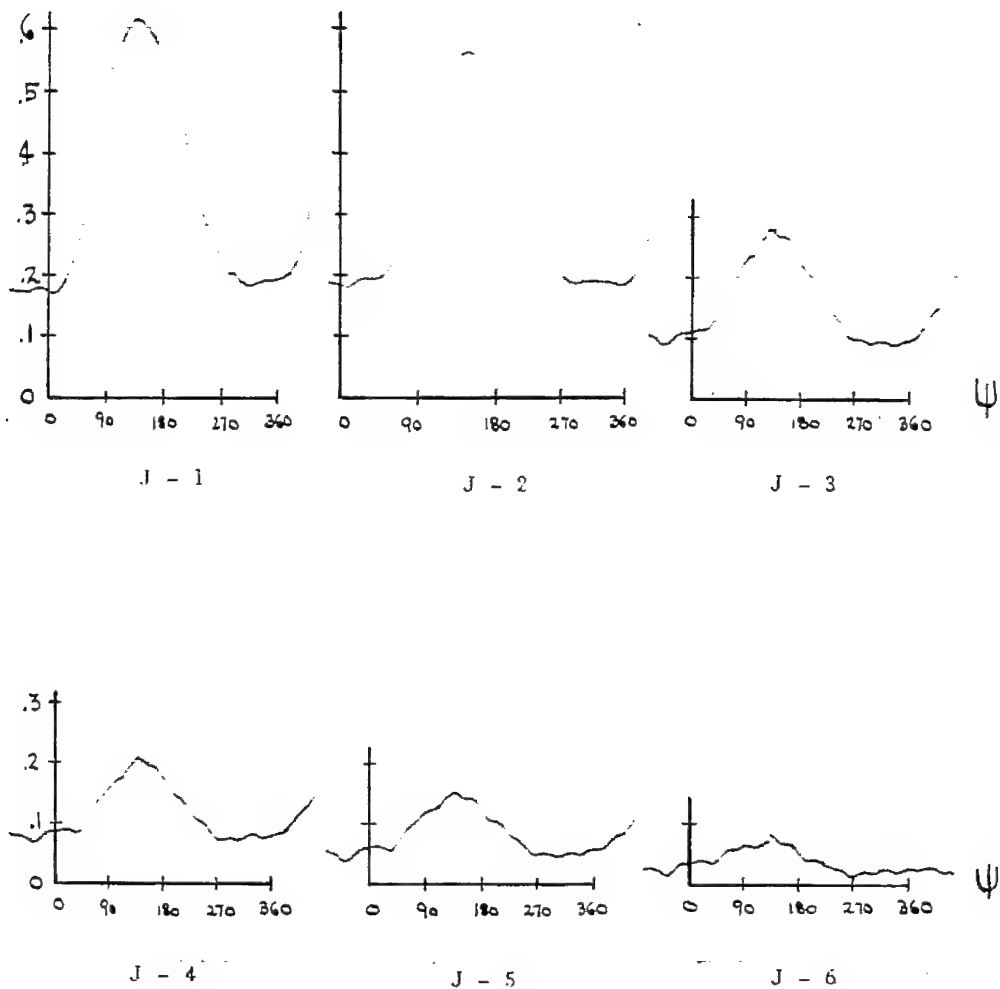
(g) Span station  $J$ ;  $r/R = 0.925$ .

Figure 41.- Continued.

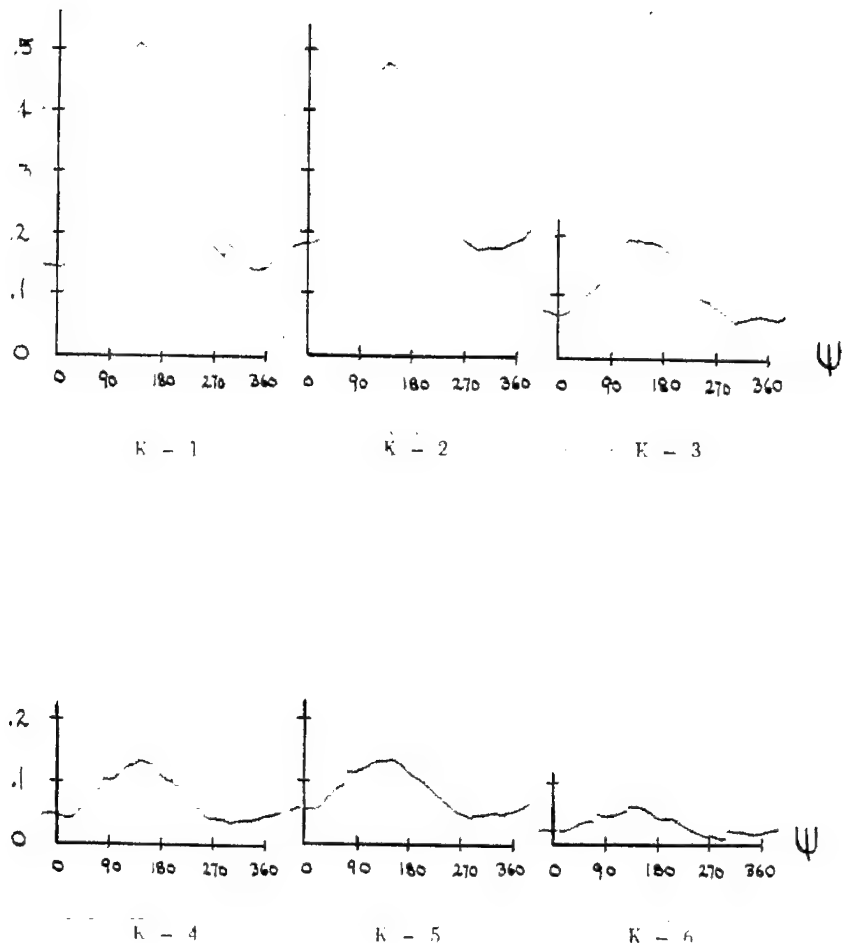
(h) Span station K;  $r/R = 0.960$ .

Figure 41.- Concluded.

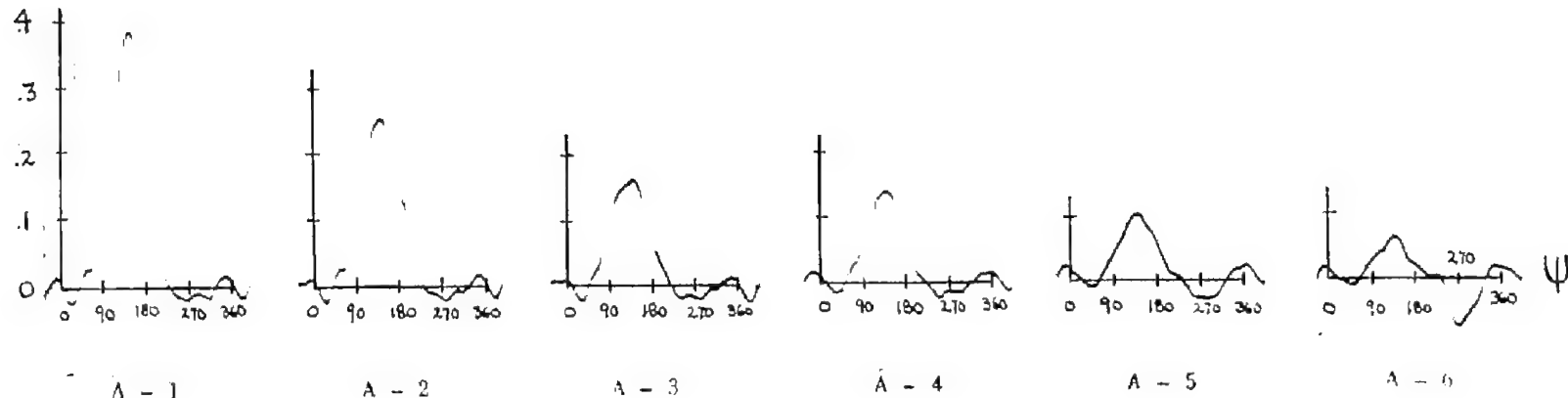
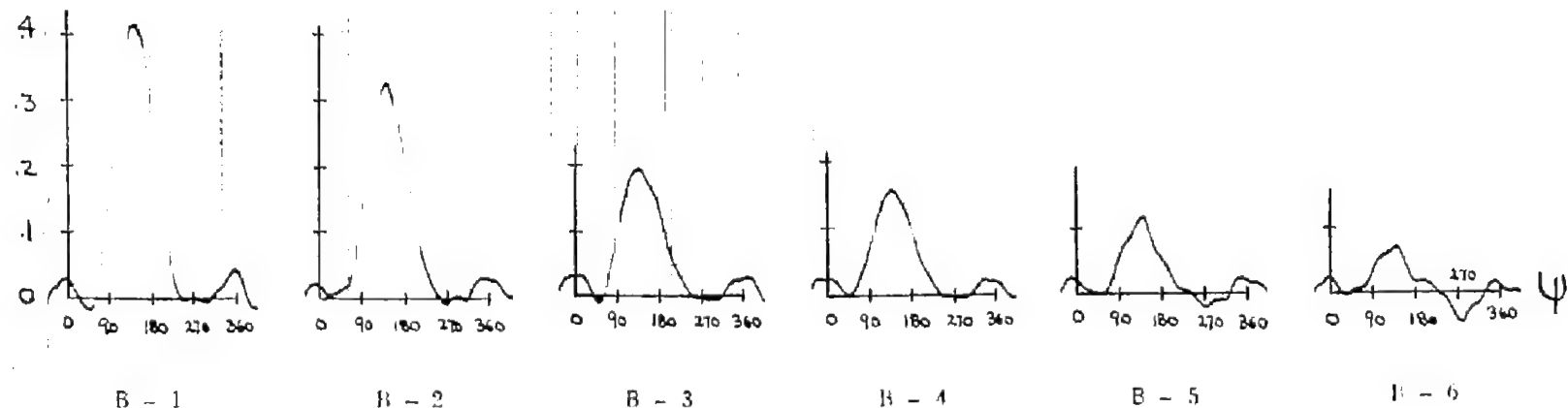
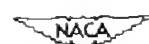
(a) Span station A;  $r/R = 0.325$ .(b) Span station B;  $r/R = 0.460$ .

Figure 42.- Pressure difference in pounds per square inch against azimuth in degrees. Profile, NACA 0015; speed, 500 rpm;  $\xi = 0.13$ ;  $\mu = 0.80$ ;  $\theta = 8^\circ$ ;  $\alpha = -5^\circ$ .

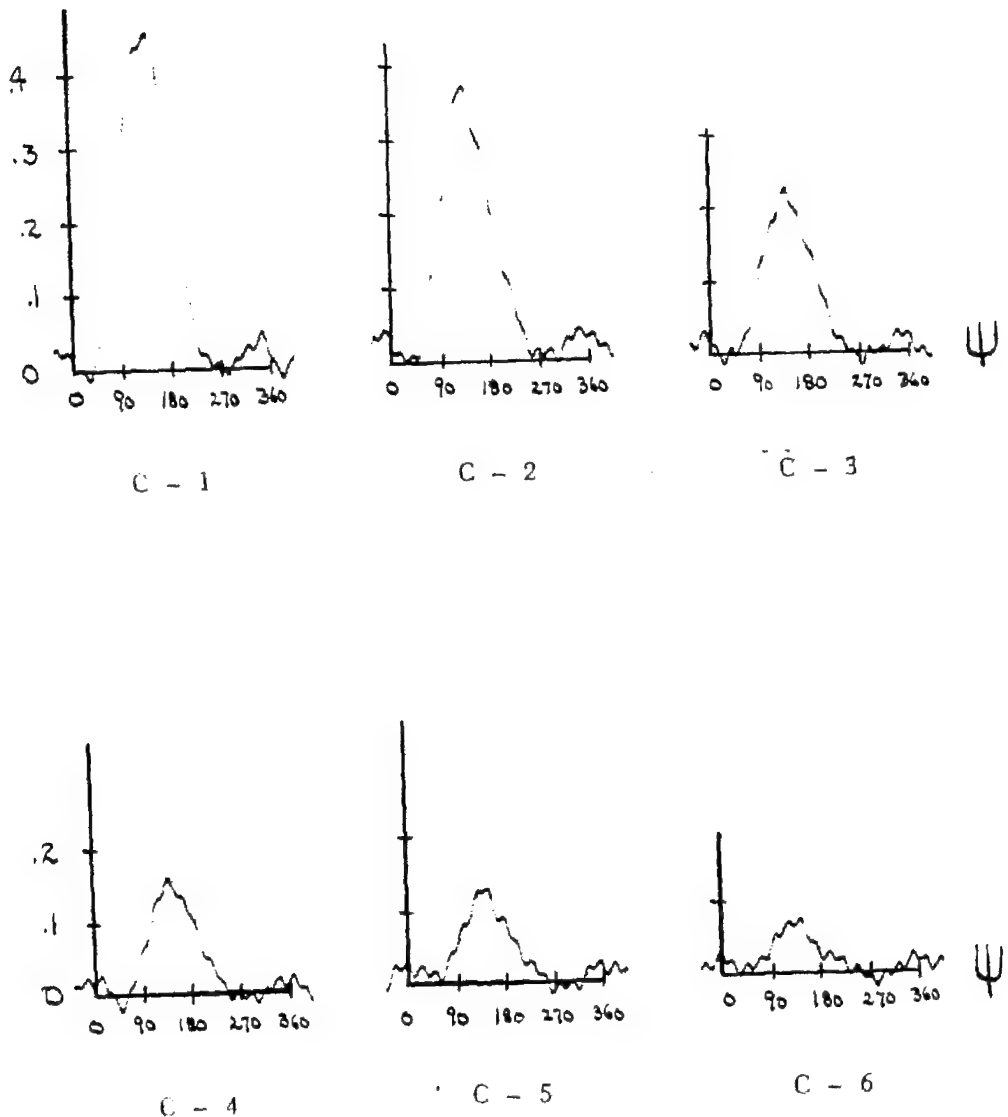
(c) Span station C;  $r/R = 0.590$ .

Figure 42.- Continued.

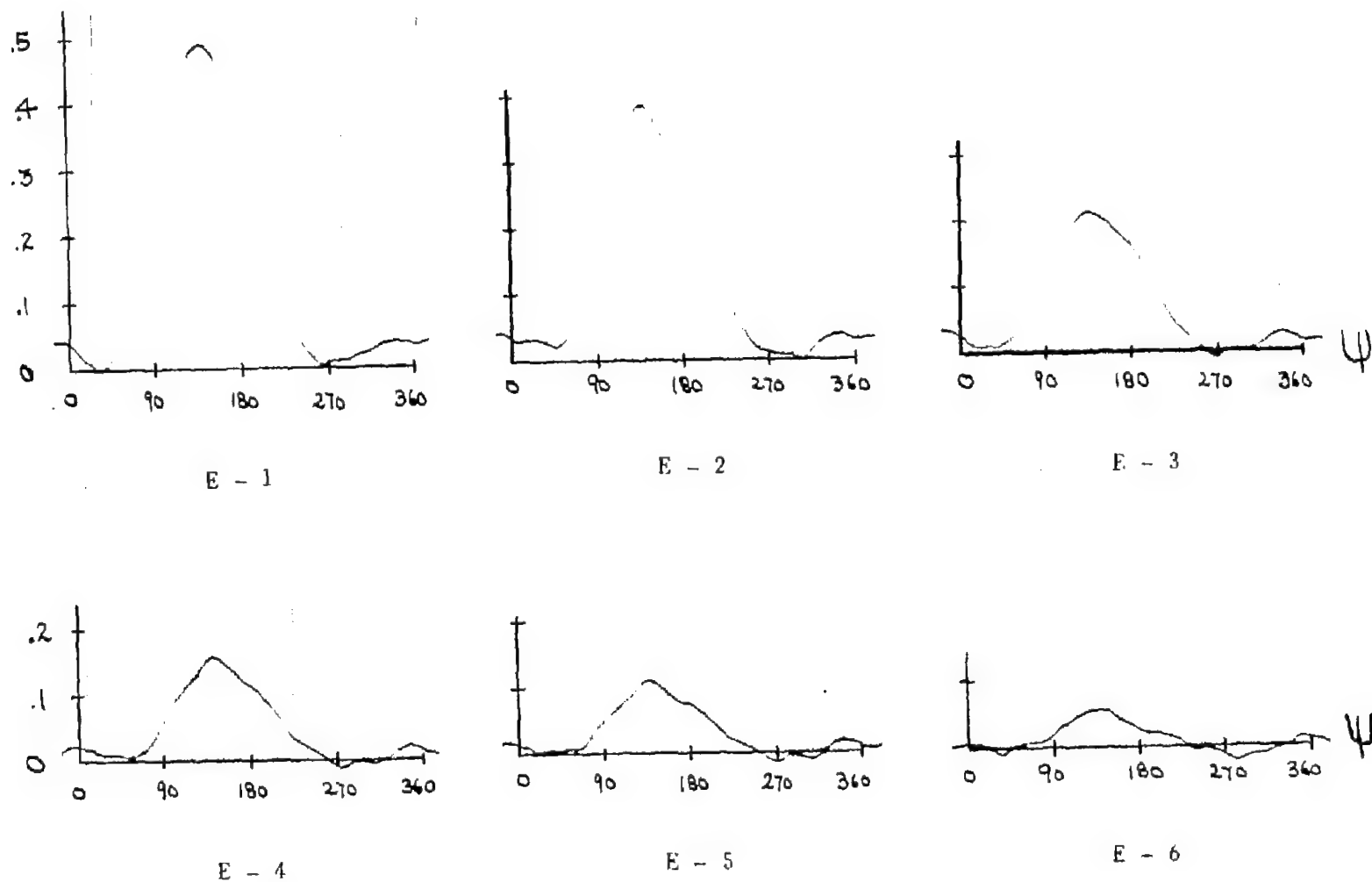
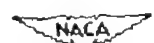
(d) Span station E;  $r/R = 0.725.$ 

Figure 42.- Continued.



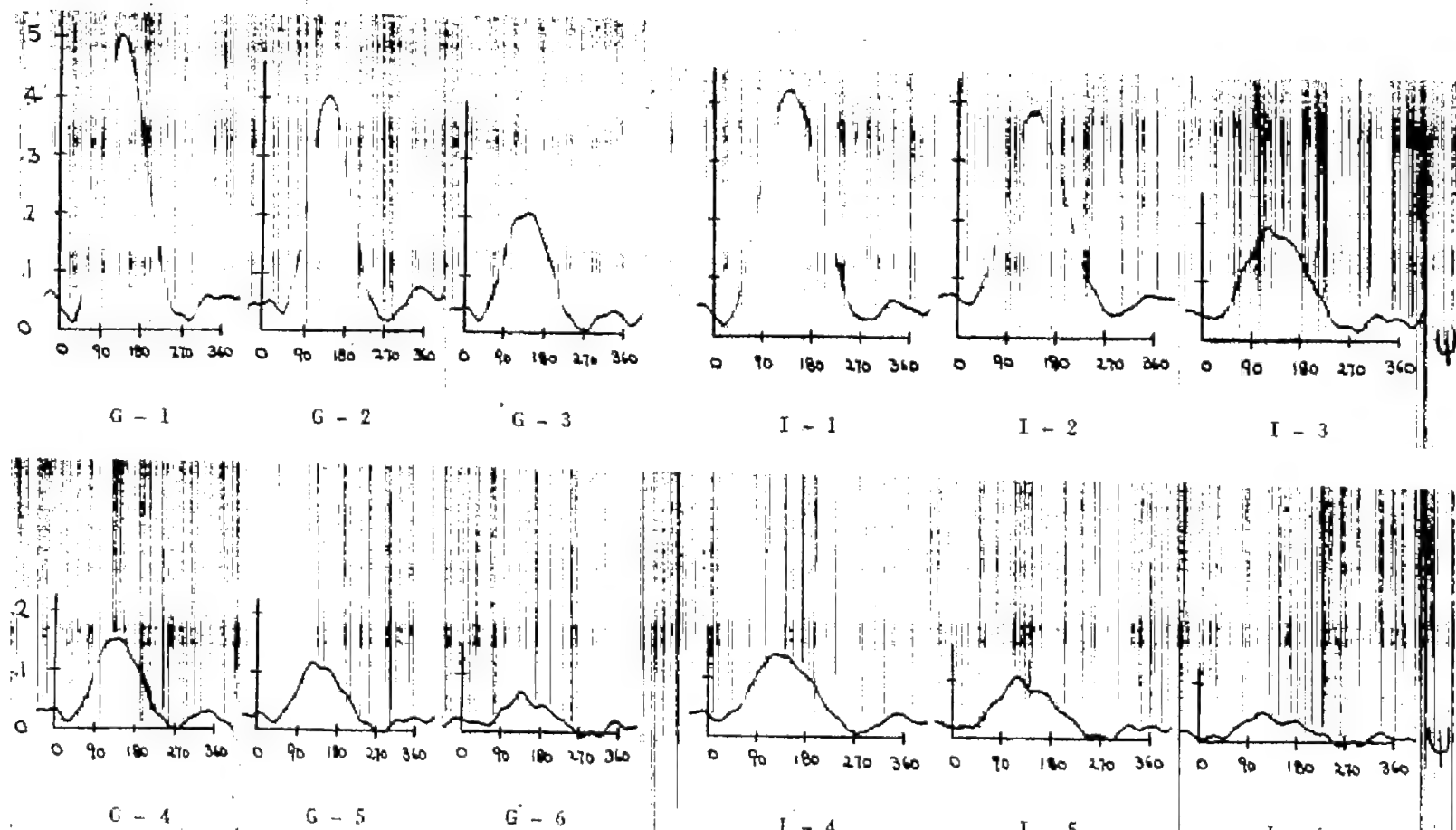
(e) Span station G;  $r/R = 0.825$ .(f) Span station I;  $r/R = 0.890$ .

Figure 42.- Continued.



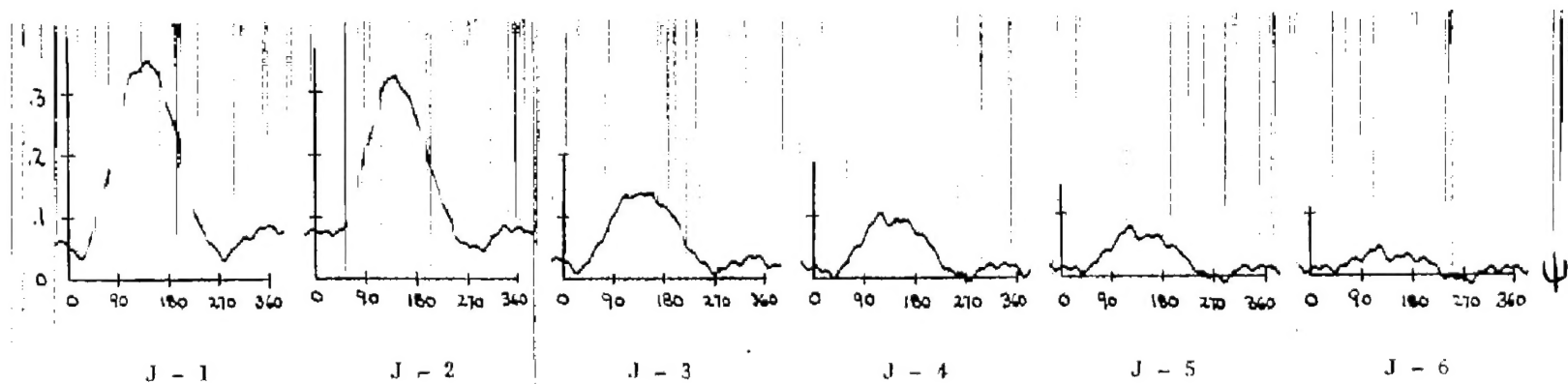
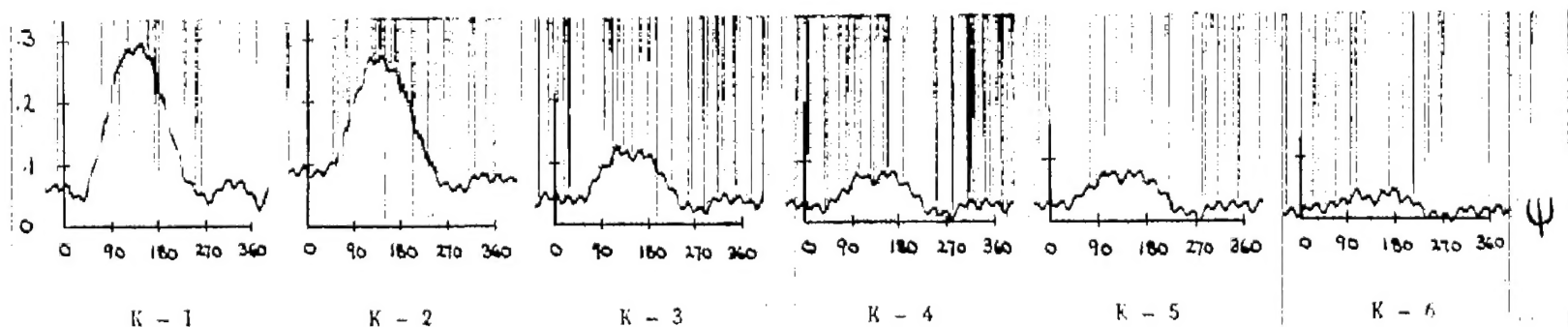
(g) Span station J;  $r/R = 0.925$ .(h) Span station K;  $r/R = 0.960$ .

Figure 42.- Concluded.

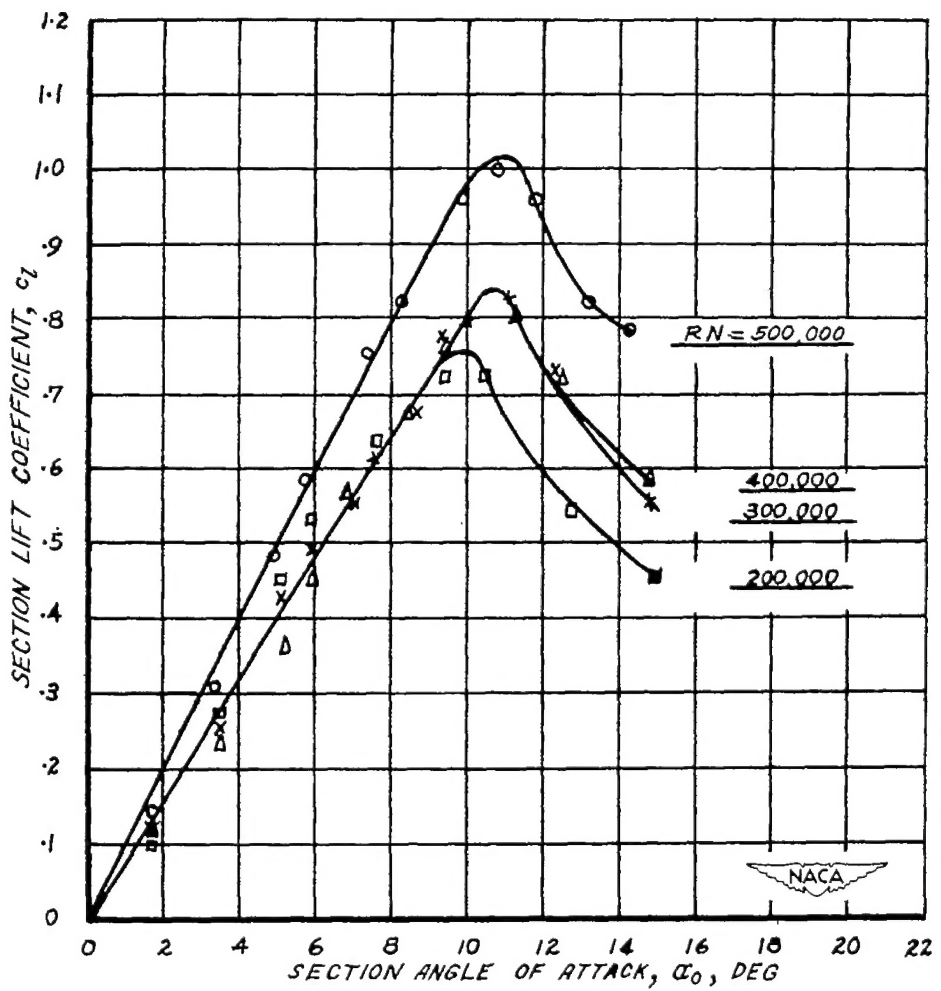


Figure 43.- Sectional lift characteristics of model rotor blade at various low Reynolds numbers RN.

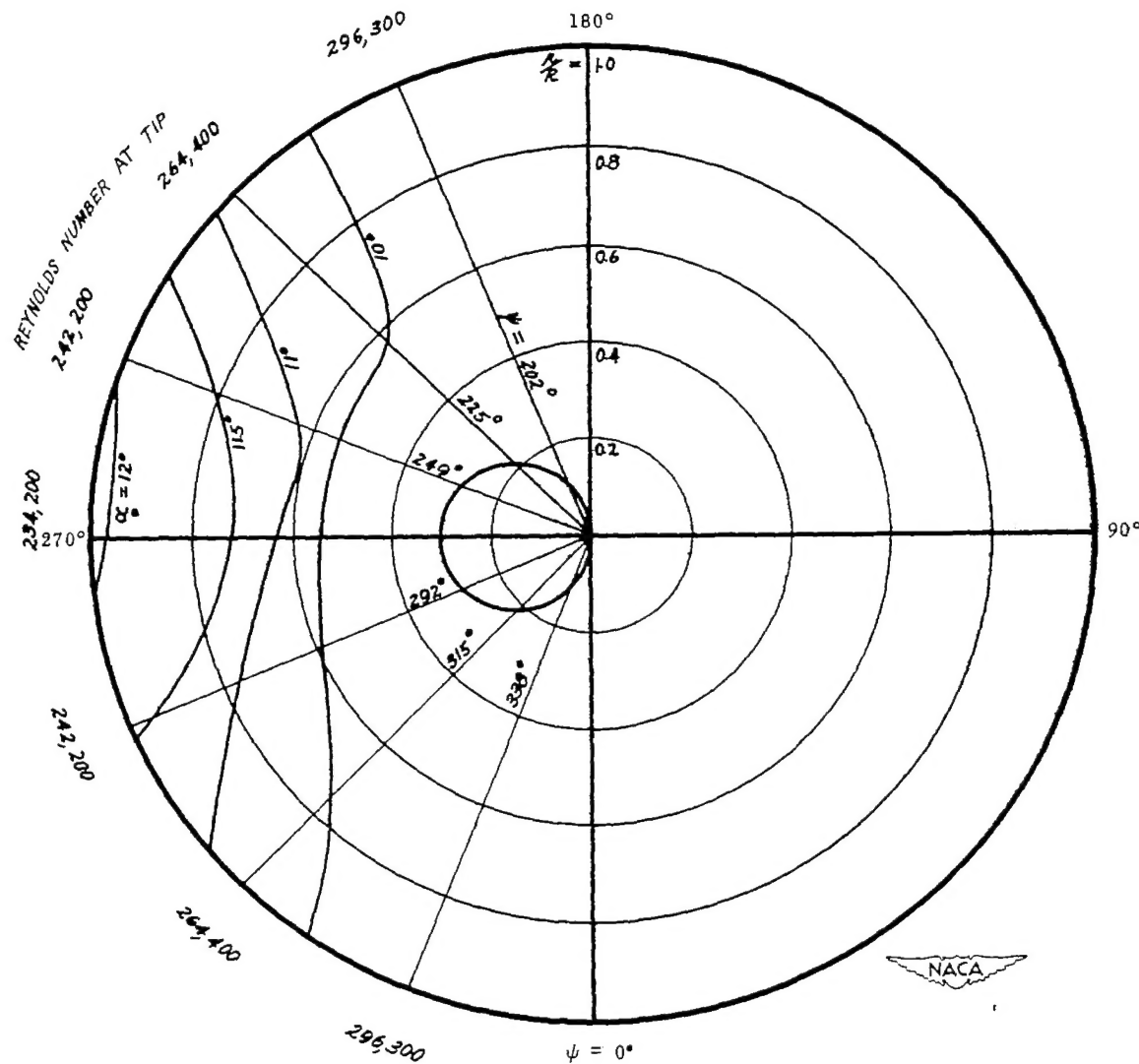


Figure 44.- Blade angle-of-attack distribution for critical region.  
 $\xi = 0$ ;  $\mu = 0.30$ ;  $\theta = 8^\circ$ ;  $\alpha = -5^\circ$ ;  $C_T/\sigma = 0.10$ .

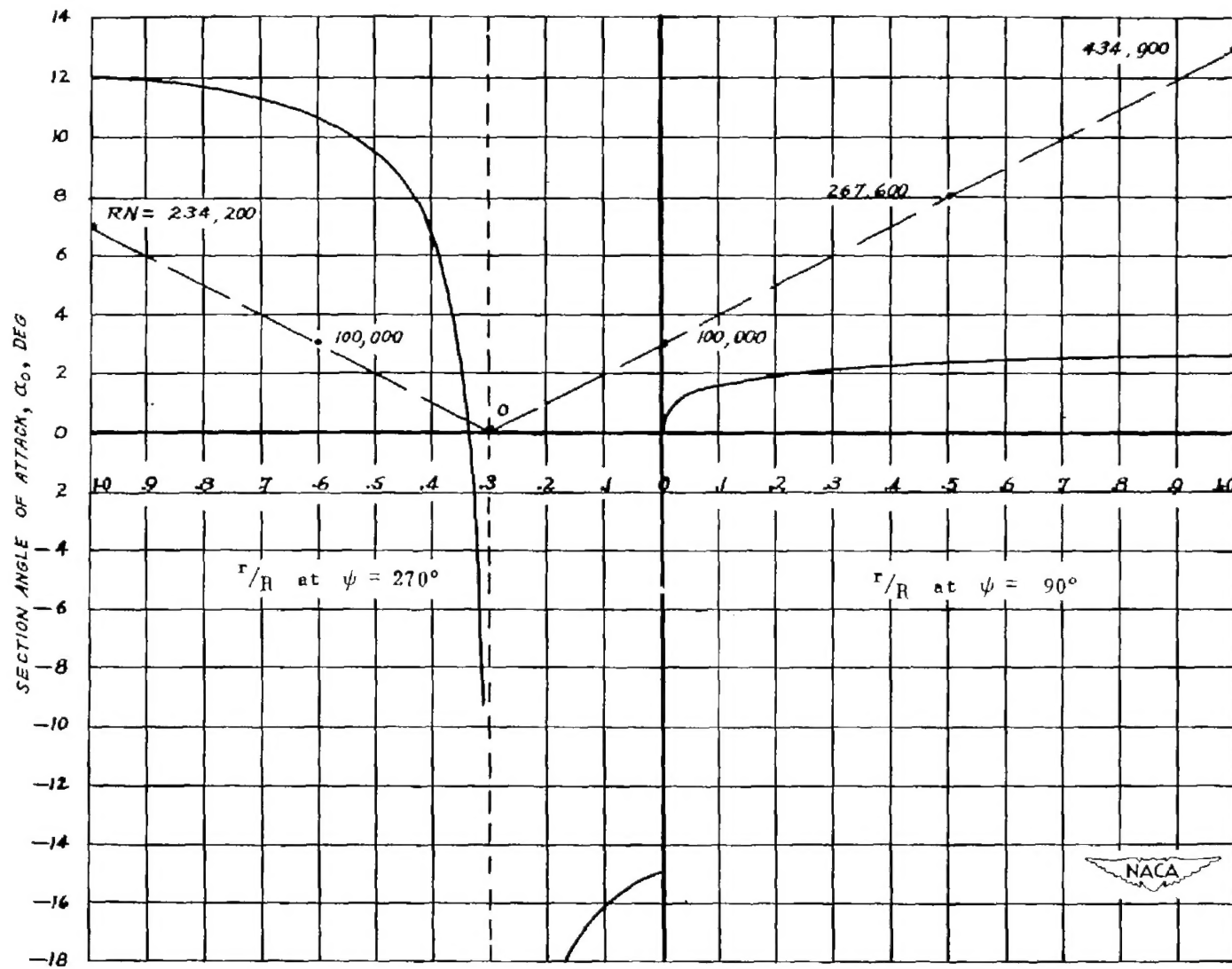


Figure 45.- Angle-of-attack distribution along blade span for azimuths of  $90^\circ$  and  $270^\circ$ .  $\xi = 0$ ;  $\mu = 0.30$ ;  $\theta = 8^\circ$ ;  $\alpha = -5^\circ$ ;  $C_T/\sigma = 0.10$ .